



UNIVERSITA' DI PISA

Dipartimento di Ingegneria Civile e Industriale

Tesi di Laurea Magistrale

A Computational Multi-purpose Unsteady Aerodynamic Solver for the Analysis of Innovative Wing Configurations, Helicopter Blades and Wind Turbines

RELATORI

CANDIDATO

Prof. Aldo Frediani

Massimiliano Nardini

Prof. Luciano Demasi

Dott. Ing. Rauno Cavallaro

Anno accademico 2013-2014

*Ai miei genitori
e a tutti coloro
che mi sono stati accanto
nel lungo percorso
che ha portato a questo traguardo*

Acknowledgements

Il primo ringraziamento va senza dubbio al Prof. Aldo Frediani, per avermi offerto l'opportunità di svolgere questo lavoro di tesi di cui sono orgoglioso. Un grazie va al Prof. Luciano Demasi, per avermi seguito durante il mio lavoro a San Diego e per la capacità con cui gestisce il suo team di ricerca, di cui ho avuto la fortuna di far parte in questi mesi. Un ringraziamento particolare va a Rauno Cavallaro, per il tempo che mi ha dedicato nello svolgimento del mio lavoro; grazie per la pazienza e la dedizione con cui ha seguito ogni passo della mia ricerca e grazie per l'aiuto e per i preziosi consigli.

Un sentito ringraziamento ai miei colleghi con cui ho condiviso questa esperienza a San Diego: grazie per l'aiuto reciproco e per la vostra insostituibile compagnia sia nei momenti di svago, sia in quelli di duro lavoro. Un ringraziamento speciale va ad Andrea, Luca e Rocco, perché non c'è luogo che meriti di essere visto o viaggio che meriti di essere intrapreso senza avere accanto la giusta compagnia. Un grazie anche a tutti i nuovi amici conosciuti in questi straordinari dieci mesi; grazie per i bellissimi ricordi e per avermi arricchito in un modo che non mi sarei mai aspettato.

Un immenso grazie ai miei amici di sempre, quelli con cui sono cresciuto e con cui condivido alcuni tra i ricordi più belli che ho; grazie per essermi stati accanto anche quando ero distante e soprattutto grazie per avermi accolto come se dieci mesi fossero trascorsi in un solo giorno.

Un grazie va ai miei parenti più stretti, in particolare le mie zie e la mia nonna che aspettano da anni questo traguardo. C'è una persona speciale con cui avrei tanto voluto condividere questo successo, e anche se non è qui con me so che sarebbe orgogliosa come sempre.

Infine il ringraziamento più importante va ai miei genitori, senza i quali non sarei la persona che sono adesso: grazie per avermi incoraggiato e sostenuto in ogni modo possibile.

So che questo non è un punto di arrivo, ma l'inizio di una nuova avventura, e spero che tutte le persone che ho incontrato sulla mia strada e che hanno condiviso qualcosa con me continuino ad essere in qualche modo al mio fianco, perché in questo modo so per certo che saprò affrontare al meglio qualsiasi cosa mi riservi il futuro. Grazie.

Abstract

In the last 50 years the use of numerical tools for the study of fluid dynamics problems in different engineering branches (aeronautical, energetic, automotive, civil engineering) has grown exponentially. From the first attempts to solve highly simplified flows around easy two-dimensional geometries, computational fluid dynamics has become an indispensable tool in every stage of a project design, from the conceptual design to the optimization, as well as the fine tuning or the post-manufacturing analysis.

With modern computational resources, it is possible to solve three-dimensional highly unsteady flows around complex configurations like aircrafts in maneuver, large wind turbine farms or even atmospheric boundary layer between city buildings.

Despite the huge leaps made in the computational fluid dynamics field, a lot of work still has to be done; with the exception of simplified geometries and low Reynolds numbers, far from engineering practical applications, direct solution of the Navier-Stokes equations is not yet possible. Computational models like RANS (Reynolds Average Navier-Stokes) and LES (Large Eddy Simulations) still have many unresolved issues and the accuracy of the results is strongly dependent on arbitrary parameters like the turbulence models adopted. Another fundamental issue to take into account is the computational cost of a numerical method: large RANS simulations, for example, often require several processors to run, as well as computational times varying from several hours to a few days.

In this scenario, a good compromise between fidelity of the simulation, application versatility and computational costs is represented by panel methods. Panel methods are numerical methods to solve potential flows around multiple kinds of geometries and can be applied in all those situations in which the flow can be considered as irrotational (high Reynolds numbers, attached flow, boundary layers effects negligible). Thus, they represent an ideal tool for a wide variety of aerodynamic problems, from the analysis of airfoils and three-dimensional wings, to the study of wind turbines, helicopter rotors and propellers, giving excellent results in all those cases where the hypothesis of irrotational flow are met, with computational times that are *at least* one order smaller than those required by higher fidelity simulations like RANS or LES. Thanks to their versatility and their efficiency, panel codes are widely

used in different stages of an aerodynamic project, from the conceptual design to advanced post-optimization phases.

The main aim of this work is the development and validation of a three-dimensional multi-purpose panel code, with particular attention to the study of highly unsteady problems like the aerodynamics of rotors and blades, as well as multi-body simulations involving the interactions between bodies and unsteady wakes and even flows around non-conventional aircraft configurations like Joined Wings.

The second part of the thesis is focused on the application of the panel code to the problem of the integration of the propellers in the aero-mechanic design of an amphibious *PrandtlPlane* aircraft. Different modeling options will be taken into account and the results will be compared and discussed, with the aim of giving an insight of the advantages that a panel code offers and of the information that can be obtained from a simulation, as well as the limits of this method.

Contents

I	THEORY AND CODE DEVELOPMENT	5
1	Introduction	6
2	Incompressible, Potential Flows	8
2.1	Potential flow	8
2.2	Continuity equation	9
2.3	Momentum conservation and Bernoulli equation	9
2.4	Definition of the mathematical problem	10
2.5	Integral formulation of the Laplace equation	11
2.6	D'Alembert paradox and potential wake	14
2.6.1	Boundary conditions	16
2.6.2	Integral formulation	17
2.7	Existence and uniqueness of solutions	18
2.8	Boundary element method	20
2.8.1	Elementary solution of Laplace equation	22
2.8.2	Boundary element method: mathematical formulation	23
2.8.3	Dirichlet boundary condition	24
3	Numerical Panel Method	26
3.1	Geometry discretization	26
3.1.1	Panel geometry	27
3.2	Singularities	32
3.2.1	Farfield	33
3.3	Linear system	34
3.4	Potential wake: vortex desingularization	38
3.4.1	Kelvin's theorem	40

3.4.2	Velocity induced by a vorticity distribution	41
3.4.3	Induction of a vorticity filament: Biot-Savart	41
3.4.4	Straight vortex segment	42
3.4.5	Doublet - vortex equivalence	43
3.4.6	Vortex singularity	44
3.4.7	Vortex regularization	44
3.5	Force evaluation: Bernoulli theorem	45
3.6	Surface differentiation of perturbation potential	47
3.6.1	Pressure coefficient	50
3.7	Iterative Kutta condition	50
4	Body-Wake Interaction: Alternative Formulation	55
4.1	Body-wake impingement	55
4.2	Alternative formulation	56
4.2.1	Pressures evaluation	59
5	Kinematics	61
5.1	Coordinate systems	61
5.1.1	Euler angles	62
5.1.2	Coordinate transformation	63
5.2	Bodies motion	64
5.3	Quaternions	65
5.3.1	Equivalence between quaternions and Euler angles	67
5.3.2	Determining the attitude of a frame of reference in motion	68
5.4	Practical implementation	69
5.5	Recapitulatory table	69
6	Code Improvements	72
6.1	Symmetry	72
6.1.1	Perturbation potential induction	72
6.1.2	Velocity induction	76
6.1.3	Forces and moments evaluation	77
6.2	Zero-thickness bodies: vortex lattice method	79
6.2.1	Vortex lattice method	79
6.3	Mixed problem	80

7	Validations	83
7.1	Wagner-based test case	83
7.2	Theodorsen-based test case	87
7.2.1	Theodorsen's theory: brief outline	88
7.2.2	Pure heaving	90
7.2.3	Pure pitching	92
7.3	Propeller - Biermann and Gray 1942 NACA report	93
7.4	Caradonna-Tung experiment	95
II	APPLICATIONS: <i>IDINTOS</i> PROJECT	102
8	Introduction	103
9	IDINTOS: Propeller	105
9.1	Geometry and mesh	105
9.2	Comparison between panel code and BET	107
10	IDINTOS: Aircraft Models and Propellers Integration	114
10.1	Introduction	114
10.2	Description of the analyzed joined-wing configurations	114
10.3	Modeling options for the wing system and propeller's influence	117
10.3.1	Rigid/Free Wake modeling effects	117
10.3.2	Iterative Kutta condition	120
10.3.3	Propeller's wake influence on the wing system aerodynamics	123
10.4	Fuselage	125
11	Conclusions	131
11.1	Discussion on the results	131
11.2	Future developments	133
	Appendices	134
A	Singularities	135
A.1	Constant strength quadrilateral doublet	135
A.1.1	Velocity potential induction	136
A.1.2	Self-induction	136

A.1.3	Farfield	136
A.2	Constant strength quadrilateral source	137
A.2.1	Velocity potential induction	137
A.2.2	Farfield	138
B	Sensitivity Matrix	139
C	Kinematics	141
C.1	Rotation matrix	141
C.2	Transformation between multiple coordinate systems	142
C.3	Angular velocity and Euler Angles derivatives	143
C.4	Fourth Order Runge-Kutta integration	144
C.5	Derivative of a vector expressed in a different frame of reference	145
C.6	Derivative of a quaternion in another frame of reference	146
C.7	From quaternions to rotation matrix	148
D	Percentage Error	151

Part I

THEORY AND CODE DEVELOPMENT

Chapter 1

Introduction

Aerodynamic panel methods were first investigated at the beginning of the second half of the 20th century. Their success was a consequence of their reduced computational cost, based on the inherent properties of the method that uses a distribution of singularities on the boundary surface rather than in the entire volume surrounding the body. A brief history on panel methods as well as a comprehensive outline of the different variants (from the two-dimensional zero-thickness steady vortex based methods to the more advanced unsteady three-dimensional formulations) can be found in [12, 17].

As one of the main purposes of this work is to develop a code that is both efficient and able to be applied to a vast range of aerodynamic applications, unsteady three-dimensional panel methods have proved to be an excellent choice. Their versatility lies in the possibility to simulate flows around complex three-dimensional bodies, as long as the hypothesis of irrotational flow (that means vorticity confined in a thin region around the body) are not violated; this is the case of many engineering problems where streamlined bodies are involved. Panel methods applicabilities span from small-angle of attack airfoils and wings to propellers' blades, from helicopter rotors to wind turbine.

In the next sections the theory behind the potential flows as well as an outline of the numerical implementation of a boundary element method will be introduced. The uniqueness and existence of the mathematical solution will be discussed for three-dimensional simply connected and multiple-connected domains and an iterative procedure will be implemented to enforce the condition of zero pressure jump on the trailing edge (Kutta condition). An alternative boundary element formulation based on vortex rings desingularization will be introduced for the study of all those cases in which a wake passes close or impinges on a body.

One of the main feature of the panel code is the advanced kinematic module, based on mutual transformations between coordinate systems: it allows multi-body simulations where each body moves independently from the others.

Finally the code will be validated, comparing the results with different test cases found in literature.

Chapter 2

Incompressible, Potential Flows

The behaviour of a generic flow can be described through a system of non-linear coupled time-dependent equations known as Navier-Stokes equations. Although these equations can be theoretically applied to a huge range of flows, analytical solutions are known only for a few simple cases, while numerical solutions often requires huge computational cost, making almost impossible to directly solve the equations for common engineering applications. Under certain hypothesis, a series of approximations can be made to simplify the equations: while this restricts the generality, it also reduces the computational time. In this chapter the hypothesis of potential incompressible flow will be introduced, the consequently simplifications of the Navier-Stokes equations shown and the limits of their applicability discussed.

2.1 Potential flow

Consider a flow in which the fluid velocity in every point of the domain can be written as the gradient of a scalar function:

$$\mathbf{V} = \nabla\Phi. \quad (2.1)$$

Φ is called *velocity potential* and the flow is called *potential flow*. Using the definition of *vorticity*

$$\boldsymbol{\omega} = \nabla \times \mathbf{V} \quad (2.2)$$

and considering the identity (where \mathbf{a} is a generic vector)

$$\nabla \times (\nabla\mathbf{a}) = 0 \quad (2.3)$$

it is immediately clear that, by definition, a potential flow is also *irrotational*.

2.2 Continuity equation

The continuity equation in differential form can be written as

$$\frac{\partial \rho}{\partial t} + \nabla \cdot \rho \mathbf{V} = 0 \quad (2.4)$$

Assuming that the flow is also homogeneous and incompressible, it is possible to write the continuity equation in differential form as

$$\nabla \cdot \mathbf{V} = 0. \quad (2.5)$$

Assuming also that a velocity potential exists and substituting its definition 2.1 in 2.5, the so called *Laplace equation* for the velocity potential is obtained

$$\nabla^2 \Phi = 0. \quad (2.6)$$

2.3 Momentum conservation and Bernoulli equation

Starting from the Momentum equation for incompressible flows

$$\frac{\partial \mathbf{V}}{\partial t} + \mathbf{V} \cdot \nabla \mathbf{V} = \mathbf{f} - \frac{1}{\rho} \nabla p + \nu \nabla^2 \mathbf{V} \quad (2.7)$$

where \mathbf{f} represents the body forces and ν is the kinematic viscosity, through simple identities it is possible to express Equation 2.7 in terms of vorticity [8]. Neglecting body forces, it is

$$\frac{\partial \mathbf{V}}{\partial t} + \boldsymbol{\omega} \wedge \mathbf{V} = -\nabla \left(\frac{p}{\rho} + \frac{V^2}{2} \right) - \nu \nabla \times \boldsymbol{\omega}, \quad (2.8)$$

where $V = ||\mathbf{V}||$. Assuming that the flow is also irrotational, it is clear that the kinematic viscosity ν has no effect on the momentum equation: the flow behaves as it was *inviscid*. Substituting \mathbf{V} with $\nabla \Phi$, Equation 2.7 becomes

$$\nabla \left(\frac{\partial \Phi}{\partial t} + \frac{p}{\rho} + \frac{V^2}{2} \right) = 0 \quad (2.9)$$

that implies that the quantities on the left hand side are, at most, function of time throughout the entire field

$$\frac{\partial \Phi}{\partial t} + \frac{p}{\rho} + \frac{V^2}{2} = F(t). \quad (2.10)$$

As shown in [1], if necessary it is possible to determine the unknown function $F(t)$ substituting

$$\Phi' = \Phi - \int F(t)dt. \quad (2.11)$$

However, this is usually unnecessary when conditions are known at every time in a reference point in the flow: if, for example, at great distance from the body the flow is and remains uniform, indicating with p_∞ and \mathbf{V}_∞ pressure and speed in the reference point, it is

$$\frac{\partial \Phi}{\partial t} + \frac{p}{\rho} + \frac{V^2}{2} = \frac{p_\infty}{\rho} + \frac{V_\infty^2}{2}. \quad (2.12)$$

Equation 2.12 is known as Bernoulli equation for unsteady flows and, once the velocity field is known from the solution of 2.6, it allows to evaluate the pressure field in every point of the domain.

2.4 Definition of the mathematical problem

Imagine to have one or more solid bodies submerged in a potential, incompressible flow. As shown in Figure 2.1, the fluid domain \mathcal{V} is a closed volume bounded by the body surface \mathcal{S}_B and the outer boundary \mathcal{S}_∞ . For the following formulation, a frame of reference attached to the body will be used. In such coordinate system, it is possible to decompose the velocity

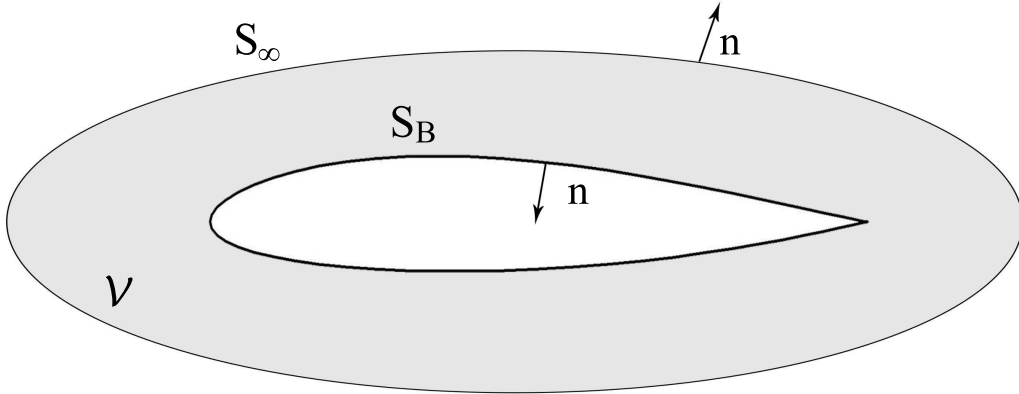


Figure 2.1: Potential domain.

potential into two contributions

$$\Phi = \Phi_\infty + \varphi; \quad (2.13)$$

from now on, Φ will be called *total velocity potential* (or just *total potential*), φ is called *perturbation velocity potential* (or *perturbation potential*) and Φ_∞ is the velocity potential of the undisturbed flow expressed in the considered frame of reference. Applying the gradient operator

$$\mathbf{V} = \mathbf{V}_\infty + \nabla\varphi \quad (2.14)$$

and substituting the velocity in Equation 2.6, it follows

$$\nabla^2\varphi = 0. \quad (2.15)$$

Indicating with \mathbf{n} the normal unit vector to the surface directed outside the domain \mathcal{V} , and considering the body as a solid surface, the normal component of the velocity must be zero (no-penetration condition):

$$\mathbf{V} \cdot \mathbf{n} = \frac{\partial\Phi}{\partial n} = 0. \quad (2.16)$$

Combining equation 2.14 with 2.16, it is

$$\frac{\partial\varphi}{\partial n} = -\mathbf{V}_\infty \cdot \mathbf{n} \quad (2.17)$$

and enforcing that the velocity perturbation potential must be zero when the distance from the body approaches infinite, the following system is obtained:

$$\left\{ \begin{array}{ll} \nabla^2\varphi = 0 & \text{for } \mathbf{x} \in \mathcal{V} \\ \frac{\partial\varphi}{\partial n} = -\mathbf{V}_\infty \cdot \mathbf{n} & \text{for } \mathbf{x} \in \mathcal{S}_B \\ \varphi \rightarrow 0 & \text{for } \|\mathbf{r}\| \rightarrow \infty \end{array} \right. \quad (2.18)$$

where \mathbf{y} are the coordinates of a point on the body, \mathbf{x} are the coordinates of a generic point in \mathcal{V} and $\mathbf{r} = \mathbf{x} - \mathbf{y}$. This system is linear and non explicitly time independent (the time dependence is in the boundary conditions) and it is possible to show that it has only one solution if the domain is *simply connected*. The definition of *simply connected* domain and the uniqueness of the solution will be discussed in the following sections.

2.5 Integral formulation of the Laplace equation

In this section, an integral formulation for the Laplace equation will be presented. The purpose of this formulation is to evaluate the velocity potential all over the domain, solving an

integral equation only on the boundaries. A method of solution based on the Green's function will be introduced. In Figure 2.2 the mathematical problem expressed in the previous section is displayed. The volume \mathcal{V} (domain) is the closed region bounded by the body surface \mathcal{S}_B and an external boundary \mathcal{S}_∞ . Solution $G(\mathbf{x}, \mathbf{y})$ of equation

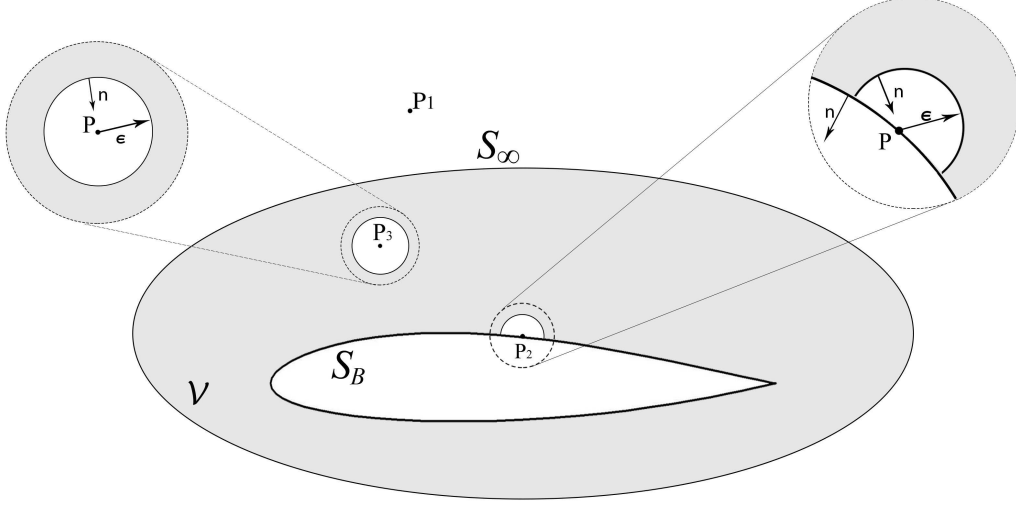


Figure 2.2: Potential domain. Three cases are taken into account, depending if point P lies in the domain, outside the domain or on the boundary.

$$\nabla^2 G(\mathbf{x}, \mathbf{y}) = \delta(\mathbf{y} - \mathbf{x}) \quad (2.19)$$

is introduced, where δ is the Dirac delta function. Equation 2.19 represents the induction of a unit source concentrated at the point \mathbf{y} and $G(\mathbf{x}, \mathbf{y})$, known as Green's function, is a fundamental solution of the Laplace equation. The expression for the Green's function depends on the domain and on the boundary conditions: in Table 2.1 the solutions for 2D and 3D unbounded domains are shown.

To show how to obtain an integral expression for φ , the starting point is the following equation, where $\mathcal{S} = \mathcal{S}_B + \mathcal{S}_\infty$. On the right hand side the second Green's identity is used.

$$\begin{aligned} \int_{\mathcal{S}} [G(\mathbf{x}, \mathbf{y}) \nabla \varphi(\mathbf{x}) - \varphi(\mathbf{x}) \nabla G(\mathbf{x}, \mathbf{y})] \cdot \mathbf{n} d\mathcal{S}(\mathbf{y}) = \\ \int_{\mathcal{V}} [G(\mathbf{x}, \mathbf{y}) \nabla^2 \varphi(\mathbf{x}) - \varphi(\mathbf{x}) \nabla^2 G(\mathbf{x}, \mathbf{y})] d\mathcal{V}(\mathbf{y}) \end{aligned} \quad (2.20)$$

From this point on, variables \mathbf{x} and \mathbf{y} will be made explicit only when necessary. It is important to remember that both functions G and φ satisfy Laplace equation inside the

2D domain	$G(\mathbf{x}, \mathbf{y}) = \frac{1}{2\pi} \ln \left(\frac{1}{\ \mathbf{y}-\mathbf{x}\ } \right)$
3D domain	$G(\mathbf{x}, \mathbf{y}) = -\frac{1}{4\pi} \frac{1}{\ \mathbf{y}-\mathbf{x}\ }$

Table 2.1: Laplace Fundamental Solutions.

domain \mathcal{V} and the right hand side of Equation 2.20 is zero. In Equation 2.20, \mathbf{n} indicates the normal unit vector to the boundary \mathcal{S} , oriented *outside* the volume \mathcal{V} .

Considering the velocity potential in a point $P(\mathbf{x})$, as the function G results weakly singular when $\mathbf{y} \rightarrow \mathbf{x}$, three different cases can occur, depending if P lies inside the volume \mathcal{V} , outside or on the boundary.

If P lies outside the volume \mathcal{V} , it simply is

$$\int_{\mathcal{S}} (G \nabla \varphi - \varphi \nabla G) \cdot \mathbf{n} d\mathcal{S}(\mathbf{y}) = 0 \quad (2.21)$$

If P lies inside the domain, it is possible to evaluate the integral in Equation 2.20 considering a small sphere of radius ϵ surrounding P and evaluating the limit as ϵ approaches zero [17]. The expression that results from the limit is

$$\varphi(\mathbf{x}) = \int_{\mathcal{S}} (G \nabla \varphi - \varphi \nabla G) \cdot \mathbf{n} d\mathcal{S}(\mathbf{y}) \quad (2.22)$$

Finally, if P lies on the boundary \mathcal{S} , it is possible to exclude it with a hemisphere and send the radius to zero

$$\varphi(\mathbf{x}) = 2 \int_{\mathcal{S}} (G \nabla \varphi - \varphi \nabla G) \cdot \mathbf{n} d\mathcal{S}(\mathbf{y}) \quad (2.23)$$

Results are summarized and generalized in Table 2.2. The identities

$$\nabla G \cdot \mathbf{n} = \frac{\partial G}{\partial n} \quad (2.24)$$

$$\nabla \varphi \cdot \mathbf{n} = \frac{\partial \varphi}{\partial n} \quad (2.25)$$

have been used.

$E(\mathbf{x})\varphi(\mathbf{x}) = \int_{\mathcal{S}_B} \left(G \frac{\partial \varphi}{\partial n} - \varphi \frac{\partial G}{\partial n} \right) d\mathcal{S}(\mathbf{y}) + \int_{\mathcal{S}_\infty} \left(G \frac{\partial \varphi}{\partial n} - \varphi \frac{\partial G}{\partial n} \right) d\mathcal{S}(\mathbf{y})$
$E(\mathbf{x}) = \begin{cases} 1 & \text{if } \mathbf{x} \in \mathcal{V} \\ \frac{1}{2} & \text{if } \mathbf{x} \in \mathcal{S} \\ 0 & \text{if } \mathbf{x} \in \mathbb{R}^3 \setminus \mathcal{V} \end{cases}$

Table 2.2: Integral formulation for velocity potential.

Finally, as φ and $\nabla\varphi$ both decrease to zero when the distance from the body becomes infinite, is it possible to prove [27] that, moving the outer boundary \mathcal{S}_∞ to infinite, the integral on that surface becomes zero. The final equation that allows to evaluate the velocity potential only involves the calculation of an integral on the body surface \mathcal{S}_B , in terms of the values of φ and $\frac{\partial \varphi}{\partial n}$ on \mathcal{S}_B :

$$E(\mathbf{x})\varphi(\mathbf{x}) = \int_{\mathcal{S}_B} \left(G \frac{\partial \varphi}{\partial n} - \varphi \frac{\partial G}{\partial n} \right) d\mathcal{S}(\mathbf{y}). \quad (2.26)$$

2.6 D'Alembert paradox and potential wake

The equations to find the velocity potential and the pressure in every point of the domain \mathcal{V} have been introduced and they are summarized in Table 2.3.

Considering a body immersed in a incompressible, irrotational and steady flow, the solution of the latter system generates a pressure field that, if integrated all over the body surface, gives a zero aerodynamic force. This result, known as D'Alembert paradox, collides with experiments and practical experience and, apparently, makes the potential flow model useless for practical simulations. The potential flow model considers the flow as irrotational *inside* the domain \mathcal{V} and, as already seen, this is a condition necessary and sufficient for the existence of a velocity potential: this is a good approximation for high Reynolds flows, where the vorticity is concentrated in a thin region around the body, known as *boundary layer*. However, the influence of the vorticity present in the boundary layer is crucial for the generation of the aerodynamic forces and somehow has to be included in the model.

Considering the body surface as a boundary of the domain \mathcal{V} , all the fluid particles that

$\left\{ \begin{array}{ll} \varphi(\mathbf{x}) = \int_{\mathcal{S}_B} \left(G \frac{\partial \varphi}{\partial n} - \varphi \frac{\partial G}{\partial n} \right) d\mathcal{S}(\mathbf{y}) & \text{for } \mathbf{x} \in \mathcal{V} \\[10pt] \frac{\partial \varphi}{\partial n} = -\mathbf{V}_\infty \cdot \mathbf{n} & \text{for } \mathbf{x} \in \mathcal{S}_B \\[10pt] \varphi \rightarrow 0 & \text{for } \mathbf{r} \rightarrow \infty \end{array} \right.$
$\frac{\partial \varphi}{\partial t} + \frac{p}{\rho} + \frac{V^2}{2} = \frac{p_\infty}{\rho} + \frac{V_\infty^2}{2}$

Table 2.3: Summary: potential field mathematical problem.

are in contact with the body at the generic time instant t are not *inside* the domain and it is not possible to define a potential for this particles. The particles that have been in contact with the body are then convected in the volume \mathcal{V} : this suggest the necessity to define the locus of this particles and to exclude this region from the volume \mathcal{V} . A *potential wake* \mathcal{S}_w is defined as the surface delimiting the region of the particles that have been in contact with the body; \mathcal{S}_w is part of the boundary of the domain \mathcal{V} and represents a region where vorticity generated by the interaction of the fluid with the body is present. This way, the main effects of vorticity, such as the generation of the aerodynamic forces, can be taken into account, but at the same time the flow inside the volume \mathcal{V} remains irrotational and does not collide with the hypothesis of potential flow. The potential wake can be seen as a *discontinuity surface* (it is considered to have zero thickness) for the potential, where the vorticity generated on the body surface is shed downstream.

According to this considerations, the shape and position of the wake are not known a priori, but are part of the solution. An important information that needs to be specified is where the wake is shed from the body: for aerodynamic bodies, this happens from the sharp trailing edge. Further details will be given in the next sections.

It is necessary to define new boundary conditions for the potential wake.

2.6.1 Boundary conditions

Since a new surface \mathcal{S}_w has been introduced in the problem, boundary conditions have to be specified on this surface. Differently to what introduced for a solid surface, the boundary conditions are not just purely kinematics; the wake is not a solid surface, but a free surface, a surface that can be deformable and moving and that separates two different states of motion of the same fluid [19], so a dynamic equilibrium boundary condition can be derived too.

For each point of the wake surface, it is

$$\mathbf{V}_{up} \cdot \mathbf{n} = \mathbf{V}_{down} \cdot \mathbf{n} = \mathbf{V}_w \cdot \mathbf{n} \quad (2.27)$$

where \mathbf{V}_{up} and \mathbf{V}_{down} are the velocities of the fluid on both sides of the wake, while \mathbf{V}_w is the velocity of the wake.

The dynamic equilibrium condition for a free surface moving in a inviscid flow is that for every infinitesimal surface element $d\mathcal{S}$ is

$$(p_{up} - p_{down}) \cdot \mathbf{n} d\mathcal{S} = 0 \quad (2.28)$$

that means

$$p_{up} = p_{down} \quad (2.29)$$

everywhere on the surface.

Decomposing the velocities in free-stream velocity and perturbation velocity and recalling the definition of velocity potential, it is

$$\mathbf{V}_{up} = \mathbf{V}_\infty + \mathbf{v}_{up} = \nabla (\Phi_\infty + \varphi_{up}) \quad (2.30)$$

$$\mathbf{V}_{down} = \mathbf{V}_\infty + \mathbf{v}_{down} = \nabla (\Phi_\infty + \varphi_{down}) \quad (2.31)$$

$$\mathbf{V}_w = \mathbf{V}_\infty + \mathbf{v}_w = \nabla (\Phi_\infty + \varphi_w) \quad (2.32)$$

where \mathbf{v}_{up} and \mathbf{v}_{down} are the perturbation velocities on the two sides of the wake, while \mathbf{v}_w is the perturbation velocity with which the wake is moving.

From 2.27 it is not hard to prove that

$$\mathbf{v}_w = \frac{1}{2}(\mathbf{v}_{up} + \mathbf{v}_{down}); \quad (2.33)$$

introducing the velocity potential and recalling that

$$\nabla() \cdot \mathbf{n} = \frac{\partial()}{\partial n} \quad (2.34)$$

it is possible to write

$$\frac{\partial \varphi}{\partial n} \Big|_{up} - \frac{\partial \varphi}{\partial n} \Big|_{down} = \Delta \left(\frac{\partial \varphi}{\partial n} \right) = 0 \quad \text{for } \mathbf{x} \in \mathcal{S}_w \quad (2.35)$$

that means that the normal component of the perturbation velocity is continue across the wake; the wake is not a discontinuity surface for the normal velocity, while the tangential velocity is allowed to be discontinuous.

From Bernoulli theorem, neglecting body forces and applying 2.29 it is

$$\frac{\partial \varphi}{\partial t} \Big|_{up} + \frac{||\mathbf{V}_\infty + \mathbf{v}_{up}||^2}{2} = \frac{\partial \varphi}{\partial t} \Big|_{down} + \frac{||\mathbf{V}_\infty + \mathbf{v}_{down}||^2}{2} \quad (2.36)$$

and, as shown in [5], Equation 2.36 leads to

$$\frac{D}{Dt} \Delta \varphi := \left(\frac{\partial}{\partial t} + \mathbf{V}_w \cdot \nabla \right) \Delta \varphi = 0 \quad \text{for } \mathbf{x} \in \mathcal{S}_w. \quad (2.37)$$

Equation 2.37 states that for a wake point $\mathbf{x}_w(t)$ moving with speed \mathbf{v}_w the quantity $\Delta \varphi$ remains constant.

2.6.2 Integral formulation

To include the potential wake in the integral formulation of the velocity potential, a process similar to the one presented in Section 2.5 is adopted. As shown in Figure 2.3, $\mathcal{S} = \mathcal{S}_\infty + \mathcal{S}_B + \mathcal{S}_w$ is the new boundary of the domain \mathcal{V} and \mathcal{S}_w indicates the potential wake, the zero-thickness region that includes the vorticity shed from the body surface.

The integral formulation becomes

$$E(\mathbf{x})\varphi(\mathbf{x}) = \int_{\mathcal{S}_B} \left(G \frac{\partial \varphi}{\partial n} - \varphi \frac{\partial G}{\partial n} \right) d\mathcal{S}(\mathbf{y}) + \int_{\mathcal{S}_w} \left(G \frac{\partial \varphi}{\partial n} - \varphi \frac{\partial G}{\partial n} \right) d\mathcal{S}(\mathbf{y}). \quad (2.38)$$

As previously stated, the wake is a zero-thickness surface and represents a discontinuity for the potential φ ; it is possible to split the integral over \mathcal{S}_w in the contributions of the two sides, *up* and *down*. The Green function G is continuous across the wake, as well as $\frac{\partial \varphi}{\partial n}$, while the normal vectors \mathbf{n} are opposite on the two sides of \mathcal{S}_w , so it is possible to state that

$$\int_{\mathcal{S}_w} \left(G \frac{\partial \varphi}{\partial n} \right) d\mathcal{S}(\mathbf{y}) = 0. \quad (2.39)$$

Following the results of 2.39, the integral over \mathcal{S}_w can be written as

$$- \int_{\mathcal{S}_w^{up}} \left(\varphi^{up} \frac{\partial G}{\partial n} \right) d\mathcal{S}(\mathbf{y}) - \int_{\mathcal{S}_w^{down}} \left(\varphi^{down} \frac{\partial G}{\partial n} \right) d\mathcal{S}(\mathbf{y}) \quad (2.40)$$

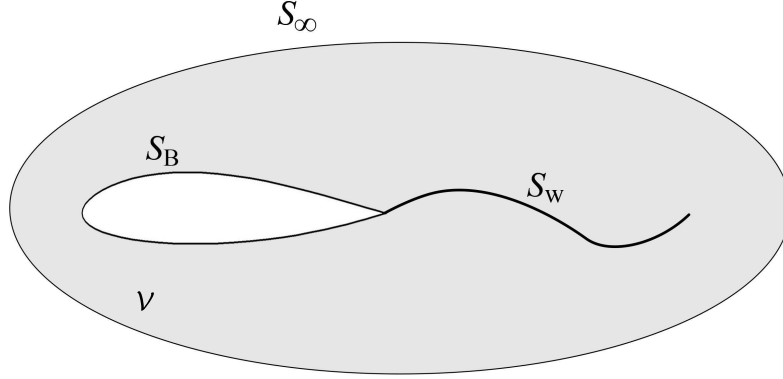


Figure 2.3: Potential wake domain.

and using the continuity of G across S_w and remembering that the normal vectors are opposite on the two sides, it is

$$-\int_{S_w^{up}} \left(\varphi^{up} \frac{\partial G}{\partial n} \right) dS(\mathbf{y}) + \int_{S_w^{down}} \left(\varphi^{down} \frac{\partial G}{\partial n} \right) dS(\mathbf{y}) = \int_{S_w^{up}} \left(\Delta \varphi \frac{\partial G}{\partial n} \right) dS(\mathbf{y}) \quad (2.41)$$

where

$$\Delta \varphi = \varphi^{up} - \varphi^{down}. \quad (2.42)$$

Collecting all the results together, the integral formulation of the Laplace equation including the potential wake is summarized in Table 2.4

2.7 Existence and uniqueness of solutions

From the analytical point of view, some issues regarding the existence and uniqueness of the solutions have to be discussed. The analytical theory is in many cases non-trivial and, as this is not the main topic of this work, only a general outline will be given. Detailed and extensive information can be found in [3–5]. Considering the case of a two dimensional airfoil immersed in a steady flow, it is possible to notice that the domain is multiply connected, because a closed curve surrounding the airfoil is not reducible. In this case the potential is a multi-valued function and the solution is not unique, unless a branch-cut is introduced in the domain. This way the domain becomes simply connected and, with a proper condition on the

$E(\mathbf{x})\varphi(\mathbf{x}) = \int_{\mathcal{S}_B} \left(\frac{\partial \varphi}{\partial n} G - \varphi \frac{\partial G}{\partial n} \right) d\mathcal{S}(\mathbf{y}) - \int_{\mathcal{S}_w} \left(\Delta \varphi \frac{\partial G}{\partial n} \right) d\mathcal{S}(\mathbf{y})$
$E(\mathbf{x}) = \begin{cases} 1 & \text{if } \mathbf{x} \in \mathcal{V} \\ \frac{1}{2} & \text{if } \mathbf{x} \in \mathcal{S}_B \cup \mathcal{S}_w \\ 0 & \text{if } \mathbf{x} \in \mathbb{R}^3 \setminus \mathcal{V} \end{cases}$

Table 2.4: Integral formulation for the velocity potential including the contribution of the potential wake.

cut known as Kutta-Joukowski condition, the solution becomes unique. The two-dimensional steady Kutta-Joukowski condition consists in enforcing that on sharp trailing edge the velocity is bounded and no singularities occur. For the unsteady two-dimensional case the non-uniqueness of the solution is due to the presence of the wake, that is a discontinuity surface for the potential: in this case the Kutta-Joukowski condition consists in enforcing no pressure jump on the two sides of the wake and is equivalent to enforce that the velocity on the trailing edge is bounded. Setting the wake potential on the trailing edge to enforce zero pressure jump allows to remove a singularity on the trailing edge and as a result the velocity remains bounded. For three-dimensional domains the theory behind the singularity removal is basically an extension of the two-dimensional theory; an important difference is that the Kutta condition (zero pressure jump on trailing edge) and the Joukowski condition (bounded velocity on trailing edge) do not always imply each other as happens in the two dimensional case. If the domain is simply connected, consequence of the presence of the wake the potential is still a multi-valued function and the Joukowski condition (singularity removal) has to be enforced to determine the wake intensity. Indicating with \mathbf{x}_W^{TE} a wake point on trailing edge, the intensity of the wake on trailing edge is set to be equal to the difference between the body perturbation potential on the two sides of the wake, here indicated with *up* and *down*:

$$\Delta \varphi(\mathbf{x}_W^{TE}) = \varphi_{TE}^{up} - \varphi_{TE}^{down}. \quad (2.43)$$

There are still open questions whether or not this condition is sufficient to satisfy also the Kutta condition [5]. If the domain is multiply connected, as in the case of a joined-wing system or of a propeller's shroud, the potential is still multi-valued and different conditions

have to be enforced to remove all kinds of three-dimensional singularities. More detailed information are given by [5, 18, 23]. As many of the issues regarding singularity removal on the trailing edge are still unsolved, in this work, following the results obtained in [5, 23], the direction of the wake on the trailing edge will be taken as the bisector of the solid angle formed by the two body panels concurring at the trailing edge, as shown in Figure 2.4. This condition on the wake geometry, combined to the condition on the wake potential in

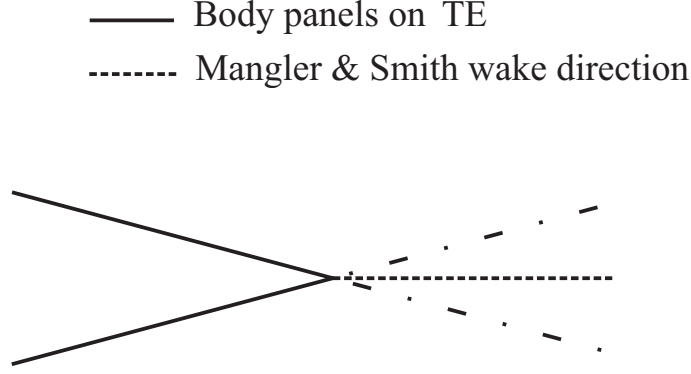


Figure 2.4: Wake direction on trailing edge as the bisector of the angle formed by the directions of the trailing edge body panels.

Equation 2.43, has proven to be sufficient to remove all the singularities. For a zero-order panel method these conditions are not enough to ensure a zero pressure jump on the trailing edge: for this reason, a numerical iterative procedure will be introduced to correct the wake intensity accordingly.

2.8 Boundary element method

Consider again the problem of a body immersed in a potential flow. The integral formulation for the case of Figure 2.1 has already been determined in Section 2.6.2. To include the effects of the internal potential, it is possible to consider the case of Figure 2.5, with \mathcal{V}_{in} as domain, and find an integral formulation for the internal potential with the same procedure used in Section 2.5.

Combining the two formulations, the presented in Table 2.6 is obtained. The minus sign is because of the opposite normals. Equation listed in Table 2.6 is valid inside and outside the volume bounded by \mathcal{S}_B .

$E(\mathbf{x})\varphi(\mathbf{x}) = \int_{\mathcal{S}_B} \left(\frac{\partial \varphi^{in}}{\partial n} G - \varphi^{in} \frac{\partial G}{\partial n} \right) d\mathcal{S}(\mathbf{y}) - \int_{\mathcal{S}_w} (\Delta \varphi \frac{\partial G}{\partial n}) d\mathcal{S}(\mathbf{y})$
$E(\mathbf{x}) = \begin{cases} 1 & \text{if } \mathbf{x} \in \mathcal{V}_{in} \\ \frac{1}{2} & \text{if } \mathbf{x} \in \mathcal{S}_B \cup \mathcal{S}_w \\ 0 & \text{if } \mathbf{x} \in \mathbb{R}^3 \setminus \mathcal{V}_{in} \end{cases}$

Table 2.5: Integral formulation for the internal potential including the contribution of the potential wake.

$\varphi(\mathbf{x}) = \int_{\mathcal{S}_B} \left(\left(\frac{\partial \varphi^{out}}{\partial n} - \frac{\partial \varphi^{in}}{\partial n} \right) G - (\varphi^{out} - \varphi^{in}) \frac{\partial G}{\partial n} \right) d\mathcal{S}(\mathbf{y}) -$ $\int_{\mathcal{S}_w} (\Delta \varphi \frac{\partial G}{\partial n}) d\mathcal{S}(\mathbf{y})$
$E(\mathbf{x}) = \begin{cases} 1 & \text{if } \mathbf{x} \in \mathcal{V} \\ \frac{1}{2} & \text{if } \mathbf{x} \in \mathcal{S}_B \cup \mathcal{S}_w \\ 1 & \text{if } \mathbf{x} \in \mathcal{V}_{in} \end{cases}$

Table 2.6: Integral formulation for the potential inside and outside the volume bounded by \mathcal{S}_B .

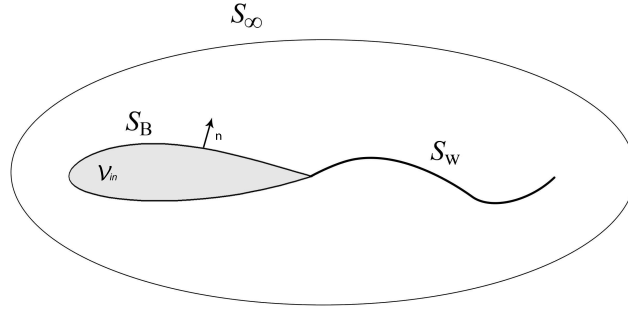


Figure 2.5: Potential wake formulation: internal domain.

2.8.1 Elementary solution of Laplace equation

As seen in the previous section, the integral formulation requires only the values of φ and $\nabla\varphi$ on the boundaries to evaluate the velocity potential in every point of the domain (to be precise, even outside the domain and on the boundaries). As the Laplace equation is linear, it is possible to obtain the velocity potential φ as a linear combination (superimposition) of a certain number of elementary solutions. In this section, most common three dimensional elementary solutions will be introduced. See [11] for a comprehensive introduction to two-dimensional and three-dimensional elementary solutions of the Laplace equation.

Source

In a three-dimensional, incompressible, steady flow Equation 2.44 represents the potential field induced by a *point source* placed in \mathbf{y} :

$$\varphi_s(\mathbf{x}) = \sigma G(\mathbf{x}, \mathbf{y}) = \frac{\sigma}{4\pi} \frac{1}{\|\mathbf{x} - \mathbf{y}\|}. \quad (2.44)$$

The symbol σ denotes the source intensity. It is easy to prove that φ_s is a solution of the Laplace equation. Imagining a distribution of sources over a surface \mathcal{S} , the induced perturbation potential results

$$\varphi(\mathbf{x}) = \int_{\mathcal{S}} \sigma(\mathbf{y}) G(\mathbf{x}, \mathbf{y}) d\mathcal{S}(\mathbf{y}). \quad (2.45)$$

This relation will be useful in the next sections. It is important to notice that Equation 2.44 presents a singularity when $\mathbf{x} \rightarrow \mathbf{y}$.

Doublet

As the Laplace equation is linear, superimposing the inductions of two sources of opposite signs originates a velocity potential field that is still solution of the Laplace equation. Imagining to reduce the distance d between the sources to zero and at the same time to increase the strengths σ of the sources to infinite, in such a way that the product σd remains finite, the expression of the induction of the doublet is obtained [11].

Assuming $\mu = \sigma d$, where μ is the strength of the doublet, and indicating with \mathbf{n} the direction of the segment (that collapses into a point as d is sent to zero) between the two sources, the expression of the induction of the doublet is

$$\varphi_d = -\mu G(\mathbf{x}, \mathbf{y}) \frac{\mathbf{n} \cdot (\mathbf{x} - \mathbf{y})}{\|\mathbf{x} - \mathbf{y}\|^3} = -\frac{\mu}{4\pi} \frac{\mathbf{n} \cdot (\mathbf{x} - \mathbf{y})}{\|\mathbf{x} - \mathbf{y}\|^3} \quad (2.46)$$

It is easy to show that

$$\varphi_d = -\frac{\partial \varphi_s}{\partial n} = -\frac{\partial G}{\partial n} \quad (2.47)$$

and, as done with the source, imagining a distribution of doublets on a surface \mathcal{S} , the expression of the velocity potential in a generic point \mathbf{x} is

$$\varphi(\mathbf{x}) = \int_{\mathcal{S}} \left(\mu(\mathbf{y}) \frac{\partial G(\mathbf{x}, \mathbf{y})}{\partial n} \right) d\mathcal{S}(\mathbf{y}). \quad (2.48)$$

2.8.2 Boundary element method: mathematical formulation

Using the results obtained in the previous sections, it is possible to rewrite the integral formulation for a body immersed in a potential flow, considering a linear combination of elementary solutions of Laplace equation distributed on the boundaries of the domain \mathcal{V} . Consider a source distribution of unknown intensity σ and a doublet distribution of intensity μ on the body surface \mathcal{S}_B , and a doublet distribution of intensity μ_W on the wake surface \mathcal{S}_w . Recalling 2.45 and 2.48 and remembering the linearity of Laplace equation, the velocity potential in a generic point \mathbf{x} of \mathcal{V} can be written in the following form:

$$\varphi(\mathbf{x}) = \int_{\mathcal{S}_B} \left(\sigma G - \mu \frac{\partial G}{\partial n} \right) d\mathcal{S}(\mathbf{y}) - \int_{\mathcal{S}_w} \left(\mu_W \frac{\partial G}{\partial n} \right) d\mathcal{S}(\mathbf{y}). \quad (2.49)$$

Figure 2.6 shows the orientation of the unit vector \mathbf{n} for each surface. From the comparison

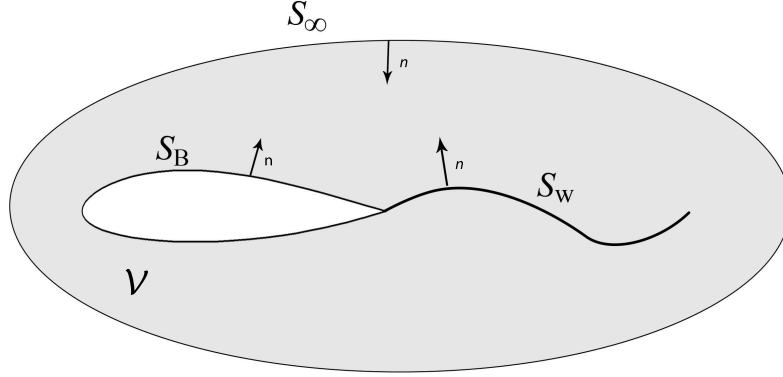


Figure 2.6: Orientations of normal vectors.

of 2.26 and 2.49, the following relations can be derived:

$$\sigma = \frac{\partial \varphi}{\partial n} \Big|_{S_B}^{out} - \frac{\partial \varphi}{\partial n} \Big|_{S_B}^{in} \quad (2.50)$$

$$\mu = \varphi|_{S_B}^{out} - \varphi|_{S_B}^{in} \quad (2.51)$$

$$\mu_W = \Delta \varphi|_{S_w}. \quad (2.52)$$

This is a fundamental result and it is the basis of the boundary element method. As already seen, to evaluate the velocity potential in the domain, only the values of the potential on the boundaries are needed. Using the linearity of the Laplace equation and introducing surface distributions of sources and doublets as elementary solutions, finding the velocity potential on the boundaries means finding the unknown singularity intensities σ , μ and μ_W .

2.8.3 Dirichlet boundary condition

The no-penetration condition 2.16 leads to Equation 2.17 that can be seen as a Neumann boundary condition on the normal derivative of φ for the closed boundary S_B . This condition

can be converted in a Dirichlet boundary condition on φ , enforcing that internal perturbation velocity potential is zero [17]:

$$\varphi^{in} = 0. \quad (2.53)$$

As a consequence, combining 2.53 and 2.53, it is $\frac{\partial \varphi^{in}}{\partial n} = 0$, from which the intensities of the sources are obtained:

$$\sigma = \frac{\partial \varphi^{out}}{\partial n} - \frac{\partial \varphi^{in}}{\partial n} = \frac{\partial \varphi^{out}}{\partial n} = -\mathbf{V}_\infty \cdot \mathbf{n}. \quad (2.54)$$

The integral formulation with homogeneous Dirichlet boundary condition becomes:

$$\begin{cases} \oint_{\mathcal{S}_B} (\sigma G - \mu \frac{\partial G}{\partial n}) d\mathcal{S}(\mathbf{y}) - \int_{\mathcal{S}_w} (\Delta \varphi \frac{\partial G}{\partial n}) d\mathcal{S}(\mathbf{y}) = 0 \\ \sigma = -\mathbf{V}_\infty \cdot \mathbf{n} \end{cases} \quad (2.55)$$

Chapter 3

Numerical Panel Method

In the previous chapters, the analytical formulation of a Boundary Element Method (BEM) to solve potential flows around aerodynamic bodies has been introduced. While analytical solutions are available just for simple geometries, numerical methods allow to treat more complex cases and can be applied to many engineering problems. In this chapter the theory behind the development of an unsteady numerical panel method will be presented.

3.1 Geometry discretization

The BEM approach allows to find a solution of the Laplace Equation solving (discretizing) an integral Equation all over the boundary of the considered domain. Panel methods due their name to the fact that the domain's boundary is discretized into a series of surface elements (panels): these elements are the basis of the numerical solution of the Laplace equation. Figure 3.1 shows an example of geometry and wake discretization into panels. Usually

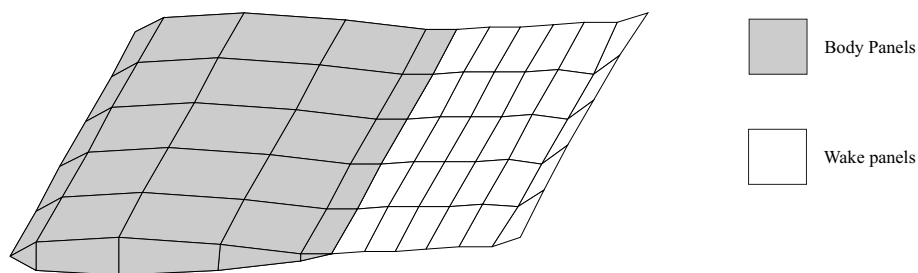


Figure 3.1: Example of body and wake panel discretization.

panels and singularities distributions are approximated using polynomial interpolations. In

the present work, body and wake surfaces are discretized using plane quadrilateral panels, as shown in Figure 3.1. This choice, coupled with zeroth or first order singularities give rise to the so called lower order panels methods: compared to higher order methods they generally require less computational effort and offer a good compromise between accuracy and performances. A shortcoming of the plane panels is that, for complex three-dimensional surfaces (for example with abrupt curvatures), a grid refinement is needed (higher number of panels) to correctly represent the geometry. A rough representation of geometry leads to inaccurate results consequence of the difficulty of appropriately enforcing the no-penetration boundary condition on body surface [17]. In supersonic flows (not taken into account in

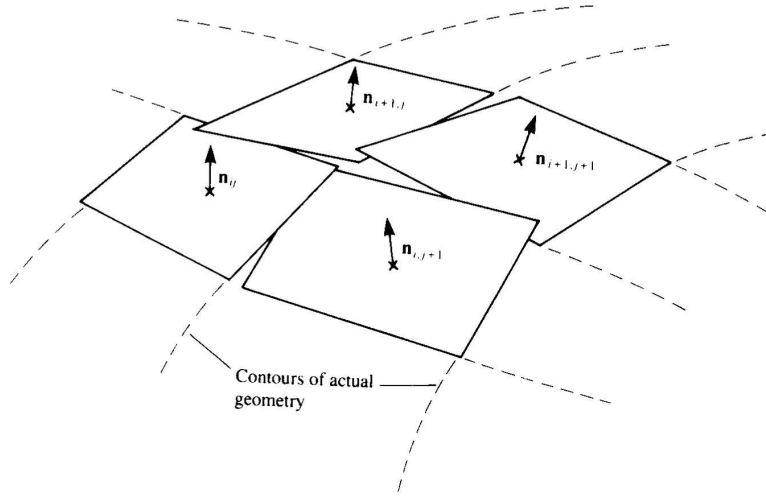


Figure 3.2: Leakage in representing the actual surface with planar panels. From [17].

this work), no discontinuities in the singularity distribution can be accepted: not only it is then necessary to avoid gaps between the panels, but also the order of the singularity has to be high enough to guarantee continuity. In the case of subsonic flows, except in those cases in which gaps between panels are too severe, zeroth-order panels guarantee reasonable approximation of the real geometry. A convergence analysis is always recommended to avoid undesired results due to the gaps between the panels.

3.1.1 Panel geometry

A low order panel method, using the principles of a finite element method, requires the evaluation of surface integrals on quadrilateral surface elements (in the present case the

surface elements are planar); thus, to evaluate aerodynamic loads on a generic body, its surface has to be discretized and converted into a series of planar panels. This is achieved by a multiple step process. First, a grid on the body surface is obtained from the input file. The points are called nodes and they are the corners of the quadrilateral (generally non-planar) elements. The order in which these nodes are connected (connectivity) is important to define the direction of the panel normals: as shown in Figure 3.3, the right hand rule defines the direction of the normal. Body panel nodes coordinates and connectivity are obtained as an input from file and particular care has to be taken to ensure that the nodes order results in an *outward* normal respect to the body. For the wake panels the normal's orientation will be discussed later. However, a quadrilateral element obtained connecting four generic nodes

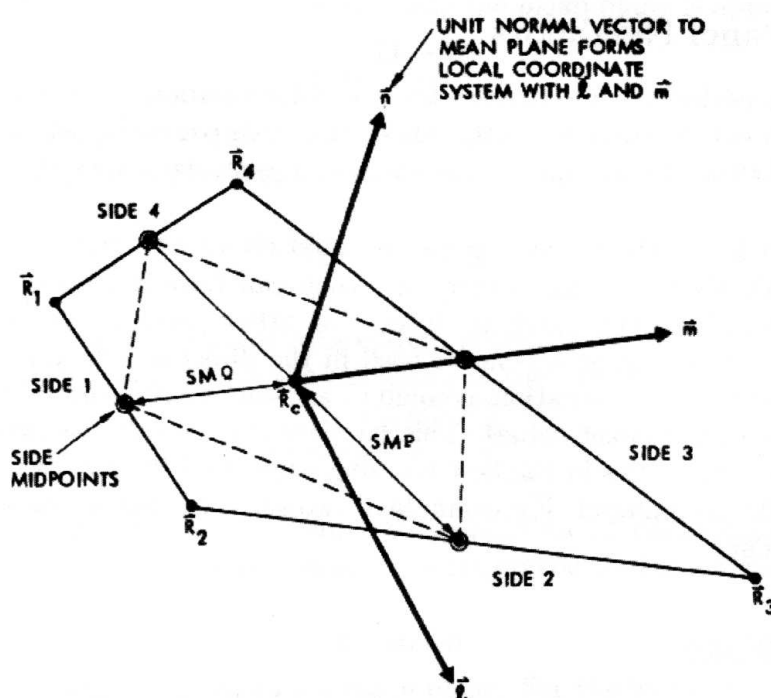


Figure 3.3: Panel geometry and main features. Taken from [24].

is not, in general, planar. This means that to transform a generic quadrilateral element into a planar panel, some precautions have to be taken.

Starting from the four corner points, the two diagonals D_1 and D_2 are first defined (Figure 3.4). The vector product of this diagonals produces a vector normal to the *mean*

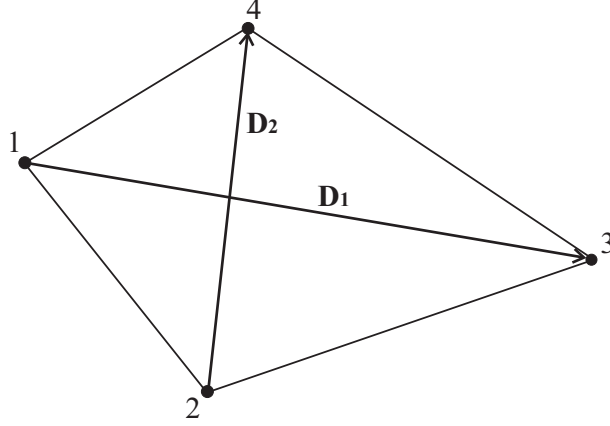


Figure 3.4: Panel geometry and representation of the two diagonals.

plane of the quadrilateral, from which the unit normal vector \mathbf{n} is defined:

$$\mathbf{n} = \frac{\mathbf{D}_1 \times \mathbf{D}_2}{|\mathbf{D}_1 \times \mathbf{D}_2|}. \quad (3.1)$$

It is important to recall that the order of the corner gives the direction of the normal; to have an outward normal \mathbf{D}_1 runs from node 1 to node 3, \mathbf{D}_2 runs from node 2 to node 4. The area A of the element projected onto the mean plane is approximated by:

$$A = \frac{\|\mathbf{D}_1 \times \mathbf{D}_2\|}{2}. \quad (3.2)$$

The control points where the boundary condition is enforced (collocation points) are coincident with the center of the panel, defined as the mean of the four corner points (see Figure 3.3):

$$\mathbf{R}_c = \frac{1}{4} \sum_{i=1}^4 \mathbf{R}_i. \quad (3.3)$$

For every panel, a *local* coordinate system of unit vectors \mathbf{l} , \mathbf{m} , \mathbf{n} is defined; the origin of every local coordinate system is the panel center \mathbf{R}_c . Unit vector \mathbf{n} has already been defined, while the tangential vector \mathbf{m} is directed from \mathbf{R}_c to the mid-point of side 3 (which, as shown in Figure 3.3 connects nodes 3 and 4) and lies on the mean plane (since both the points lie on the mean-plane):

$$\mathbf{m} = \frac{\frac{\mathbf{R}_3 + \mathbf{R}_4}{2} - \mathbf{R}_c}{\left\| \frac{\mathbf{R}_3 + \mathbf{R}_4}{2} - \mathbf{R}_c \right\|}. \quad (3.4)$$

Finally the second tangen vector \mathbf{l} , which completes the reference system, is taken as perpendicular to \mathbf{n} and \mathbf{m} and is obtained by their cross product:

$$\mathbf{l} = \mathbf{m} \times \mathbf{n}. \quad (3.5)$$

Another important parameter to define are the half median lenghts, whose analytical expressions are:

$$SMP = \left\| \frac{\mathbf{R}_2 + \mathbf{R}_3}{2} - \mathbf{R}_c \right\| \quad (3.6)$$

$$SMQ = \left\| \frac{\mathbf{R}_3 + \mathbf{R}_4}{2} - \mathbf{R}_c \right\|. \quad (3.7)$$

They will be useful for the differentiation of the potential on the body surface for the calculation of pressures. The directions of the medians are given by the unit vectors \mathbf{SMP} and \mathbf{SMQ} , expressed by

$$\mathbf{SMP} = \frac{\frac{\mathbf{R}_2 + \mathbf{R}_3}{2} - \mathbf{R}_c}{\left\| \frac{\mathbf{R}_2 + \mathbf{R}_3}{2} - \mathbf{R}_c \right\|} \quad (3.8)$$

$$\mathbf{SMQ} = \frac{\frac{\mathbf{R}_2 + \mathbf{R}_3}{2} - \mathbf{R}_c}{\left\| \frac{\mathbf{R}_2 + \mathbf{R}_3}{2} - \mathbf{R}_c \right\|}. \quad (3.9)$$

Two panels that share two adjacent nodes, also share the same edge midpoints: this means that the medians of two adjacent panels are connected (even though not necessary parallel) and they give a good approximations of the surface distances between panel centers. The quantity $SMP + SMQ$ is used as reference length for the panel: it is generally used to adimensionalize the distance of a point from the panel center.

Wake panels

The discretization procedure presented for body panels geometry is also valid for wake panels. A difference is that for wake panels the orientation is not given as an input, but is set by the panel code. *Edge 4* (Figure 3.3) is always upstream, and *edge 2* downstream. In addition the mean plane is defined as the plane containing *edge 4* and the mid-point of *edge 2*; this way the projected wake panels are cleanly attached to the surface separation line even when the panels are skewed. Finally, concerning the orientation of the normal, there is no

preferential direction. Thus, it is automatically set by internal routines of the code. The only restriction is that wake panels shed by the same trailing edge have concordant normal directions. However, wake normal direction will define the *upper* body panel on trailing edge from which the wake panel is shed. In other words, as will be shown in the following, the shed wake panel normal's direction and the *upper* body trailing edge one will point on the same *semi-space*. The concept of *upper* is then completely arbitrary and needed only to appropriately enforce Kutta condition.

Panel neighbors and patches

Considering a generic panel, a neighbor is a panel that shares one edge (with its two nodes) with the considered panel. Figure 3.5 shows a panel and its neighbors: every panel can have a maximum of four neighbors. The importance of neighbors will be clear in the next sections:

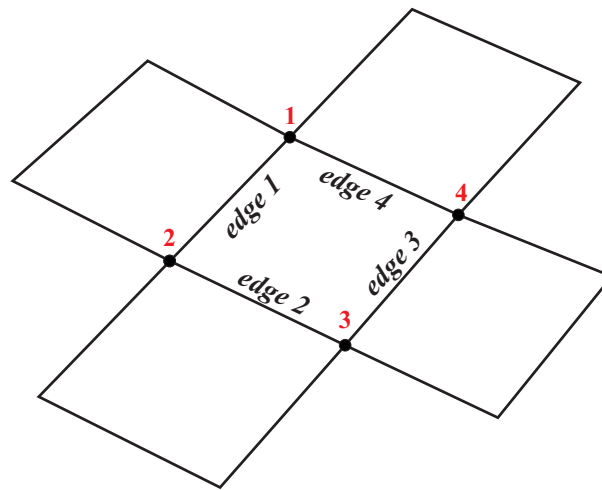


Figure 3.5: A panel with its neighbors. Every neighbor shares one edge and two nodes.

they are no strictly related to the geometry representation, but are used to perform a surface numerical integration of the potential for the evaluation of pressures on a body. For this reason, some exceptions apply whether to consider or not two panels as neighbors: they have to share an edge, but they do not have to be separated by a trailing edge or a sharp corner with a too large angle (in the code this is set to 135 degrees, being angle measured between the two panels' normals).

There are some cases in which two groups of panels are separated by a sharp corner with smaller angles, but are not suitable to be considered as neighbors because a potential differentiation across that corner would lead to inaccurate results. This is the case, for

example, of wing's tip lateral patches (also called *plugs*, see Figure 3.6). This is where the definition of *patches* becomes useful. Patches are just group of panels: from input, the user decides to which patch every panel belongs. If two panels belong to different patches and they share an edge, they will be considered neighbors only if the angle between the panels normals is smaller than another fixed value (in the implementation, less than 45 degrees).

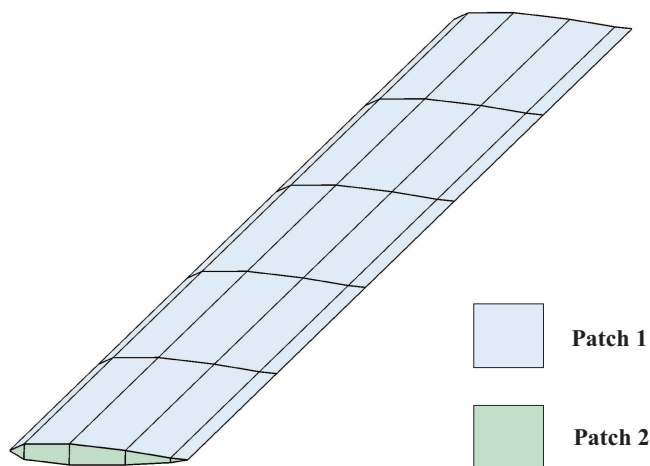


Figure 3.6: A simple mesh on a rectangular finite wing. The two different patches are plotted in different colors.

For complex surfaces, it is not always possible to guarantee perfect abutment between panels. In general this does not represent a problem and also partial abutments are allowed (Figure 3.7), assumed that gaps are not too severe. The drawback is that panels that do not completely share an edge, even if they partially abut on one edge, will not be considered as neighbors and the potential differentiation will not be carried out between them. The choice of the geometry discretization is up to the operator's needs, that in some cases has to make a compromise between accuracy of the geometry representation and accuracy of the potential differentiation.

3.2 Singularities

The analytical formulation of a BEM is based on the distribution of singularities (generally doublets and sources) all over the body and wake surface. Knowing the intensities of these singularity distribution allows one to evaluate the perturbation potential φ in the domain \mathcal{V} .

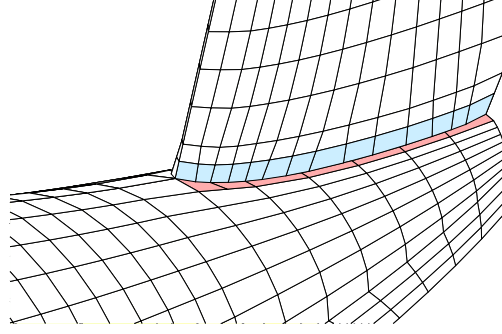


Figure 3.7: Details of the joint between fuselage and vertical fin. The patches of the two different parts do not abut (the interface is highlighted with two different colors): this is allowed if the gaps between the panels are not too severe.

As briefly introduced in the previous section, after discretizing the surfaces with quadrilateral panels, a singularity intensity distribution has to be specified all over these panels; a polynomial interpolation is used. The order of the polynomial interpolation has to be consistent with the order of the panels; using low order panels coupled with high order singularities or vice-versa, will only increase computational time without a significant improvement of accuracy. In this work, zeroth-order singularity distributions are used: this means that the strength of the singularities is constant on each panel. Using zero-order singularities coupled with plane panels allows one to calculate the integrals in a closed form, avoiding numerical integrations that usually require more computational effort and is a further source of error. The expressions to evaluate perturbation velocity potential due to the induction of a plane quadrilateral panel with a constant strength singularity distribution, have been obtained by Hess and Smith [16] and are listed in Appendix A.

3.2.1 Farfield

To improve code performances, if the distance between the induced point and the inducing panel center is larger than a certain (user-defined) value (in general this value is expressed as a multiple of the panel dimension $SMP + SMQ$), the used induction formulas will switch to those of a concentrated singularity (see Appendix A). It can be shown that increasing the distance between induced point and inducing panel, the induced potential difference between the original and the far-field formulas decreases. This difference depends on the singularity type as well, and is up to the user to carry out a sensibility analysis to set the most suitable farfield distance value.

3.3 Linear system

In a numerical panel method, the body surface S_B is discretized with N panels and the wake surface S_W with N_W panels. Body panels are characterized by a distribution of sources $\sigma(\mathbf{y})$ and doublets $\mu(\mathbf{y})$, while for the wake panels only doublets are necessary (the normal velocity is continue across the wake). Let \mathbf{y} indicate a generic point of wake and body surfaces. Assuming zero-order singularities, σ and μ are constant on each panel. In order to reduce the integral formulation to a set of linear algebraic equations, it is then necessary to enforce the boundary condition at each *collocation point* (coincident with the centers of the panels). In the present work, the perturbation potential *inside* the body is set to zero (homogeneous Dirichlet boundary condition) and enforcing this condition at the center of a generic k -th panel (\mathbf{x}_k), Equations 2.55 can be written as:

$$\begin{cases} \sum_{i=1}^N B_{ki} \sigma_i + \sum_{i=1}^N A_{ki} \mu_i + \sum_{j=1}^{N_W} F_{kj} \mu_j^w = 0 \\ \sigma_k = -\mathbf{V}_{\infty, k} \cdot \mathbf{n}_k \end{cases} \quad k = 1, \dots, N \quad (3.10)$$

where \mathbf{n}_i is the i -th panel unit normal vector, V_∞ has to be evaluated in the i -th collocation point, and

$$B_{ki} = -\frac{1}{4\pi} \int_{S_{B_i}} \left(\frac{1}{\|\mathbf{y} - \mathbf{x}_k\|} \right) dS_{B_i}(\mathbf{y}) \quad (3.11)$$

$$A_{ki} = \frac{1}{4\pi} \int_{S_{B_i}} \frac{\partial}{\partial n} \left(\frac{1}{\|\mathbf{y} - \mathbf{x}_k\|} \right) dS_{B_i}(\mathbf{y}) \quad (3.12)$$

$$F_{kj} = \frac{1}{4\pi} \int_{S_{w_j}} \frac{\partial}{\partial n} \left(\frac{1}{\|\mathbf{y} - \mathbf{x}_k\|} \right) dS_{w_j}(\mathbf{y}). \quad (3.13)$$

Equation 3.10 becomes a linear algebraic system of N equations that, for this particular choice of panels and singularities, means one equation for each collocation point. The strengths of the sources are easily evaluated by the second set of equations 3.10. In Table 3.3 are reported the dimensions of the aerodynamics coefficient matrices, as well as the disposition of the coefficients inside the matrices. Notice that, the intensity of the wake doublets not attached to the trailing edge are known from the previous timesteps 2.37.

The only unknowns are the N body doublets intensities μ_i and the N_{TE} intensities of the wake doublets attached to the trailing edge, where N_{TE} is the number of panels on the

Aerodynamic Influence Coefficient Matrix	Dimensions	Influence Coefficients
B	$N \times N$	B_{ki} = influence of body source i over panel k
A	$N \times N$	A_{ki} = influence of body doublet i over panel k
F	$N \times N_W$	F_{kj} = influence of wake doublet j over panel k

Table 3.1: Aerodynamic Influence Coefficient Matrices.

trailing edge. From now on, the wake panels attached to the trailing edge will be defined as *near wake*, while all the other wake panels will be the *far wake*, as shown in Figure 3.8. System 3.10 can be written again separating the contributions of near wake and far wake:

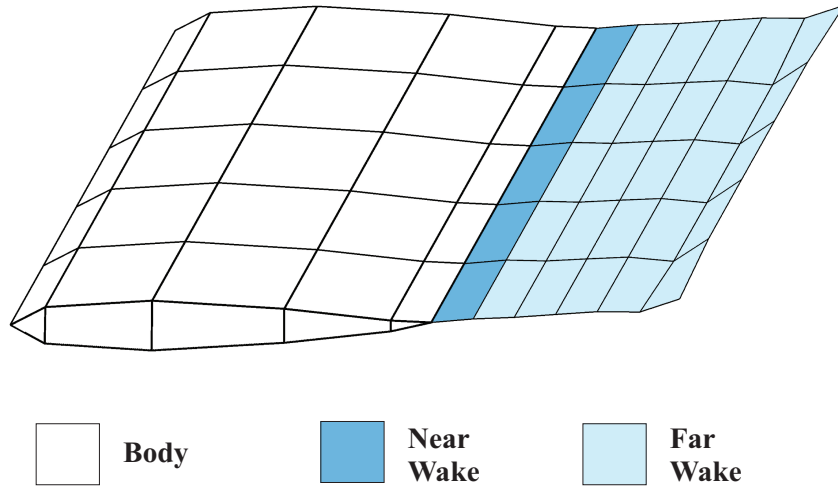


Figure 3.8: Representation of near and far wake.

$$\left\{ \begin{array}{l} \sum_{i=1}^N A_{ki} \mu_i + \sum_{l=1}^{N_{TE}} C_{kl} \tilde{\mu}_l = - \sum_{j=1}^{N_{FW}} D_{kj} \mu_j^* - \sum_{i=1}^N B_{ki} \sigma_i \\ \sigma_k = -\mathbf{V}_{\infty, k} \cdot \mathbf{n}_k \end{array} \right. \quad k = 1, \dots, N \quad (3.14)$$

where

$$C_{kj} = \frac{1}{4\pi} \int_{S_{w_j}^N} \frac{\partial}{\partial n} \left(\frac{1}{\|\mathbf{y} - \mathbf{x}_k\|} \right) dS_{w_j}^N(\mathbf{y}) \quad (3.15)$$

$$D_{kl} = \frac{1}{4\pi} \int_{S_{w_l}^F} \frac{\partial}{\partial n} \left(\frac{1}{\|\mathbf{y} - \mathbf{x}_k\|} \right) dS_{w_l}^F(\mathbf{y}) \quad (3.16)$$

and $\tilde{\mu}$ and μ^* represent the near and far wake doublets intensity, respectively, whereas N_{FW} is the number of far wake panels. Indicating with S_F^W and S_N^W the surfaces of far wake and near wake respectively, the symbols $S_{w_l}^F$ and $S_{w_j}^N$ are the surfaces of the l -th panel of the far wake and of the j -th panel of the near wake respectively.

The meaning of the coefficients is summarized in Table 3.2. The right hand side of the first equation of the system is known. To solve the linear system, the number of unknowns has to be reduced from $N + N_{TE}$ to N . This is achieved imposing the so-called Kutta condition, that sets a relation between the intensity of the body doublets on the trailing edge and the doublet intensities of the near wake. There are actually different ways to *close* the problem. In the following the most common approach (regular Kutta condition) is shown, whereas advanced way to impose the condition are outlined later in 3.7. As shown in Figure 3.9, indicating with μ_j^{up} and μ_j^{down} the body doublets on the same trailing edge segment j , the following relation (expressing the so called Kutta-Joukowski condition, see Section 2.7 for details) is imposed:

$$\tilde{\mu}_j = \mu_j^{up} - \mu_j^{down}. \quad (3.17)$$

It is possible to combine matrix A and C to include the Kutta condition in a $N \times N$ matrix \tilde{A} , such that:

$$\left\{ \begin{array}{ll} \tilde{A}_{ik} = A_{ik} & \text{if panel } k \text{ is not a trailing edge panel} \\ \tilde{A}_{ik} = A_{ik} + C_{il_k} & \text{if panel } k \text{ is a trailing edge } \textit{upper} \text{ panel} \\ \tilde{A}_{ik} = A_{ik} - C_{il_k} & \text{if panel } k \text{ is a trailing edge } \textit{lower} \text{ panel} \end{array} \right. \quad (3.18)$$

Aerodynamic Influence Coefficient Matrix	Dimensions	Influence Coefficients
B	$N \times N$	B_{ki} = influence of body source i over panel k
A	$N \times N$	A_{ki} = influence of body doublet i over panel k
C	$N \times N_{TE}$	C_{kj} = influence of near wake doublet j over panel k
D	$N \times N_{FW}$	D_{kl} = influence of far wake doublet l over panel k

Table 3.2: Aerodynamic Influence Coefficient Matrices, separating the contributions of near wake and far wake.

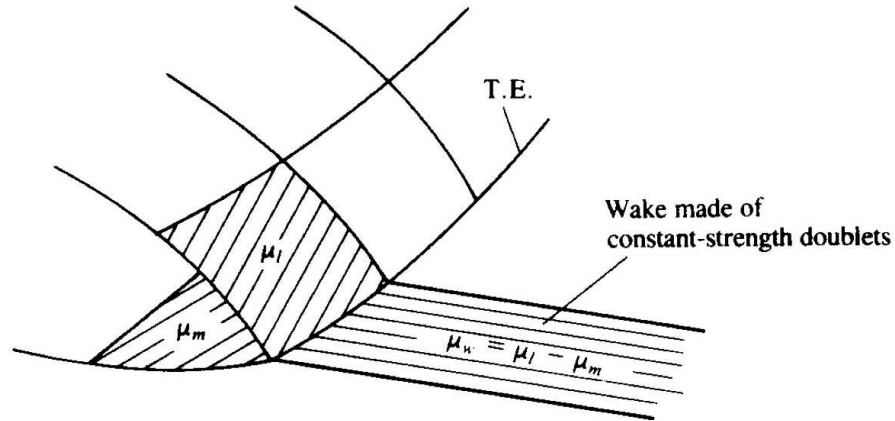


Figure 3.9: Near wake doublets intensities obtained as difference of the intensities of the correspondent body doublets on trailing edge. Taken from [17]. This is the regular (linear) Kutta condition.

where l_k is an index used to indicate the l -th trailing edge segment corresponding to the k -th body panel (when this panel is on the trailing edge). Notice again, that the *upper* and *lower* panels are defined once the wake normal is set: the upper panel is the one having its normal pointing in the same of the domain as the wake's one (Figure 3.10).

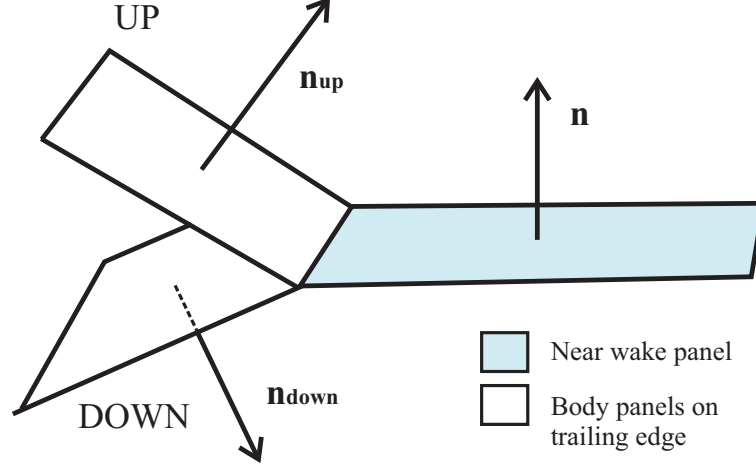


Figure 3.10: Upper and lower body panels on trailing edge, and shed wake panel. The body panel with the normal directed as the wake's panel normal is defined as *up* panel, while the other is the *down* panel.

Enforcing Kutta condition, the system has been reduced to an algebraic linear system of N equations in N unknowns:

$$\begin{cases} \sum_{i=1}^N \tilde{A}_{ki} \mu_i = - \sum_{j=1}^{N_{FW}} D_{kj} \mu_j^* - \sum_{i=1}^N B_{ki} \sigma_i \\ \sigma_k = -\mathbf{V}_{\infty,k} \cdot \mathbf{n}_k \end{cases} \quad k = 1, \dots, N \quad (3.19)$$

Solving the system, it is possible to obtain the unknown *array* $\boldsymbol{\mu}$ and from relation 3.17 the intensities of the near wake doublets are determined. Once the system is solved, all the singularities intensities of the problem are known and it is possible to obtain the value of the velocity potential all over the domain.

3.4 Potential wake: vortex desingularization

As explained in the previous chapters, the potential wake is a thin region that contains vorticity and that has to be excluded from the field domain (boundary surface). From the

definition of vorticity (Section 2.1), using identity

$$\nabla \cdot (\nabla \times \mathbf{a}) = 0, \quad (3.20)$$

where \mathbf{a} is a generic vector, immediately follows

$$\nabla \cdot \boldsymbol{\omega} = 0; \quad (3.21)$$

the vorticity field is thus solenoidal (zero divergence). To describe vorticity in a volume, it is often useful to give the definition of *vortex lines* as vorticity field lines that are parallel to the vorticity vector at every point of the domain. Vortex lines passing through a closed curve in space form a *vortex tube* and a vortex tube with infinitesimal cross section is called *vortex filament* (see [17]).

A fundamental consequence of the solenoidal behaviour of the vorticity field is that, for every vortex tube, the velocity circulation Γ around any closed curve belonging to the wall of the vortex tube is constant. This can be easily proven considering a portion of a vortex

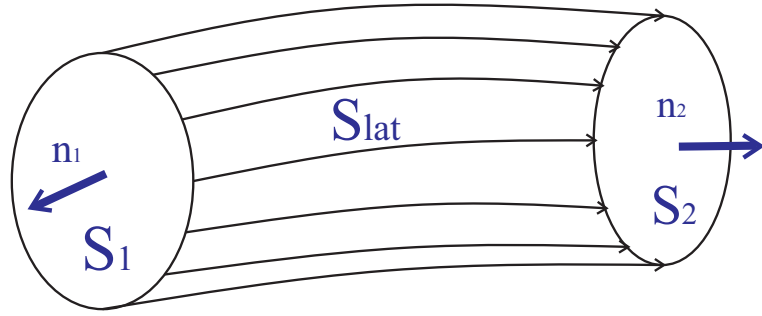


Figure 3.11: portion of vortex tube between two cross-sections.

tube between two cross-sections, as in Figure 3.11. Because the vorticity field is solenoidal, considering the volume of the vortex tube portion it is:

$$\int_{\mathcal{V}} \nabla \cdot \boldsymbol{\omega} d\mathcal{V} = 0 \quad (3.22)$$

and applying the Divergence theorem

$$\int_{\mathcal{V}} \nabla \cdot \boldsymbol{\omega} d\mathcal{V} = \int_{S=\partial\mathcal{V}} \boldsymbol{\omega} \cdot \mathbf{n} dS \quad (3.23)$$

the following result is obtained:

$$\int_{S=\partial\mathcal{V}} \boldsymbol{\omega} \cdot \mathbf{n} dS = 0. \quad (3.24)$$

According to the definition of vortex tube, there is no vorticity flux through the lateral surface \mathcal{S}_{lat} , so Equation 3.24 includes just the contributions of the two cross-sections and becomes:

$$\int_{\mathcal{S}_1} \boldsymbol{\omega}_1 \cdot \mathbf{n}_1 d\mathcal{S} = \int_{\mathcal{S}_2} \boldsymbol{\omega}_2 \cdot \mathbf{n}_2 d\mathcal{S}. \quad (3.25)$$

Equation 3.25 is a purely kinematic relation, consequence of the divergence free property enjoyed by vorticity field. Applying Stokes theorem:

$$\int_{\mathcal{C}=\partial\mathcal{S}} \mathbf{V} \cdot d\mathbf{l} = \int_{\mathcal{S}} (\nabla \times \mathbf{V}) \cdot \mathbf{n} d\mathcal{S} \quad (3.26)$$

using the definition of vorticity and recalling the results obtained in Equation 3.25, the circulation of a vortex tube is constant for every section:

$$\Gamma = \oint_{\mathcal{C}} \mathbf{V} \cdot d\mathbf{l} = \oint_{\mathcal{S}} \boldsymbol{\omega} \cdot \mathbf{n} d\mathcal{S} = \text{const.} \quad (3.27)$$

An important remark is that Stokes theorem is valid only if the region enclosed by the boundary \mathcal{C} is *simply connected*.

A vortex filament will be considered, by definition, as a vortex tube of finite strength whose cross-section has been squeezed to zero. The vorticity vector is parallel to the direction of the filament and because the product $\boldsymbol{\omega} \cdot \mathbf{n} d\mathcal{S}$ is constant, as the cross-section goes to zero the vorticity goes to infinity, in such way to keep that product constant. A vortex filament is thus a model of vortex where an infinite vorticity (whose direction is parallel to the vortex filament) is concentrated along a filament of zero cross-section [17]. As shown later, this will be very useful to represent the potential wake.

3.4.1 Kelvin's theorem

Considering a closed material circuit $\mathcal{C}(t)$ (formed by the same fluids particles), from Equation 3.27 the time derivative of the circulation around this circuit can be expressed as:

$$\frac{d\Gamma}{dt} = \frac{d}{dt} \oint_{\mathcal{C}(t)} \mathbf{V} \cdot d\mathbf{l}. \quad (3.28)$$

As circuit $\mathcal{C}(t)$ is a material circuit, Reynolds transport theorem [8] can be applied, leading to

$$\frac{d\Gamma}{dt} = \oint_{\mathcal{C}(t)} \left(\frac{d\mathbf{V}}{dt} + \mathbf{V} \cdot \nabla \mathbf{V} \right) \cdot d\mathbf{l}; \quad (3.29)$$

using the Momentum equation, Equation 3.29 becomes

$$\frac{d\Gamma}{dt} = \oint_{\mathcal{C}(t)} \left(\mathbf{f} - \frac{1}{\rho} \nabla p + \nu \nabla^2 \mathbf{V} \right) \cdot d\mathbf{l}. \quad (3.30)$$

Neglecting body forces \mathbf{f} , considering the fluid as inviscid and from the identity $\nabla p \cdot d\mathbf{l} = dp$, Equation 3.30 can be rewritten as

$$\frac{d\Gamma}{dt} = \oint_{C(t)} -\frac{1}{\rho} dp. \quad (3.31)$$

A fundamental result can be obtained in case of *barotropic* flows (where density is a function of pressure only), being an incompressible flow a particular case of. In this case Equation 3.31 simply becomes:

$$\frac{d\Gamma}{dt} = 0. \quad (3.32)$$

This is a fundamental result, also known as Kelvin's theorem, that states that for an inviscid, barotropic fluid with no body forces the circulation is a conservative property. This guarantees that an irrotational incompressible flow remains irrotational during the motion.

3.4.2 Velocity induced by a vorticity distribution

Applying curl to $\boldsymbol{\omega}$ and recalling the definition of $\boldsymbol{\omega}$, it holds that

$$\nabla \times \boldsymbol{\omega} = -\nabla \times (\nabla \times \mathbf{V}) = \nabla (\nabla \cdot \mathbf{V}) - \nabla^2 \mathbf{V} \quad (3.33)$$

For an incompressible flow, as $\nabla \cdot \mathbf{V} = 0$, the following identity is obtained

$$\nabla \times \boldsymbol{\omega} = -\nabla^2 \mathbf{V} \quad (3.34)$$

and it can be solved using Green's identity [19], leading to

$$\mathbf{v}(\mathbf{x}) = \frac{1}{4\pi} \int_{\mathcal{V}} \nabla \times \frac{\boldsymbol{\omega}(\mathbf{y})}{\|\mathbf{x} - \mathbf{y}\|} d\mathcal{V}(\mathbf{y}). \quad (3.35)$$

Equation 3.35 represents the velocity in a generic point P due to a vorticity distribution in \mathcal{V} . A singularity is present in case P belongs to \mathcal{V} : in this case the integral cannot be evaluated using the classical theory of integration, but following Hadamard's definition it admits a finite-part if the limit process is carried out properly [26].

3.4.3 Induction of a vorticity filament: Biot-Savart

Indicating with $d\mathbf{l}$ a unit vector parallel to the filament direction, domain \mathcal{V} can be written as

$$d\mathcal{V}(\mathbf{y}) = d\mathcal{S} \, dl(\mathbf{y}) \quad (3.36)$$

where

$$dl(\mathbf{y}) = \|d\mathbf{l}(\mathbf{y})\| \quad (3.37)$$

and, consequently, Equation 3.35 can be rewritten as

$$\mathbf{v}(\mathbf{x}) = \frac{1}{4\pi} \int_{\mathcal{V}} \nabla \times \frac{\boldsymbol{\omega}(\mathbf{y})}{\|\mathbf{x} - \mathbf{y}\|} dS \, dl(\mathbf{y}). \quad (3.38)$$

From the definition of circulation Γ , remembering that $\boldsymbol{\omega} \cdot d\mathbf{l} = 0$, it is possible to show that Equation 3.38 can be expressed in the following form [17]:

$$\mathbf{v}(\mathbf{x}) = \frac{\Gamma}{4\pi} \int \frac{d\mathbf{l}(\mathbf{y}) \times (\mathbf{x} - \mathbf{y})}{\|\mathbf{x} - \mathbf{y}\|^3}. \quad (3.39)$$

Equation 3.39 can be written in differential form, expressing the velocity induction of a vortex filament with infinitesimal length:

$$\mathbf{v}(\mathbf{x}) = \frac{\Gamma}{4\pi} \frac{d\mathbf{l}(\mathbf{y}) \times (\mathbf{x} - \mathbf{y})}{\|\mathbf{x} - \mathbf{y}\|^3}. \quad (3.40)$$

For its analogy with the formula in electromagnetism theory, Equation 3.40 is called Biot-Savart law.

3.4.4 Straight vortex segment

Even if a vortex filament cannot end inside the domain, it is useful to analyze the case of the velocity induced by a straight vortex segment. The analytical expression of the induction is obtained integrating Equation 3.39 along the length of the straight filament. Figure 3.12 shows the symbology used in the formula. Following Leishmann [20], the expression of the velocity induction can be written as:

$$\mathbf{v}(\mathbf{x}) = \frac{\Gamma}{4\pi h} (\cos \theta_1 - \cos \theta_2) \mathbf{e}_{12} \quad (3.41)$$

where

$$\left\{ \begin{array}{l} \mathbf{e}_{12} = \frac{\mathbf{l}_{12} \times \mathbf{r}_1}{|\mathbf{l}_{12} \times \mathbf{r}_1|} \\ h = r_1 \sin \theta_1 = r_2 \sin \theta_2 \\ \cos \theta_1 = \frac{\mathbf{l}_{12} \cdot \mathbf{r}_1}{|\mathbf{l}_{12}| |\mathbf{r}_1|} \\ \cos \theta_2 = \frac{\mathbf{l}_{12} \cdot \mathbf{r}_2}{|\mathbf{l}_{12}| |\mathbf{r}_2|} \end{array} \right. \quad (3.42)$$

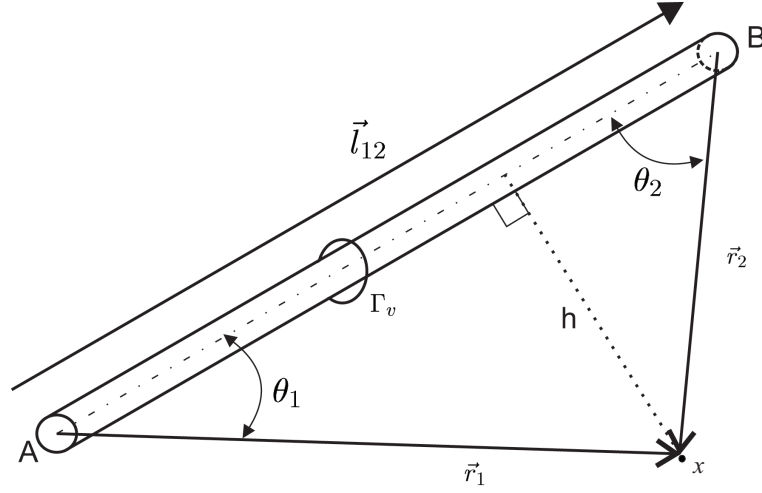


Figure 3.12: Definition of symbols used in the formulation of the induction of a finite length straight vortex filament.

3.4.5 Doublet - vortex equivalence

It is possible to prove that the velocity induced by a constant strength doublet panel is equal to the velocity induced by a vortex ring whose sides are the boundaries of the doublet panel. The proof of the equivalence, which is not present in this work, was provided by Hess and a simplified derivation can be found in [17]. Figure 3.13 summarizes the principles of this equivalence.

What is important to notice is that while the induced velocity is the same, the order of

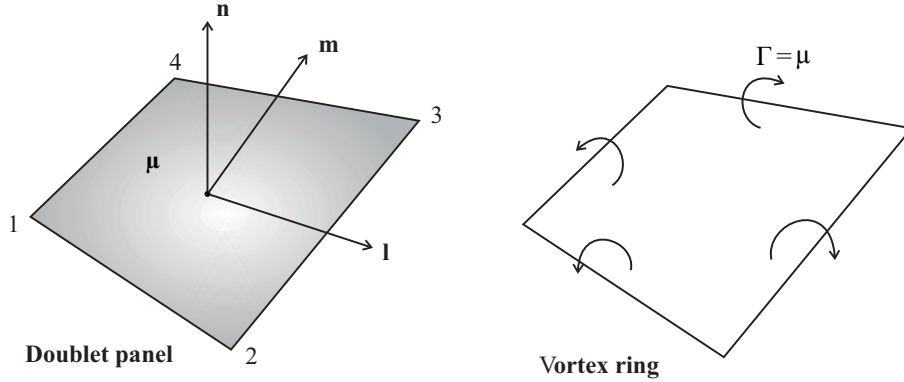


Figure 3.13: Equivalence between a quadrilateral doublet panel and a vortex ring.

the singularity of the velocity induction of the two formulations is different: the singularity of a vortex ring is one order less than the singularity of a doublet surface distribution and

this can be extremely important in a numerical code. Thanks to this equivalence, only for the velocity induction, the wake doublets will be considered as vortex rings and because the panels are quadrilateral, the induced velocity will be the sum of the contributions of the four straight vortex segments of the panel.

3.4.6 Vortex singularity

Even if the order of the singularity of the velocity induction of a constant strength quadrilateral doublet is reduced using the analogy with the vortex ring, as the induced point approaches the inducing filament, velocity tends to infinity. For example, considering the tangential velocity V_θ induced by an infinite straight vortex filament of constant strength Γ (it can be easily obtained from 3.41),

$$V_\theta = \frac{\Gamma}{2\pi r} \quad (3.43)$$

it is not hard to see that velocity goes to infinity as the distance r between the induced point and the vortex filament approaches zero.

Panel codes are based on the assumption that the flow is potential and this means that the effects of viscosity are not taken into account. When the distance between the induced point and the vortex is sufficiently large, a vortex filament can be a good mathematical model to numerically represent the induction of concentrated vorticity in a *real* flow.

However, when the point approaches the filament, the model is no longer accurate, because it does not take into account the smoothing effects of viscosity that occur in a viscous flow, especially in areas of highly concentrated vorticity where these effects are predominant.

3.4.7 Vortex regularization

A more refined analytical model would be a vortex with a finite cross-section of radius r_c : inside the core radius, the velocity goes to zero as the induced point approaches the vortex center, simulating the smoothing effect of viscosity, while outside the core the velocity approximates the Biot-Savart law. This is achieved introducing a regularization function. Extensive information about vortex regularization can be found in [32]. In this work only the general outline will be presented.

For a straight vortex filament it is already been said that infinite vorticity is concentrated on the vortex line: this can be mathematically expressed with

$$\boldsymbol{\omega}(\mathbf{x}) = \Gamma \int \delta(\mathbf{y} - \mathbf{x}) d\mathbf{l}(\mathbf{y}) \quad (3.44)$$

where $\delta(\mathbf{x})$ represents the Dirac delta function. The principle of vortex regularization is to introduce a regularization function ζ_{r_c} to smooth the vorticity distribution:

$$\boldsymbol{\omega}_{r_c}(\mathbf{x}) = \zeta_{r_c}(\mathbf{y}) * \boldsymbol{\omega}_{r_c}(\mathbf{x}) = \Gamma \int \zeta_{r_c}(\mathbf{y} - \mathbf{x}) d\mathbf{l}(\mathbf{y}) \quad (3.45)$$

where $*$ is the convolution product and r_c is the smoothing radius. Function ζ_{r_c} defines the vorticity distribution within the core of the vortex filament. Following Equation 3.38 it is possible to find the velocity induction. In [32] a series of conditions that regularization functions have to satisfy as well as some examples of regularization functions are thoroughly explained and analyzed. The choice of the regularization function is important in all those cases in which a wake passes very close to a body (or parts of the distorted wake tend to compenetrates), modifying the forces on the body itself: forces can change depending on the choice of the regularization function and a sensibility analysis, coupled with the use of other tools such as experiments or simulations with different codes, is highly recommended.

In this work, a vortex regularization based on two-dimensional *Vatistas* model [20] is adopted. This regularization affects the velocity induction of a vortex segment in its integrated form, avoiding numerical integrations of Equation 3.38 and improving the computational performances. The aim of this work does not consider the study of transients with severe body-wake impingements, so the choice of this model is more than appropriate.

The regularized vortex induction can be written as

$$\mathbf{v}(\mathbf{x}_P) = \frac{\Gamma}{4\pi} \frac{h}{(r_c^{2n} + h^{2n})^{\frac{1}{n}}} (\cos \theta_1 - \cos \theta_2) \mathbf{e}_{12}, \quad (3.46)$$

where r_c represents the core radius and n is an index that defines the regularization function ($n = 1$ or $n = 2$). It is important to remark that this choice of regularization is an extension of the two-dimensional theory, so it has its drawbacks. When r_1 , r_2 or l_{12} have zero norm, quantities h , $\cos \theta_1$ e $\cos \theta_2$ are not defined: it is necessary to exclude this cases forcing the induction to zero when at least one of those vectors has zero norm. This is just a numerical adjustment: in fact when $r_1 = 0$ or $r_2 = 0$ the induced point lies on the vortex filament, so the induction is zero by definition, whereas if l_{12} has zero norm then the filament collapses in a point and the induction is again zero.

3.5 Force evaluation: Bernoulli theorem

Once the linear system is solved, it is possible to evaluate the fluid pressure at every point of the domain using Bernoulli theorem in its unsteady form. Considering a point of the domain

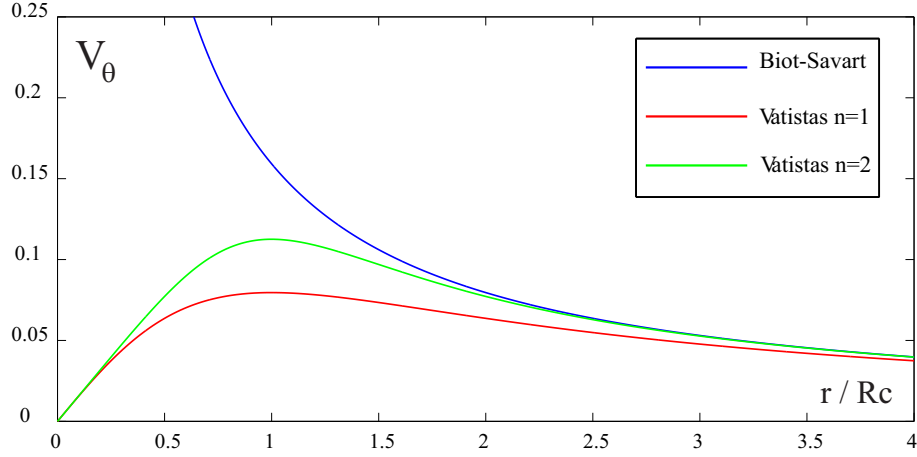


Figure 3.14: Comparison between the two-dimensional *Biot-Savart* law and the *Vatistas* two-dimensional model.

where the fluid properties are $p = p_{ref}$ and $\mathbf{V} = \mathbf{V}_{ref}$, from Equation 2.12 specified in a body fixed frame of reference, for a generic point on the body surface it holds

$$\frac{p_{ref}}{\rho} + \frac{\|\mathbf{V}_{ref}\|^2}{2} = \frac{p}{\rho} + \frac{\partial\varphi}{\partial t} + \frac{\|\mathbf{V}_w - \mathbf{V}_b + \mathbf{v}_p\|^2}{2} \quad (3.47)$$

where

$$\begin{aligned} \mathbf{V}_w &= \text{wind speed} \\ \mathbf{V}_b &= \text{velocity of the moving body} \\ \mathbf{v}_p &= \text{perturbation velocity} \\ \mathbf{V}_{ref} &= \text{reference velocity} \end{aligned} \quad (3.48)$$

In Equation 3.47 the total velocity on the body surface has been decomposed in the contributions of the perturbation velocity \mathbf{v}_p , of the wind velocity \mathbf{V}_w and of the velocity due to the body's motion. The norms of the previous quantities will be indicated, respectively, with V_w , V_b , v_p and V_{ref} .

From Equation 3.47 it is possible to obtain an expression for the pressure difference $p - p_{ref}$:

$$\frac{p - p_{ref}}{\rho} = -\frac{\partial\varphi}{\partial t} + \frac{\|\mathbf{V}_{ref}\|^2}{2} - \frac{\|\mathbf{V}_w - \mathbf{V}_b + \mathbf{v}_p\|^2}{2} \quad (3.49)$$

As the first aim of the panel code is to evaluate forces and moments that the fluid exerts on the body, the evaluation of all the quantities involved in Equation 3.49 will be performed on the body surface, specifically on the control points of every panel (panel centers). For a closed body completely immersed in a flow the value of p_{ref} is not important, as long as it

is the same for every control point. Remembering that from Dirichlet boundary condition is $\varphi_{in} = 0$, the value of the perturbation potential on the body surface is

$$\varphi = \mu \quad (3.50)$$

and from the definition of velocity potential

$$\mathbf{v}_p = \nabla \mu. \quad (3.51)$$

Equation 3.49 becomes

$$\frac{p - p_{ref}}{\rho} = -\frac{\partial \varphi}{\partial t} + \frac{||\mathbf{V}_{ref}||^2}{2} - \frac{||\mathbf{V}_w - \mathbf{V}_b + \nabla \mu||^2}{2}. \quad (3.52)$$

The differentiation of the potential on the body panels is carried out using a finite differences scheme. Details of the procedure will be presented in the next section.

3.6 Surface differentiation of perturbation potential

The expression of the perturbation velocity in panel local coordinate system can be written as

$$\mathbf{v}_p = \nabla \varphi = \frac{\partial \varphi}{\partial l} \mathbf{e}_l + \frac{\partial \varphi}{\partial m} \mathbf{e}_m + \frac{\partial \varphi}{\partial n} \mathbf{e}_n \quad (3.53)$$

where \mathbf{e}_l , \mathbf{e}_m and \mathbf{e}_n are the unit vectors of the local coordinate system. To evaluate the aerodynamic loads on a body, the perturbation velocity has to be evaluated on the body surface. The perturbation potential on the body surface is $\varphi = \mu$, where all the body doublets intensities μ are known from the solution of the linear system. Recalling the definition of source intensity, for the normal perturbation velocity it holds $v_n = \sigma$. Thus Equation 3.53 can be rewritten as

$$\mathbf{v}_p|_{body} = \frac{\partial \mu}{\partial l} \mathbf{e}_l + \frac{\partial \mu}{\partial m} \mathbf{e}_m + \sigma \mathbf{e}_n. \quad (3.54)$$

To compute the tangential velocities a differentiation of the doublet intensities has to be performed. In general to evaluate the tangential velocity in a certain direction on the collocation point of a certain panel that will be indicated with the subscript c (current), two neighbor panels along that direction have to be considered and they will be indicated with p and n (previous and next). By construction, two neighbors share an edge and the midpoint of this edge is the same for both panels: the edge medians are, thus, two adjacent segments and will be used as an average of the distance between the panels centers.

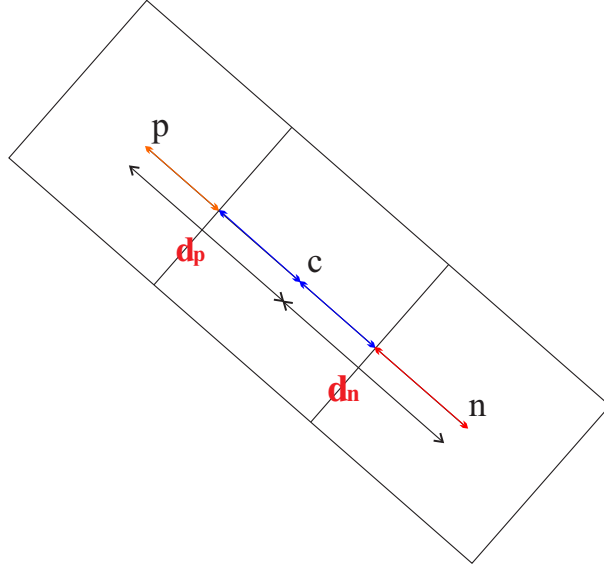


Figure 3.15: Neighbors along one direction with their medians, that are taken as reference for the distance between panel centers.

Figure 3.15 shows the disposition of the panels and the edge medians for one direction. Assuming a quadratic fit along a generic direction s of the doublet distribution, as shown in Figure 3.16, the following relations can be obtained:

$$\mu = ax^2 + bx + c \quad (3.55)$$

where

$$\left\{ \begin{array}{l} a = \frac{\mu_p x_n - \mu_n x_p - \mu_c (x_n - x_p)}{x_p x_n (x_n - x_p)} \\ b = \frac{\mu_p x_n^2 - \mu_n x_p^2 - \mu_c (x_n^2 - x_p^2)}{x_p x_n (x_n - x_p)} \\ c = \mu_c \end{array} \right. \quad (3.56)$$

Following Figure 3.16, Equation 3.56 can be rewritten as

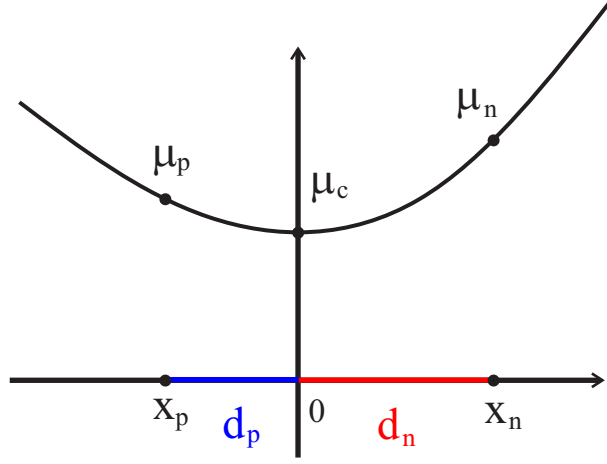


Figure 3.16: Quadratic interpolation between intensities of neighbor panels along one direction.

$$\begin{cases} a = -\frac{\mu_p d_n + \mu_n d_p - \mu_c(d_n + d_p)}{d_p d_n (d_n + d_p)} \\ b = -\frac{\mu_p d_n^2 + \mu_n d_p^2 - \mu_c(d_n^2 - d_p^2)}{d_p d_n (d_n + d_p)} \\ c = \mu_c \end{cases} \quad (3.57)$$

Calculating the first derivative in $x = 0$ (current panel collocation point) gives

$$\left. \frac{\partial \mu}{\partial x} \right|_{x=0} = b. \quad (3.58)$$

The derivatives can be calculated along the two directions \mathbf{SMP}_c and \mathbf{SMQ}_c : as the neighbor panels abut along one edge, the sum of the length of the corresponding abutting half median will be taken as d_n and d_p (according to the panel orientation) for the directions \mathbf{SMP}_c and \mathbf{SMQ}_c .

As the derivatives along \mathbf{SMP}_c and \mathbf{SMQ}_c are easier to obtain, they can be converted into derivatives along \mathbf{e}_l and \mathbf{e}_m , following:

$$\frac{\partial \mu}{\partial m} = \frac{\partial \mu}{\partial_{SMQ}}$$

$$\frac{\partial \mu}{\partial l} = \frac{\mathbf{SMP} \frac{\partial \mu}{\partial_{SMP}} - \mathbf{SMP} \cdot \mathbf{e}_m \frac{\partial \mu}{\partial_{SMQ}}}{\mathbf{SMP} \cdot \mathbf{e}_l}$$

In case a neighbor is not available, a decentralized formula is used or, if this is not possible because three adjacent panels on the same direction are not available, then a simple forward/backward linear finite difference is used (the procedure is analogous to the one used for the centered quadratic fitting).

3.6.1 Pressure coefficient

It is possible to adimensionalize the pressure quantity $p - p_{ref}$, introducing a dimensionless pressure coefficient C_p defined as:

$$C_p = \frac{p - p_{ref}}{\frac{1}{2}\rho||V_{ref}||^2}. \quad (3.59)$$

From Bernoulli equation, Equation 3.59 can be rewritten in the following form

$$C_p = 1 - \frac{||\mathbf{V}_w - \mathbf{V}_b + \mathbf{v}_p||^2}{V_{ref}^2}. \quad (3.60)$$

Usually, a good choice for V_{ref} is the asymptotic velocity V_∞ . In the panel code, because Bernoulli equation is expressed in a body fixed frame of reference and because rotating bodies can be involved in the simulations, V_{ref} was chosen such as

$$V_{ref} = ||\mathbf{V}_w - \mathbf{V}_b||. \quad (3.61)$$

3.7 Iterative Kutta condition

The importance of the Kutta condition in the analytic formulation of the Laplace problem has already been discussed (Section 2.7). While in a two-dimensional steady case enforcing that the intensity of a near wake doublet panel is equal to the difference of the intensities of the two body doublets on the considered trailing edge (proposed by Joukowski, and here called the *regular/linear* Kutta condition) correspond to the condition of zero pressure jump on the trailing edge (proposed by Kutta), the same cannot be assumed a priori for the three-dimensional unsteady case [5]. In general this is not true for a zero order panel method. The non-zero pressure jump is particularly relevant in all those applications with strong velocity components parallel to the trailing edge (cross-flow), such as helicopter rotors or propeller blades. In Figure 3.17 is reported an example of pressure coefficient distribution for a NACA 0012 dual blade rotor. It is important to notice that the pressure jump does not converge to zero when the grid is refined, but is a pathological feature of low-order panel methods.

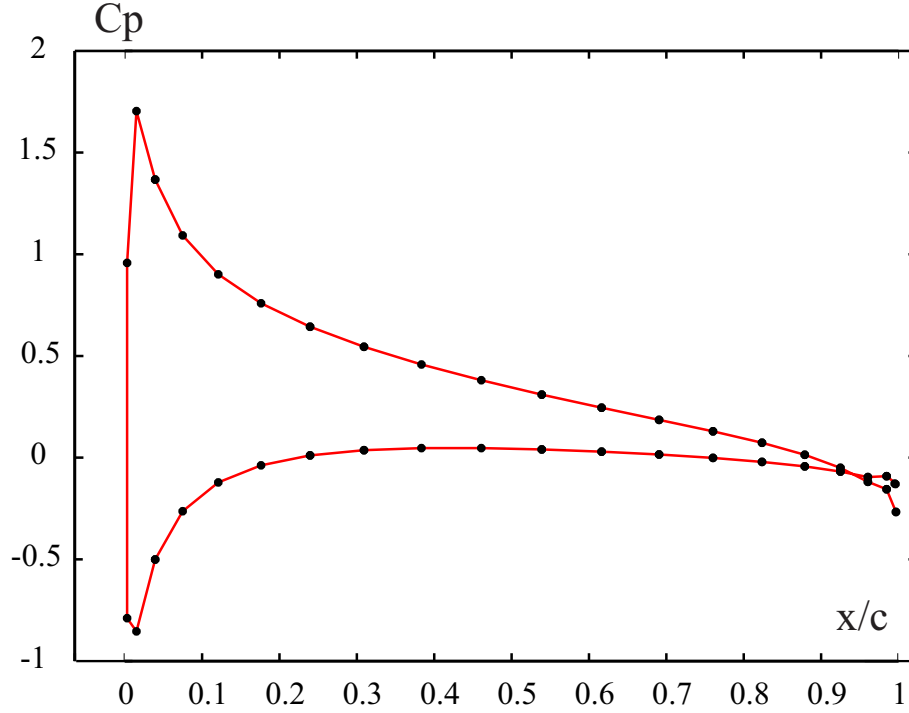


Figure 3.17: Chordwise distribution of C_p . At trailing edge, it is possible to notice that the pressure jump is not zero.

As the Equation 3.17 is not able to guarantee $\Delta C_p = 0$ on the trailing edge, a procedure to correct the near wake doublet intensities has to be introduced. This can be achieved using an iterative Newton-Rapson method. The aim of the iterative procedure is to obtain the strength of the near wake doublet in such a way that the pressure jump on the trailing edge is zero. The basis of the procedure are summarized in Figure 3.18.

In the first step of the procedure, the linear Kutta condition (see Equation 3.17) is applied, the linear system 3.10 is solved and the values of μ and $\tilde{\mu}$ are obtained. Using Bernoulli equation, the pressure coefficient C_p is obtained on the trailing edge panels and, from that, the pressure jump ΔC_p across the trailing edge is evaluated: in general, the pressure jump would not be zero. A variation of the near wake doublets intensity involves a variation of the pressure coefficient jump across the trailing edge:

$$\delta \{ \Delta C_p \} = \left[\frac{\Delta C_p}{\partial \tilde{\mu}} \right] \delta \{ \tilde{\mu} \}. \quad (3.62)$$

The analytical derivation of matrix $\left[\frac{\Delta C_p}{\partial \tilde{\mu}} \right]$ (also called *sensitivity matrix*) can be found in Appendix B. Indicating with k the k -th step of the iterative procedure and with $k + 1$ the

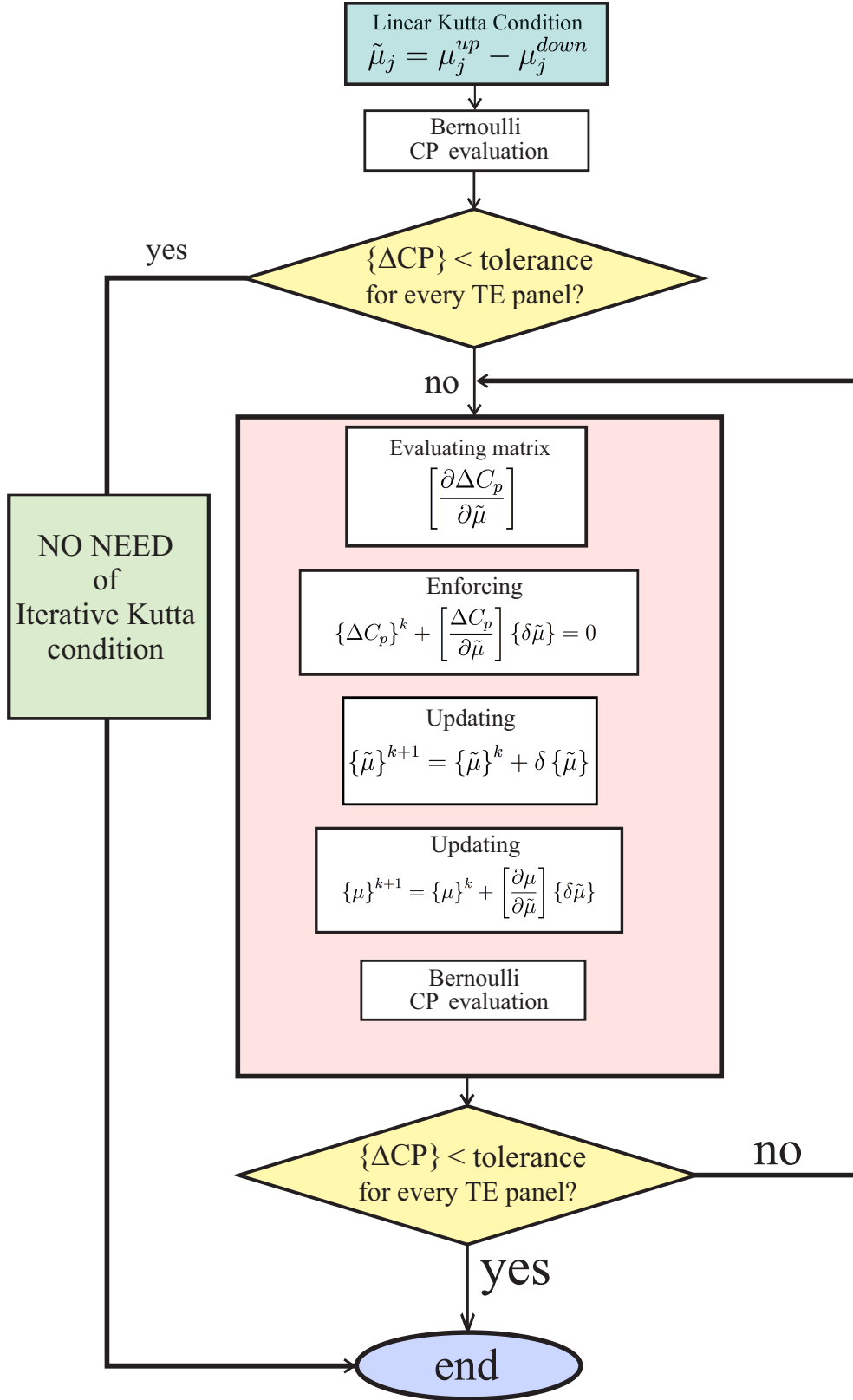


Figure 3.18: Iterative Kutta condition.

following one, it is possible to enforce ΔC_p to be zero on the trailing edge (assuming a linear dependence):

$$\{\Delta C_p\}^{k+1} = \{\Delta C_p\}^k + \delta \{\Delta C_p\} = \{\Delta C_p\}^k + \left[\frac{\Delta C_p}{\partial \tilde{\mu}} \right] \{\delta \tilde{\mu}\} = 0 \quad (3.63)$$

and consequently find the associated near wake doublet intensity:

$$\{\delta \tilde{\mu}\} = - \left[\frac{\partial \Delta C_p}{\partial \tilde{\mu}} \right]^{-1} \{\Delta C_p\}^k. \quad (3.64)$$

From Equation 3.64 it follows

$$\{\tilde{\mu}\}^{k+1} = \{\tilde{\mu}\}^k + \delta \{\tilde{\mu}\}. \quad (3.65)$$

It is now necessary to evaluate the body doublets intensities due to a variation of the near wake doublets. Starting from

$$[A] \{\mu\} + [C] \{\tilde{\mu}\} = -[B] \{\sigma\} - [D] \{\mu^*\}, \quad (3.66)$$

and differentiating in respect to $\{\mu\}$, the following expression is obtained:

$$\left[\frac{\partial \mu}{\partial \tilde{\mu}} \right] = -[A]^{-1} [C]. \quad (3.67)$$

Since

$$\{\tilde{\mu}\} = \left[\frac{\partial \mu}{\partial \tilde{\mu}} \right] \{\delta \tilde{\mu}\} \quad (3.68)$$

it holds that

$$\{\mu\}^{k+1} = \{\mu\}^k + \left[\frac{\partial \mu}{\partial \tilde{\mu}} \right] \{\delta \tilde{\mu}\} \quad (3.69)$$

and from Equation 3.67

$$\{\mu\}^{k+1} = \{\mu\}^k + [A] [C]^{-1} \{\delta \tilde{\mu}\} \quad (3.70)$$

It is important to notice that applying the iterative Kutta condition with the just introduced procedure does not change the nature of the problem: there is still one and only one solution of system 3.10.

From the new body doublets the new pressure coefficient jump on the trailing edge is evaluated, and the whole Newton iteration is repeated until the pressure jump is zero (or, in a numerical code, less than a tolerance parameter specified by the user). Figure 3.17 shows the same problem of Figure 3.17 when iterative Kutta condition is applied.

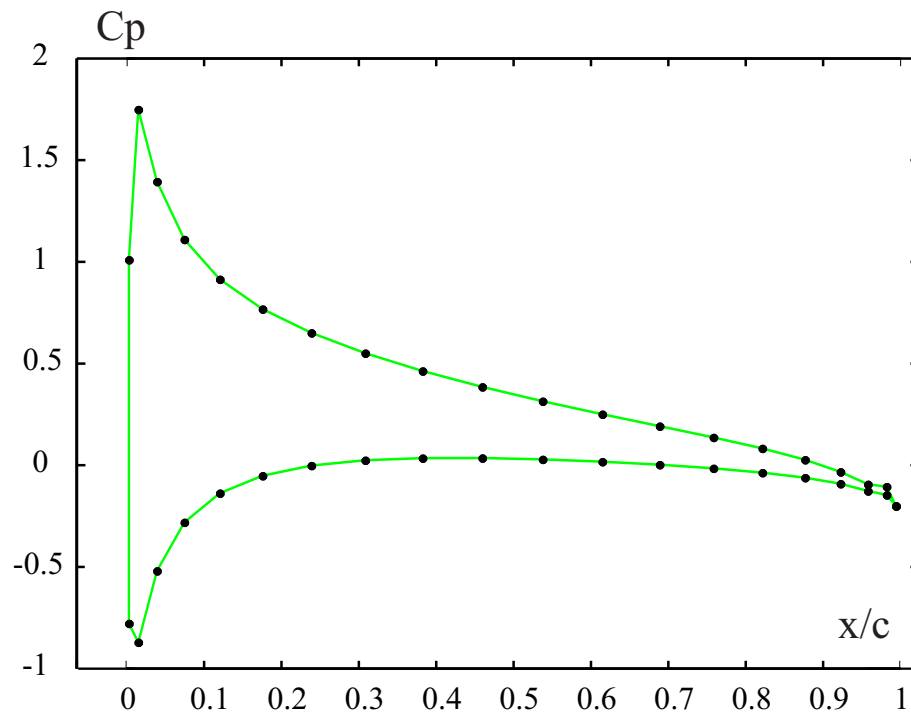


Figure 3.19: Chordwise distribution of C_p . At trailing edge the pressure jump has been driven to zero through the iterative Kutta condition.

Chapter 4

Body-Wake Interaction: Alternative Formulation

One of the major drawbacks of the BEM numerical formulation introduced so far is that instabilities arises every time a wake panel passes too close or impinges on another body panel, leading to inaccurate results. The nature of these instabilities is purely numerical and it is due to the fact that a doublet panel presents a singularity in its velocity potential induction. In the following sections different approaches to solve this problem will be presented and a new BEM numerical formulation based on velocity regularization of vortex rings will be introduced.

4.1 Body-wake impingement

Doublets and sources are elementary solutions of the Laplace equation and are the basis of numerical panel methods for the solution of potential flows. These solutions present a singularity and, in general, they have to be excluded from the flow domain. In an unsteady panel code it is possible that a wake comes close or sometimes even impinges on a body, leading to non-physical results due to numerical instabilities. These instabilities arise when a wake doublet comes too close to a collocation point: in fact, as the collocation point approaches the singularity, the influence coefficients of matrix D (see Equation 3.14) are subject to numerical errors.

To avoid these instabilities, a series of possible solutions found in literature are introduced. As the aim of a numerical code is to reproduce as close as possible the physical nature of a phenomenon, a natural solution to would be to enforce the no-penetration condition in such

a way that the wake does not impinge on the body while it is convected by the free stream. This approach has been adopted in [15] and involves a redistribution of the wake panels as they approach a body surface. Basically, before updating the wake position, a check on the wake panels is performed: if one or more panels are about to impinge on a body surface, they can be forced to slip over the surface eliminating the velocity component normal to the surface. If this is not possible without breaking the connectivity, the panels too close to the body are cut and remeshed in such a way they do not intersect the body surface. Despite the potentiality of this approach, the difficulties in implementing the panels cut-remesh procedure and some doubts concerning cases in which a body passes multiple times through a wake, represent some drawbacks that discouraged in choosing this formulation.

A different approach to remove the singularity is to simply set to zero the velocity potential induction when a collocation point is too close to the doublet panel or when the wake doublet impinges on the body. In this case the wake panels that can generate instabilities are excluded from the influence coefficients calculations. This can be an effective solution in all those cases in which the local effects of a wake passing close to a body are not relevant for the purposes of the experiment: in fact if the region of impingement is limited to a portion of the whole body, the global effects of the wake are well captured [29]. For all those cases in which the interaction between the wake and the body are important, like blade-vortex interaction in aeroacustics applications for helicopter rotors, this approach turns out to be inaccurate.

In Section 3.4.5 the equivalence between plane doublets and vortex rings has been presented, as well as the regularization of vortices induction with the introduction of the vortex core. This has proven to be extremely effective to remove numerical instabilities in the wake evolution and the same concept can be applied in the case of body-wake interaction. A new boundary element formulation has to be introduced. This formulation has been proposed in [13] and it was applied with excellent results in different applications, especially in the helicopteristic field. This solution turns out to be a good compromise between accuracy and versatility and will be adopted in this work. The analytical details of this approach are introduced in the following sections.

4.2 Alternative formulation

The basis of the method consists in decomposing the velocity potential in two contributions: an *incident potential* φ_I generated by the doublets of the far wake and a *scattered potential*

φ_S generated by the singularities over the body and near wake surfaces (doublet and sources for the body, doublets for the near wake). The total perturbation potential can be written as $\varphi = \varphi_I + \varphi_S$. Noticing that the velocity potential induced by the far wake does not depend on the velocity potential over the body or the near wake at the current timestep (Equation 2.37), recalling the results listed in Table 2.6 and employing the definition of incident potential, it is possible to write:

$$\varphi_I(\mathbf{x}, t) = - \int_{S_W^F} \Delta\varphi \frac{\partial G}{\partial n} d\mathcal{S}(\mathbf{y}). \quad (4.1)$$

For what concerns the scattered potential, applying a procedure similar to the one shown in Section 2.5, it holds:

$$\varphi_S(\mathbf{x}, t) = \int_{S_B} \left(G \frac{\partial \varphi}{\partial n} - \varphi \frac{\partial G}{\partial n} \right) d\mathcal{S}(\mathbf{x}) - \int_{S_W^N} \Delta\varphi \frac{\partial G}{\partial n} d\mathcal{S}(\mathbf{x}); \quad (4.2)$$

apparently both incident and scattered potential depend each one on the other and this dependence is represented by the total perturbation potential φ . Considering that the incident potential is continuous across the near wake, it holds:

$$\Delta\varphi(\mathbf{x}_W^{TE}, t) = \Delta\varphi_S(\mathbf{x}_W^{TE}, t) \quad (4.3)$$

where \mathbf{x}_W^{TE} is a generic wake point on trailing edge. Since the intensity of the potential along the wake does not change as it is convected downstream, from Equation 4.3 follows

$$\Delta\varphi(\mathbf{x}_W, t) = \Delta\varphi_S(\mathbf{x}_W^{TE}, t - \tau) \quad (4.4)$$

τ representing the time taken by a wake material point to move from the trailing edge position \mathbf{x}_W^{TE} to its current position \mathbf{x}_W . Finally, because the scattered potential is continuous across the far wake:

$$\Delta\varphi(\mathbf{x}_W, t) = \Delta\varphi_S(\mathbf{x}_W^{TE}, t - \tau) = \Delta\varphi_I(\mathbf{x}_W, t). \quad (4.5)$$

Equation 4.5 states that the formulation of the incident potential is related to the jump of scattered potential on trailing edge; Equation 4.1 can be rewritten as:

$$\varphi_I(\mathbf{x}, t) = - \int_{S_W^F} \Delta\varphi_I(\mathbf{x}_W, t) \frac{\partial G}{\partial n} d\mathcal{S}(\mathbf{y}) = - \int_{S_W^F} \Delta\varphi_S(\mathbf{x}_W^{TE}, t - \tau) \frac{\partial G}{\partial n} d\mathcal{S}(\mathbf{y}). \quad (4.6)$$

Following [13], writing a boundary integral equation only for the incident potential

$$\varphi_I(\mathbf{x}, t) = \int_{S_B} \left[G \frac{\partial \varphi_I}{\partial n} - \varphi_I \frac{\partial G}{\partial n} \right] d\mathcal{S}(\mathbf{y}) + \int_{S_I} \left[G \frac{\partial \varphi_I}{\partial n} - \varphi_I \frac{\partial G}{\partial n} \right] d\mathcal{S}(\mathbf{y}) \quad (4.7)$$

where \mathcal{S}_I is a closed surface surrounding the far wake \mathcal{S}_W^F . Then, letting \mathcal{S}_I approach \mathcal{S}_W^F , recalling that $\frac{\partial \varphi}{\partial n}$ (and $\frac{\partial \varphi_I}{\partial n}$) is continuous across the far wake, comparing Equations 4.1 and 4.7 leads to:

$$\int_{\mathcal{S}_B} \left(G \frac{\partial \varphi_I}{\partial n} - \varphi_I \frac{\partial G}{\partial n} \right) d\mathcal{S}(\mathbf{y}) = 0. \quad (4.8)$$

Finally, combining Equations 4.8 and 4.2, it holds that

$$\varphi_S(\mathbf{x}, t) = \int_{\mathcal{S}_B} \left(G \frac{\partial \varphi_S}{\partial n} - \varphi_S \frac{\partial G}{\partial n} \right) d\mathcal{S}(\mathbf{y}) - \int_{\mathcal{S}_W^N} \Delta \varphi_S \frac{\partial G}{\partial n} d\mathcal{S}(\mathbf{y}) \quad (4.9)$$

From the definition of scattered and incident potential follows

$$\frac{\partial \varphi_s}{\partial n} = \frac{\partial \varphi}{\partial n} - \frac{\partial \varphi_I}{\partial n} \quad (4.10)$$

and from the no-penetration condition expressed by Equation 2.17 and from the definition of $\mathbf{v}_I = \nabla \varphi_I$ as velocity induced by the incident potential, it is

$$\frac{\partial \varphi_s}{\partial n} = -\mathbf{V}_\infty \cdot \mathbf{n} - \mathbf{v}_I \cdot \mathbf{n}. \quad (4.11)$$

Enforcing that the scattered potential is zero inside the body (Dirichlet boundary condition), Equation 4.9 can be finally rewritten as

$$\begin{cases} \varphi_S(\mathbf{x}, t) = \int_{\mathcal{S}_B} (G \tilde{\sigma} - \varphi_S \frac{\partial G}{\partial n}) d\mathcal{S}(\mathbf{y}) - \int_{\mathcal{S}_W^N} \Delta \varphi_S \frac{\partial G}{\partial n} d\mathcal{S}(\mathbf{y}) \\ \tilde{\sigma} = -\mathbf{V}_\infty \cdot \mathbf{n} - \mathbf{v}_I \cdot \mathbf{n}. \end{cases} \quad (4.12)$$

From a comparison of Equations 4.12 and 2.55, it is clear that they are mathematically equivalent: thus, they can be solved with the same numerical formulation. The main difference is that the new formulation involves just the scattered potential; the evaluation of the incident potential is bypassed and the contribution of the far wake appears now in the boundary conditions, through the term \mathbf{v}_I and not as a direct contribution to the total perturbation potential. With this new formulation, in analogy with 2.51, because the scattered potential has been enforced to zero inside the body, the intensity of the body doublets will be

$$\mu = \varphi_s. \quad (4.13)$$

From the analogy between doublets and vortex rings, introducing a regularization function, \mathbf{v}_I remains bounded even when the collocation point is very close to the inducing panel, that means even when the wake impinges on the body surface.

It is important to remark that using Equation 4.12 the incident potential is not evaluated: for this reason, a different approach has to be adopted for the calculation of the forces on the body surface.

4.2.1 Pressures evaluation

To evaluate pressures on the body surface, Bernoulli theorem is used. Considering a point of the domain where the fluid properties are $p = p_{ref}$ and $\mathbf{V} = \mathbf{V}_{ref}$ and decomposing the total perturbation potential in the contributions of scattered and incident potential, using relations

$$\begin{cases} \varphi_s = \mu \\ \nabla\varphi_I = \mathbf{v}_I \end{cases} \quad (4.14)$$

from Equation 2.12 specified in a body fixed frame of reference, for a generic point on the body surface it holds

$$\frac{\partial\varphi_s}{\partial t} + \frac{\partial\varphi_I}{\partial t} + \frac{||\mathbf{V}_w - \mathbf{V}_b + \nabla\varphi_s + \mathbf{v}_I||^2}{2} + \frac{p}{\rho} = \frac{p_{ref}}{\rho} + \frac{||\mathbf{V}_{ref}||^2}{2}. \quad (4.15)$$

where \mathbf{V}_b represents the velocity of the moving body and \mathbf{V}_w is the wind velocity. All terms in Equation 4.15 are known from the solution of Equation 4.12, except the time derivative $\frac{\partial\varphi_I}{\partial t}$.

To evaluate $\frac{\partial\varphi_I}{\partial t}$ a complete procedure can be found in [6]; just a brief outline will be here reported. From the definition of incident potential, the time derivative in a body fixed frame of reference can be written as

$$\frac{\partial\varphi_I}{\partial t}(\mathbf{x}, t) = -\frac{\partial}{\partial t} \int_{S_W^F} \Delta\varphi_s(\mathbf{y}^{TE}, t - \tau) \frac{\partial G}{\partial n} dS(\mathbf{y}) \quad (4.16)$$

where \mathbf{y}^{TE} is the point on the trailing edge corresponding to the point \mathbf{y} on the far wake considered for the integration.

Basically, the integral is rewritten in a new frame of reference defined on the wake by the introduction of two curvilinear material coordinates (ζ_1, ζ_2) . ζ_1 is a time coordinate: it sets the position of a wake point based on the time instant this point was on trailing edge, while ζ_2 is defined along the trailing edge direction.

In this new coordinate system the integral is decomposed in three contributions:

- a contribution from the fact that the potential induction changes due to the fact that the distance between a body collocation point and a far wake point changes because of the relative motion between the two;
- a contribution from the wake deformation (this can usually be neglected if compared to the first term);

- a contribution from the flux of wake points that at every time instant cross the separation line between far wake and near wake.

The first contribution involves the evaluation of \boldsymbol{v}_I : using a regularization function guarantees the velocity, as well as the pressure on the body, remain bounded (no numerical instabilities arise).

Chapter 5

Kinematics

One of the advanced capabilities of the code is the possibility to accept in input different bodies, each one moving independently from the others in a three dimensional space. This is accomplished introducing multiple coordinate systems, each one linked to a *function table* that contains position, orientation and velocities of that coordinate system with respect to another one. In the next sections, the theory and the tools necessary to the development of the advanced kinematics of the aerodynamic solver will be presented.

5.1 Coordinate systems

To define the position of a point in a multi-dimensional space, a coordinate system is needed. Considering the three dimensional Euclidean space, all the coordinate systems present in the aerodynamic solver are three dimensional right-handed Cartesian coordinate systems, as shown in Figure 5.1. A three dimensional rigid object moving in a three dimensional space has six degrees of freedom: to determine position and orientation of the body respect to a coordinate system, six independent parameters are necessary. Imagining a coordinate system \mathcal{B} attached to the rigid body, the problem of describing the motion of the body respect to a generic coordinate system \mathcal{A} means determining six independent parameters that describe position and orientation of coordinate system \mathcal{B} with respect to coordinate system \mathcal{A} . The first three parameters are the coordinates the origin $O_{\mathcal{B}}$ of system \mathcal{B} , expressed in coordinates of system \mathcal{A} : this will be indicated by using the notation $O_{\mathcal{A}}O_{\mathcal{B}}^{\mathcal{A}}$, where the letter of the subscript indicates the coordinate system to which point O is attached, and the superscript indicates the coordinate system to which the coordinates of $O_{\mathcal{B}}$ are expressed.

To determine the orientation of \mathcal{B} with respect to \mathcal{A} , three other parameters are neces-

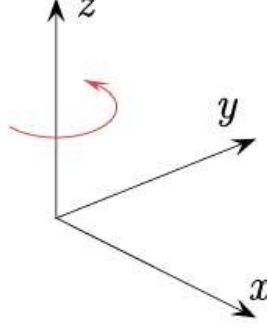


Figure 5.1: Right-handed Cartesian coordinate system. The vector product follows the so-called right-hand rule, as shown for a positive rotation around axis z .

sary: in the next section, *Euler angles* will be introduced.

5.1.1 Euler angles

A way to determine the orientation of a coordinate system \mathcal{B} with respect to a coordinate system \mathcal{A} is to use *Euler angles*. Euler angles are three parameters that represent a series of three sequential elemental rotations (rotation about three Cartesian axis) necessary to bring system \mathcal{B} to coincide with system \mathcal{A} . Given two generic frames of reference \mathcal{A} and \mathcal{B} , twelve different combination of elemental rotations are possible to bring \mathcal{B} to coincide with \mathcal{A} , so twelve different possible definitions of Euler angle exist [31]. Figure 5.2 shows the convention used in this work: this particular choice of angles is often used in aeronautics and aerospace applications and it is usually indicated with the name of *Tait-Bryan angles*.

System \mathcal{B} is obtained from system \mathcal{A} after three sequential rotations ψ , θ and ϕ and conversely system \mathcal{A} is obtained from system \mathcal{B} after three rotations $-\phi$, $-\theta$ and $-\psi$. Combining three elemental matrix rotations (see Appendix C.1), the final expression of the rotation matrix from \mathcal{B} to \mathcal{A} is

$$[\Omega_{rot}^{\mathcal{B} \rightarrow \mathcal{A}}] = \begin{bmatrix} \cos \theta \cos \psi & \sin \phi \sin \theta \cos \psi - \cos \phi \sin \psi & \cos \phi \sin \theta \cos \psi + \sin \phi \sin \psi \\ \cos \theta \sin \psi & \sin \theta + \cos \psi & \sin \theta - \sin \phi \cos \psi \\ -\sin \theta & \sin \phi \cos \theta & \cos \phi \cos \theta \end{bmatrix}. \quad (5.1)$$

It is easy to prove that the inverse matrix determines the rotation from \mathcal{A} to \mathcal{B} . Moreover, due to the orthogonality of the rotation matrix, the inverse coincides with the transpose matrix:

$$[\Omega_{rot}^{\mathcal{A} \rightarrow \mathcal{B}}] = [\Omega_{rot}^{\mathcal{B} \rightarrow \mathcal{A}}]^{-1} = [\Omega_{rot}^{\mathcal{B} \rightarrow \mathcal{A}}]^T \quad (5.2)$$

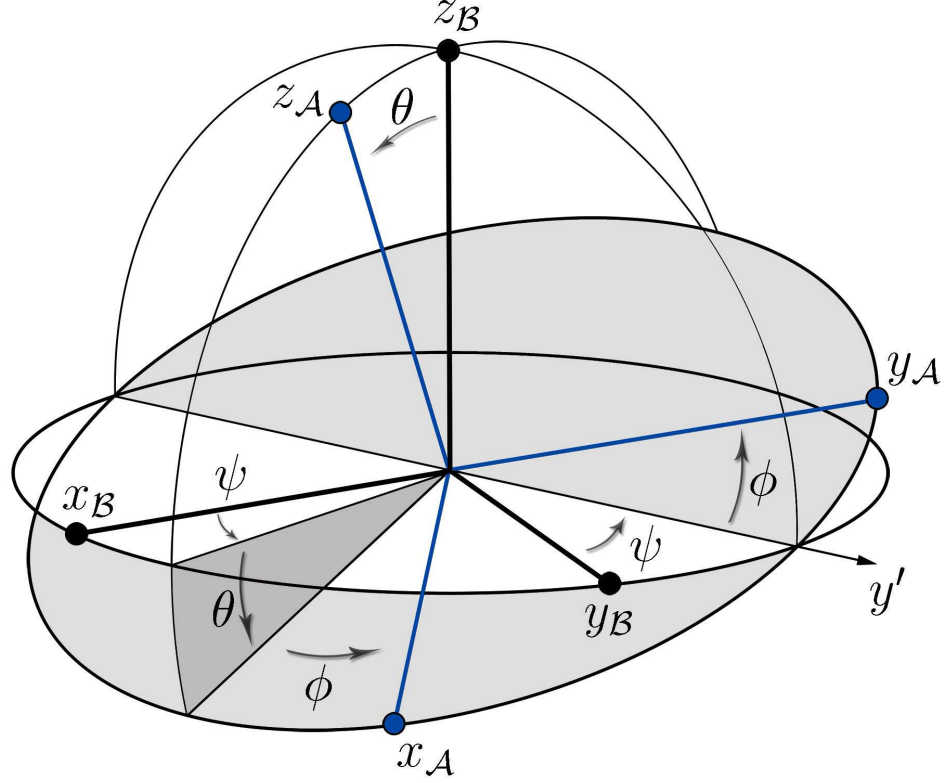


Figure 5.2: Euler angles: system \mathcal{B} is brought to coincide with system \mathcal{A} by three consecutive rotations about intermediate axis. In figure is shown a particular choice of Euler angles called Tait-Bryan angles.

where the symbol T indicates the transpose matrix.

5.1.2 Coordinate transformation

The core of the kinematic module is represented by the coordinate transformations between the different frames of reference. Once the six parameters that define the position and the orientation of a frame of reference with respect to another are known, it is possible to write the analytical expression of the coordinate transformation between the two systems. Indicating with $\mathbf{O}_{\mathcal{A}}\mathbf{P}$ the coordinates of a generic point P expressed in a frame of reference \mathcal{A} and with $\mathbf{O}_{\mathcal{B}}\mathbf{P}$ the coordinates of the same point expressed in a frame of reference \mathcal{B} , it is

$$\mathbf{O}_{\mathcal{A}}\mathbf{P} = \mathbf{O}_{\mathcal{A}}\mathbf{O}_{\mathcal{B}} + \Omega_{rot}^{\mathcal{B} \rightarrow \mathcal{A}} \mathbf{O}_{\mathcal{B}}\mathbf{P}. \quad (5.3)$$

Similarly, the transformation of the coordinates of a point P from system \mathcal{A} to system \mathcal{B} is

$$\mathbf{O}_B \mathbf{P} = \mathbf{O}_B \mathbf{O}_A + \Omega_{rot}^{A \rightarrow B} \mathbf{O}_A \mathbf{P}. \quad (5.4)$$

where $\Omega_{rot}^{B \rightarrow A}$ is obtained from Equation 5.2. Looking at Equations 5.3 and 5.4, a coordinate transformation between two generic frames of reference \mathcal{A} and \mathcal{B} (e.g. from \mathcal{B} to \mathcal{A}) is an operator characterized by two elements:

- a translational part $\mathbf{tr}^{B \rightarrow A}$, represented by the vector of the coordinates of the origin of system \mathcal{B} , expressed in the coordinates of \mathcal{A} (i.e. $\mathbf{O}_A \mathbf{O}_B$ in Equation 5.3)
- a rotational part, indicated by the matrix $ROT^{B \rightarrow A}$, obtained from the definition of Euler angles (e.g. $\Omega_{rot}^{B \rightarrow A}$ in Equation 5.3).

It is possible to show (see Appendix C.2), that if the transformation between a frame of reference \mathcal{A} and a frame of reference \mathcal{B} and the transformation between \mathcal{A} and a third coordinate system \mathcal{C} are known, then the transformation between \mathcal{B} and \mathcal{C} is immediately defined.

5.2 Bodies motion

In the previous sections, the problem of transforming the coordinates of a point from a frame of reference to another has been analyzed. This is a fundamental step necessary to *efficiently* describe the generic motion of a rigid body in a three dimensional space. Imagine a rigid body moving in respect to a generic frame of reference \mathcal{A} , and a frame of reference \mathcal{B} attached to the body.

Determining the motion of the body with respect to \mathcal{A} means evaluating the position of the points of the body in that frame of reference at every time t : this is achieved using only the information available at the previous time, making the time-marching scheme fully explicit.

The linear velocity of the origin of system \mathcal{B} is indicated with $\mathbf{v}_{O_B}^A$ and the angular velocity with respect to the frame \mathcal{A} with $\boldsymbol{\omega}_{B \rightarrow A}^A = (p_{B \rightarrow A}^A, q_{B \rightarrow A}^A, r_{B \rightarrow A}^A)$. The initial conditions are the position of the origin $\mathbf{x}_{O_B}^A$ and the orientation of the frame \mathcal{B} with respect to \mathcal{A} , expressed by the Euler angles. To obtain the coordinates $\mathbf{O}_A \mathbf{O}_B^A$ at the generic time t_1 , the velocity components of $\mathbf{v}_{O_B}^A$ can be directly integrated, using $\mathbf{x}_{O_B}^A(t_0)$ as initial conditions.

$$\mathbf{O}_A \mathbf{O}_B^A(t_1) = \mathbf{O}_A \mathbf{O}_B^A(t_0) + \int_{t_0}^{t_1} \mathbf{v}_{O_B}^A(t) dt. \quad (5.5)$$

For the angular velocity, things are slightly different: it is not possible to integrate directly the velocity components p, q, r , but it is necessary to convert them into Euler angles derivatives. The conversion matrix $\Omega_{\mathcal{A} \rightarrow EA}$ and its inverse $\Omega_{EA \rightarrow \mathcal{A}}$ are obtained in Appendix C.3. The main problem of this method is that matrix $\Omega_{EA \rightarrow \mathcal{A}}$ becomes singular when $\theta \rightarrow 0$. This is known as *gimbal lock*: two of the rotational axes merge together, causing the loss of one degree of freedom [31]. To circumvent this problem it is necessary to bypass the use of matrix $\Omega_{EA \rightarrow \mathcal{A}}$: this will be achieved introducing *quaternions*.

5.3 Quaternions

A *quaternion* \hat{q} is a mathematical element formed by a scalar part q_0 and a vector part $\mathbf{q} = q_1 \mathbf{i} + q_2 \mathbf{j} + q_3 \mathbf{k}$:

$$\mathbb{H} = \{ \hat{q} = q_0 + \mathbf{q}, \quad q_0 \in \mathbb{R}, \quad \mathbf{q} \in \mathbb{R}^3 \}. \quad (5.6)$$

The concept of quaternions [33] was introduced by the mathematician W. Hamilton and it was based on the idea of the extension to four dimensions of the complex Euler plane: the bases of the vector part $\mathbf{i}, \mathbf{j}, \mathbf{k}$ can be seen as three imaginary axis of a complex space. Consequently, the following relations apply:

- $\mathbf{i}^2 = \mathbf{j}^2 = \mathbf{k}^2 = -1$
- $\mathbf{i}\mathbf{j} = \mathbf{k}$, $\mathbf{j}\mathbf{k} = \mathbf{i}$, $\mathbf{k}\mathbf{i} = \mathbf{j}$.

For any quaternion $\hat{q}, \hat{p} \in \mathbb{H}$ and any scalar number $\lambda \in \mathbb{R}$, three elementary operations are defined:

- addition

$$\begin{aligned} (+) : \mathbb{H} \times \mathbb{H} &\rightarrow \mathbb{H} \\ \hat{q} + \hat{p} &= (q_0 + p_0) + (\mathbf{q} + \mathbf{p}) \end{aligned} \quad (5.7)$$

- scalar multiplication

$$\begin{aligned} () : \mathbb{R} \times \mathbb{H} &\rightarrow \mathbb{H} \\ \lambda \hat{q} &= \lambda q_0 + \lambda \mathbf{q} \end{aligned} \quad (5.8)$$

- quaternion multiplication

$$\begin{aligned} (\circ) : \mathbb{H} \times \mathbb{H} &\rightarrow \mathbb{H} \\ \hat{q} \circ \hat{p} &= (q_0 p_0 - \mathbf{q} \cdot \mathbf{p}) + (p_0 \mathbf{q} + q_0 \mathbf{p} + \mathbf{q} \wedge \mathbf{p}). \end{aligned} \quad (5.9)$$

As the multiplication of two quaternions is a quaternion, mathematically the set of the quaternions is a *group* and, following the definition of addition and scalar multiplication, it is also a *four-dimensional linear space* over \mathbb{R} . It should be noted that the vector product $\mathbf{q} \wedge \mathbf{p}$ makes the multiplication between quaternions *non-commutative*.

It is now possible to introduce a series of useful definitions:

- conjugated quaternion

$$\widehat{q}^* = q_0 - \mathbf{q} \quad (5.10)$$

It is easy to prove that, being \widehat{q} and \widehat{p} two quaternions, it is

$$(\widehat{q} \circ \widehat{p})^* = \widehat{p}^* \circ \widehat{q}^* \quad (5.11)$$

- quaternion norm (or quaternion length)

$$\|\widehat{q}\| = \sqrt{\widehat{q} \circ \widehat{q}^*} = \sqrt{q_0^2 + \mathbf{q}^2} = \sqrt{q_0^2 + q_1^2 + q_2^2 + q_3^2} \quad (5.12)$$

A quaternion with unit norm is called *unit quaternion*.

- inverse of a quaternion with non-zero norm

$$\widehat{q}^{-1} = \frac{q^*}{\|\mathbf{q}\|^2} \quad (5.13)$$

such as $\widehat{q} \circ \widehat{q}^{-1} = 1$. It is immediate that for a unit quaternion $\widehat{q}^{-1} = \widehat{q}^*$.

- pure quaternion

A quaternion with a zero scalar part: $\widehat{q} = 0 + \mathbf{q}$. It is easy to show that pure quaternions are a three-dimensional linear subspace of \mathbb{H} . For a pure quaternion $\widehat{q}^* = -\widehat{q}$.

- polar form

A quaternion \widehat{q} can be written in polar form

$$\widehat{q} = \|\widehat{q}\| (\cos \theta + \mathbf{n} \sin \theta) \quad (5.14)$$

where $\cos \theta = \frac{q_0}{\|\widehat{q}\|}$, $\sin \theta = \frac{\sqrt{q_1^2 + q_2^2 + q_3^2}}{\|\widehat{q}\|}$ and $\mathbf{n} = \frac{\mathbf{q}}{\|\widehat{q}\|}$.

By definition, \mathbf{n} is a unit vector.

Once introduced the main properties and the operators between quaternions, it is possible to show that there is a relation between quaternions product and three dimensional rotations. Consider a generic quaternion $\widehat{p} = (p_0, \mathbf{p})$ and a unit quaternion $\widehat{q} = (q_0, \mathbf{q})$. Since quaternions multiplications are non-commutative, two linear operators can be introduced:

- left multiplication for a unit quaternion \hat{q}

$$\phi_{\hat{q}}^L(\hat{p}) = \hat{q} \circ \hat{p} \quad (5.15)$$

- right multiplication for a unit quaternion \hat{q}

$$\phi_{\hat{q}}^R(\hat{p}) = \hat{p} \circ \hat{q}. \quad (5.16)$$

Both operations represent rotations in a four dimensional space and the length of quaternion p is preserved [31]; according to polar form 5.14, the rotation axis is vector \mathbf{n} associated to quaternion \hat{q} and the rotation angle is $\frac{\theta}{2}$. In the present work, the choice of quaternions was adopted to perform rotations on three dimensional vectors without incurring in the singularity problems shown by the use of the Euler rotation matrix. Considering a three dimensional vector as a pure quaternion, it is possible to perform a rotation using the linear operators 5.15 and 5.3: unfortunately, the result of such operation is not a pure quaternion, because the operations introduced do not map pure quaternions into pure quaternions. To perform the rotation of a vector, it can be transformed into a pure quaternion and then rotated through a quaternion product: from the result of the product, the rotated vector can be extracted only if the result is a pure quaternion. A new linear operator that maps pure quaternions into pure quaternions has to be introduced, combining two sequential rotations:

$$\mathcal{R}^{\hat{q}}(\hat{p}) = \phi_{\hat{q}}^{R*}(\hat{p}) \phi_{\hat{q}}^L(\hat{p}) = \hat{q}^* \circ \hat{p} \circ \hat{q}. \quad (5.17)$$

According to Euler's Theorem on Rotations, that states that every change in orientation of two coordinate systems (or two rigid bodies) can always be obtained as an elemental rotation about a single axis, the product of any two simple rotations is another rotation, and 5.17 is a rotation that maps pure quaternions in pure quaternions [31]. As \hat{q}^* and \hat{q} have the same direction of axis \mathbf{n} , the two consequential rotation are performed around the same axis and the rotation angle of the composed rotation is $\frac{\theta}{2} + \frac{\theta}{2} = \theta$. Consequently, the final rotation does not depend on the order in which the two simple rotations are performed.

5.3.1 Equivalence between quaternions and Euler angles

As already seen, defining the orientation of a coordinate system \mathcal{B} with respect to a coordinate system \mathcal{A} through Euler angles, means finding the values of three angles that defines three

precise rotations that bring \mathcal{A} to coincide with \mathcal{B} . Another way to see Euler's Theorem, cited in the previous section, is that it is possible to get from one orientation to another by a simply steady rotation about a single axis. This can be expressed with a single quaternion rotation, while with Euler angles the final result was obtained by three consequential rotations. It is possible to show (see Appendix C.7) that, given a quaternion representing a certain rotation, the equivalent matrix rotation [14] is

$$[\Omega_{rot}^{\mathcal{B} \rightarrow \mathcal{A}}] = \begin{bmatrix} q_0^2 + q_1^2 - q_2^2 - q_3^2 & 2(q_1q_2 - q_0q_3) & 2(q_1q_3 + q_0q_2) \\ 2(q_1q_2 + q_0q_3) & q_0^2 - q_1^2 + q_2^2 - q_3^2 & 2(q_2q_3 - q_0q_1) \\ 2(q_1q_3 - q_0q_2) & 2(q_2q_3 + q_0q_1) & q_0^2 - q_1^2 - q_2^2 + q_3^2 \end{bmatrix}. \quad (5.18)$$

5.3.2 Determining the attitude of a frame of reference in motion

As already discussed, a quaternion is a mathematical element that can be used to express a rotation of a certain angle around a given axis and, for this reason, quaternions can substitute Euler angles to represent the attitude of a certain coordinate system with respect to another. As introduced in Section 5.2, given the angular velocity $\boldsymbol{\omega}$ and the attitude of a certain frame of reference with respect to another at time t_0 , the main problem is to find the new attitude at time t_1 . Because of the singularity of the rotation matrix that converts p, q, r into ϕ, θ, ψ , another formulation based on the use of quaternions is presented. Considering two different coordinate systems \mathcal{A} and \mathcal{B} and a vector \mathbf{x}_P attached to \mathcal{A} , it is possible to write the following relation (see Appendix C.5):

$$\frac{\partial \mathbf{x}_P^{\mathcal{B}}}{\partial t} = \boldsymbol{\omega}_{\mathcal{A} \rightarrow \mathcal{B}}^{\mathcal{B}} \times \mathbf{x}_P^{\mathcal{B}} \quad (5.19)$$

where $\mathbf{x}_P^{\mathcal{A}}$ is the vector \mathbf{x}_P expressed in coordinates of system \mathcal{A} , $\mathbf{x}_P^{\mathcal{B}}$ is the same vector expressed in coordinates of \mathcal{B} and $\boldsymbol{\omega}_{\mathcal{A} \rightarrow \mathcal{B}}^{\mathcal{B}}$ is the angular velocity of \mathcal{A} with respect to \mathcal{B} , expressed in coordinates of \mathcal{A} . Similarly, using quaternions, it is (see Appendix C.6):

$$\frac{\partial}{\partial t} \begin{Bmatrix} 0 \\ \mathbf{x}_P^{\mathcal{B}} \end{Bmatrix} = 2 \frac{\partial \hat{q}}{\partial t} \circ \hat{q}^* \circ \begin{Bmatrix} 0 \\ \mathbf{x}_P^{\mathcal{B}} \end{Bmatrix}. \quad (5.20)$$

Comparing equations 5.19 and 5.20 and remembering that $2 \frac{\partial \hat{q}}{\partial t}$ is a pure quaternion, it is possible to write

$$\begin{Bmatrix} 0 \\ \boldsymbol{\omega}_{\mathcal{A} \rightarrow \mathcal{B}}^{\mathcal{B}} \end{Bmatrix} = 2 \frac{d\hat{q}}{dt} \circ \hat{q}^* \quad (5.21)$$

and consequently

$$\frac{d\hat{q}}{dt} = \frac{1}{2} \left(\left\{ \begin{array}{c} 0 \\ \boldsymbol{\omega}_{\mathcal{A} \rightarrow \mathcal{B}}^{\mathcal{B}} \end{array} \right\} \circ \hat{q} \right). \quad (5.22)$$

Equation 5.22 is a fundamental result: it can be integrated in time to obtain the quaternion defining the attitude of a reference system with respect to another.

5.4 Practical implementation

The mathematical expressions to find the position and the attitude in time of a coordinate system respect to another has been introduced in the previous sections. Indicating with T a certain timestep and with $T + \Delta T$ the following one, Equation 5.5 can be rewritten as

$$\mathbf{O}_{\mathcal{A}}\mathbf{O}_{\mathcal{B}}^{\mathcal{A}}(T + \Delta T) = \mathbf{O}_{\mathcal{A}}\mathbf{O}_{\mathcal{B}}^{\mathcal{A}}(T) + \int_T^{T+\Delta T} \mathbf{v}_{\mathbf{O}_{\mathcal{B}}}^{\mathcal{A}}(t) dt \quad (5.23)$$

and Equation 5.22 becomes

$$\hat{q}(T + \Delta T) = \hat{q}(T) + \frac{1}{2} \int_T^{T+\Delta T} \left(\left\{ \begin{array}{c} 0 \\ \boldsymbol{\omega}_{\mathcal{A} \rightarrow \mathcal{B}}^{\mathcal{B}} \end{array} \right\} \circ \hat{q} \right) dt. \quad (5.24)$$

The integration of Equations 5.23 and 5.24 is carried out using a Fourth-Order Runge Kutta scheme (see Appendix C.4). The position and attitude at timestep T are known from integration of the previous timesteps, or they are assigned as inputs at the beginning of the motion ($T=0$).

In Figure 5.3 the numerical procedure introduced in this section is summarized.

5.5 Recapitulatory table

In Figure 5.4 a summary of the kinematic module is represented. In the pre-processing the geometry, the translational and angular velocities of all the coordinate systems present in the simulation and the initial position and attitude are imported. The velocities and the positions are stored in the *function tables*. During the time-stepping, the new values of the velocities are read and stored in the function tables. Through the Runge-Kutta integration, the new position and attitude of each coordinate system are obtained. Once the mutual orientations between coordinate systems are known, it is possible to obtain all the transformations between coordinate systems; as already seen, these are made of a

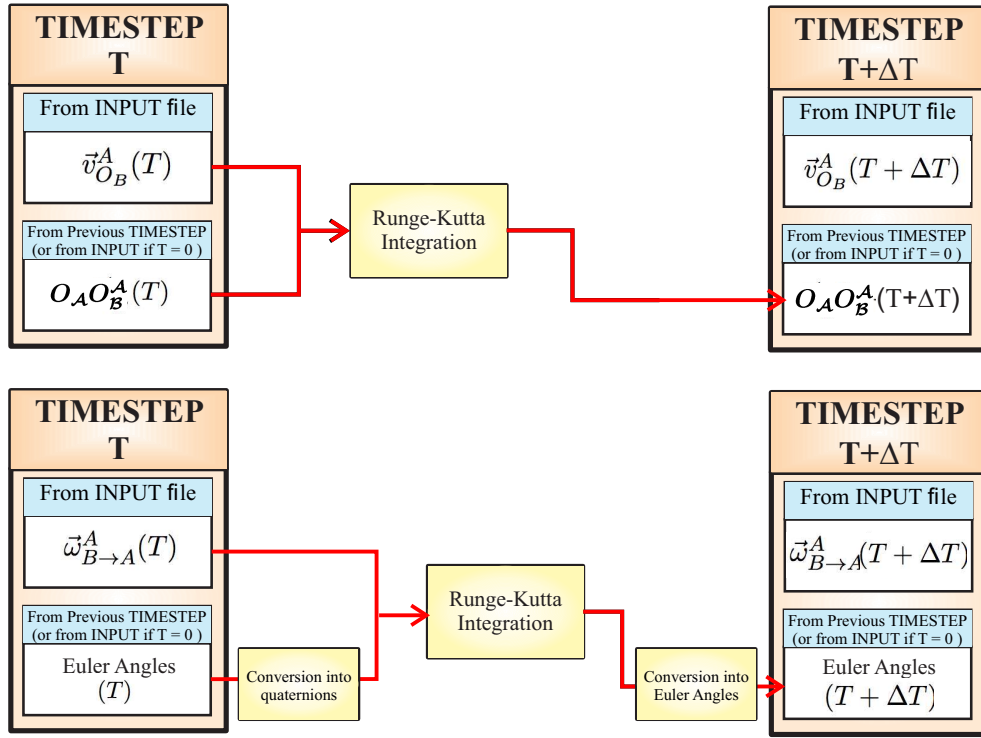


Figure 5.3: Procedure to obtain the coordinate system position and attitude at a certain timestep $T + \Delta T$, using the information from the previous timestep T .

translational (vector) and a rotational (matrix) part. Two types of transformations are obtained: one for the position vectors, another one for the velocities. At the beginning of each timestep the function tables are updated and the procedure is repeated.

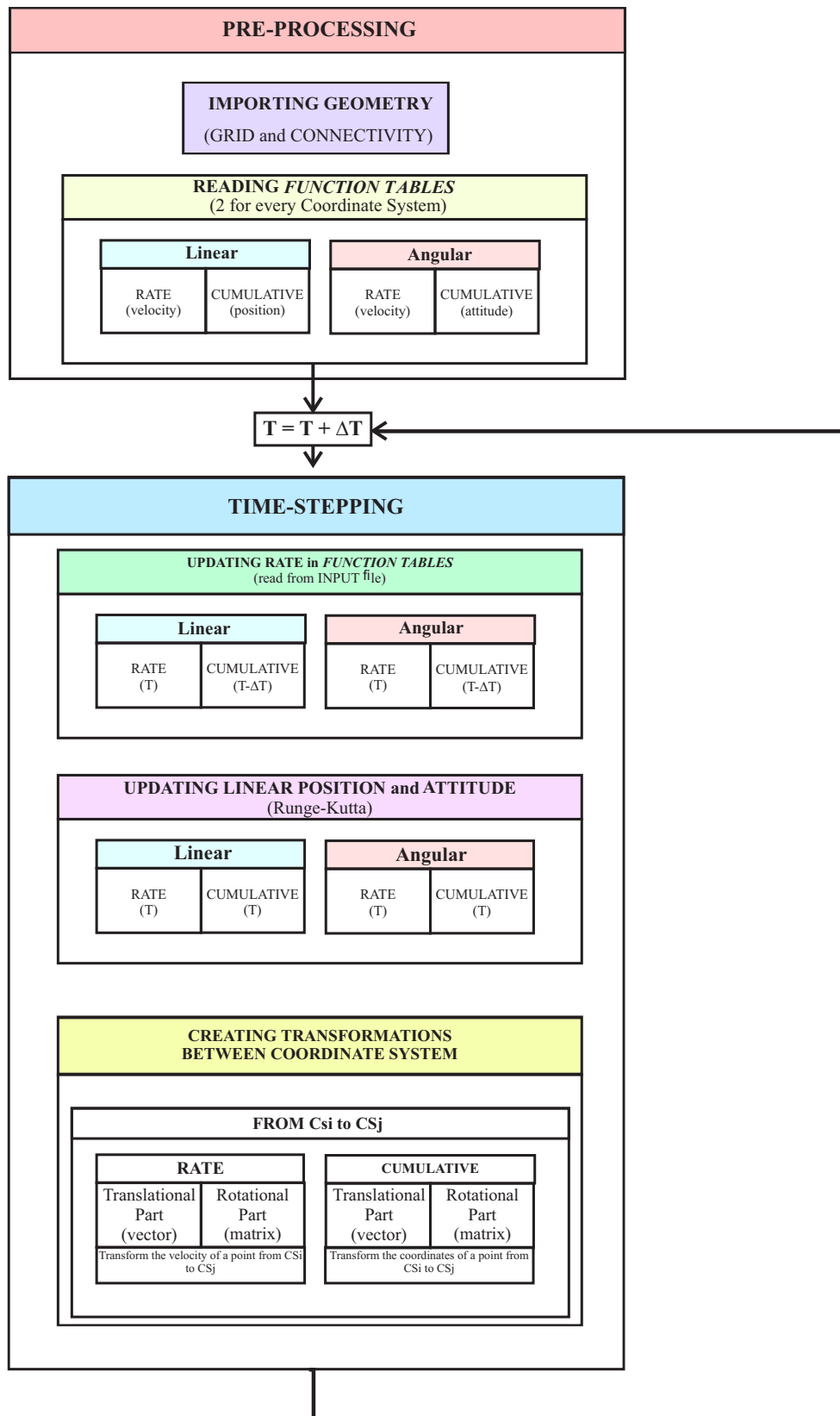


Figure 5.4: Kinematic module: recapitulatory table.

Chapter 6

Code Improvements

The analytical theory and the numerical implementation of the main features of the present panel code have been introduced in the previous chapters. Here a series of additional features will be introduced.

To improve code efficiency, in all those cases in which the geometry, the motion of the bodies involved in the simulation, and the flow conditions are symmetrical in respect to a reference plane, it is possible to reduce the dimension of the aerodynamic coefficient matrices and reduce the computational cost. The outlines of the implementation will be presented in the following.

Although one of the main features of the present code is the possibility to model three-dimensional bodies with thickness, sometimes, especially for those simulations involving a high number of panels, it could be convenient to neglect the thickness of a body. A body can be modeled representing only its mean surface, reducing the number of panels approximatively by a factor of two.

6.1 Symmetry

6.1.1 Perturbation potential induction

A symmetric problem implies a symmetry in the potential inductions between panels and, consequently, a symmetry in the aerodynamic coefficient matrices. Taking into account this symmetry reduces the computational efforts. For example, if only one plane of symmetry is identified, the dimensions of the matrices reduces from $2n \times 2n$ to $n \times n$, where $2n$ is the order of the generic aerodynamic matrix in case no symmetry is involved. In addition,

symmetry reduces the inaccuracies due to numerical errors.

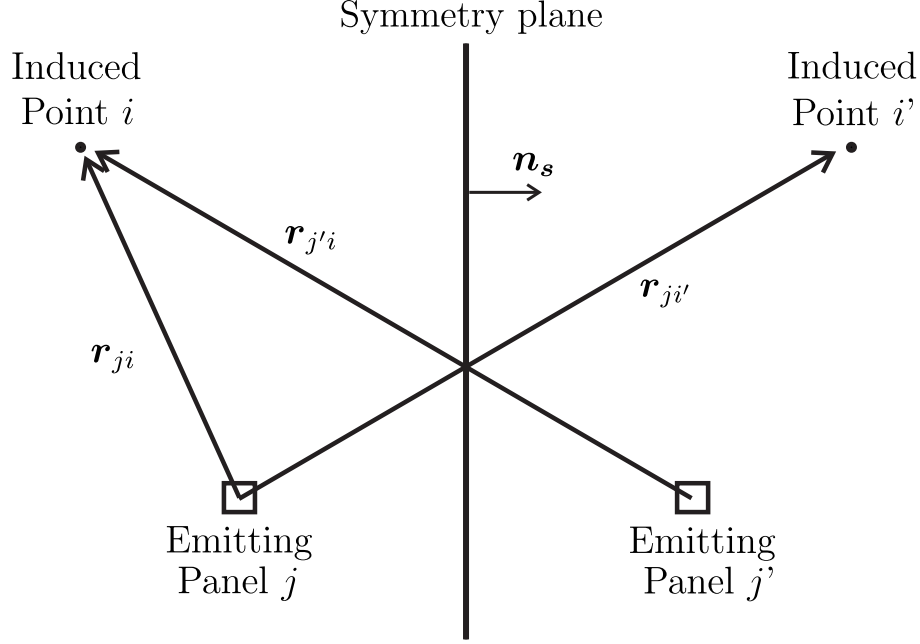


Figure 6.1: Representation of the case of an inducing panel and an induced point and their respective symmetric counterparts, focusing on the potential induction.

Figure 6.1 represents a generic inducing panel (doublet or source) j and its symmetrical j' respect to a generic symmetry plane, and a receiving point i and its symmetrical i' respect to the same plane. It can be observed that the perturbation potential φ_i at point i is given from both the contributions of panel j and j' . Indicating with φ_{ji} the perturbation potential induce by j at i and with $\varphi_{j'i}$ the potential induced by j' at i , it is

$$\varphi_i = \varphi_{ji} + \varphi_{j'i}. \quad (6.1)$$

From the first set of equations of System 3.19, indicating with ***RHS*** the right hand side, it is possible to notice that for a symmetric configuration the patterns shown in Figure 6.2 are obtained: the blocks with same colors in matrix \tilde{A} and in vectors $\boldsymbol{\mu}$ and ***RHS*** are equal. The symmetry in matrix \tilde{A} can be justified observing Figure 6.1 and recalling the definitions of aerodynamic influence coefficients from Section 3.3, while the symmetry in vector $\boldsymbol{\mu}$ comes from the symmetry conditions of the problem. Basically the equivalences depicted in Figure 6.2 state that the potential induced by panel j' at point i is the same as the one induced by panel j at point i' . Same deductions done for matrix \tilde{A} can be extended to the ***RHS***

$$\begin{pmatrix} \tilde{A}_{11} & \tilde{A}_{12} & \dots & \tilde{A}_{1N} & \tilde{A}_{11'} & \tilde{A}_{12'} & \dots & \tilde{A}_{1N'} \\ \tilde{A}_{21} & \tilde{A}_{22} & \dots & \tilde{A}_{2N} & \tilde{A}_{21'} & \tilde{A}_{22'} & \dots & \tilde{A}_{2N'} \\ \dots & \dots & \dots & \dots & \dots & \dots & \dots & \dots \\ \tilde{A}_{N1} & \tilde{A}_{N2} & \dots & \tilde{A}_{NN} & \tilde{A}_{N1'} & \tilde{A}_{N2'} & \dots & \tilde{A}_{NN'} \\ \tilde{A}_{1'1} & \tilde{A}_{1'2} & \dots & \tilde{A}_{1'N} & \tilde{A}_{1'1'} & \tilde{A}_{1'2'} & \dots & \tilde{A}_{1'N'} \\ \tilde{A}_{2'1} & \tilde{A}_{2'2} & \dots & \tilde{A}_{2'N} & \tilde{A}_{2'1'} & \tilde{A}_{2'2'} & \dots & \tilde{A}_{2'N'} \\ \dots & \dots & \dots & \dots & \dots & \dots & \dots & \dots \\ \tilde{A}_{N'1} & \tilde{A}_{N'2} & \dots & \tilde{A}_{N'N} & \tilde{A}_{N'1'} & \tilde{A}_{N'2'} & \dots & \tilde{A}_{N'N'} \end{pmatrix} \begin{pmatrix} \mu_1 \\ \mu_2 \\ \vdots \\ \mu_N \\ \mu_{1'} \\ \mu_{2'} \\ \vdots \\ \mu_{N'} \end{pmatrix} = \begin{pmatrix} RHS_1 \\ RHS_2 \\ \vdots \\ RHS_N \\ RHS_{1'} \\ RHS_{2'} \\ \vdots \\ RHS_{N'} \end{pmatrix}$$

Figure 6.2: Linear system of a symmetric configuration. The blocks highlighted with the same colors are equal.

vector, defined as:

$$\{RHS\} = -[B] \{\sigma\} - [D] \{\mu^*\}. \quad (6.2)$$

In fact, what seen above for \tilde{A} holds also for B and D , and what ascertained for vector μ applies to σ and μ^* : this leads to the symmetry patterns of vector **RHS** shown in Figure 6.3. From the symmetry between singularity intensities, System 3.19 can be rearranged as

$$\begin{aligned} (A_{j1} + A_{j1'})\mu_1 + \dots + (A_{jN} + A_{jN'})\mu_N = \\ - [(B_{j1} + B_{j1'})\sigma_1 + \dots + (B_{jN} + B_{jN'})\sigma_N] - [(D_{j1} + D_{j1'})\tilde{\mu}_1 + \dots + (D_{jN} + D_{jN'})\tilde{\mu}_N] \end{aligned} \quad (6.3)$$

and from the symmetry conditions showed in Figures 6.1 and 6.3, it is

$$\begin{aligned} (A_{j1} + A_{j1'})\mu_1 + \dots + (A_{jN} + A_{jN'})\mu_N = \\ - [(B_{j1} + B_{j1'})\sigma_1 + \dots + (B_{jN} + B_{jN'})\sigma_N] - [(D_{j1} + D_{j1'})\tilde{\mu}_1 + \dots + (D_{jN} + D_{jN'})\tilde{\mu}_N]. \end{aligned} \quad (6.4)$$

The equivalence $\tilde{A}_{j'i} = \tilde{A}_{ji'}$ (as well as $\tilde{B}_{j'i} = \tilde{B}_{ji'}$ and $\tilde{D}_{j'i} = \tilde{D}_{ji'}$) is extremely useful because simplifies the evaluation of the aerodynamic coefficients: from computational point of view, it allows to bypass the evaluation of the coordinates and the geometry of the symmetrical panel j' . The aerodynamic coefficients of the symmetric part are obtained calculating the induction of panel j on the symmetrical point i' , whose coordinates are easy to determine once the symmetry plane unit normal vector \mathbf{n}_s and a generic point P on the symmetry plane are known. From the results obtained so far and from Equation 6.4, System 3.19 can

$$\begin{pmatrix} RHS_1 \\ RHS_2 \\ \vdots \\ RHS_N \\ RHS_{1'} \\ RHS_{2'} \\ \vdots \\ RHS_{N'} \end{pmatrix} = - \begin{pmatrix} B_{11} & \dots & B_{1N} & B_{11'} & \dots & B_{1N'} \\ B_{21} & \dots & B_{2N} & B_{21'} & \dots & B_{2N'} \\ \dots & \dots & \dots & \dots & \dots & \dots \\ B_{N1} & \dots & B_{NN} & B_{N1'} & \dots & B_{NN'} \\ B_{1'1} & \dots & B_{1'N} & B_{1'1'} & \dots & B_{1'N'} \\ B_{2'1} & \dots & B_{2'N} & B_{2'1'} & \dots & B_{2'N'} \\ \dots & \dots & \dots & \dots & \dots & \dots \\ B_{N'1} & \dots & B_{N'N} & B_{N'1'} & \dots & B_{N'N'} \end{pmatrix} \begin{pmatrix} \sigma_1 \\ \sigma_2 \\ \vdots \\ \sigma_N \\ \sigma_{1'} \\ \sigma_{2'} \\ \vdots \\ \sigma_{N'} \end{pmatrix} \\
- \begin{pmatrix} D_{11} & \dots & D_{1N} & D_{11'} & \dots & D_{1N'} \\ D_{21} & \dots & D_{2N} & D_{21'} & \dots & D_{2N'} \\ \dots & \dots & \dots & \dots & \dots & \dots \\ D_{N1} & \dots & D_{NN} & D_{N1'} & \dots & D_{NN'} \\ D_{1'1} & \dots & D_{1'N} & D_{1'1'} & \dots & D_{1'N'} \\ D_{2'1} & \dots & D_{2'N} & D_{2'1'} & \dots & D_{2'N'} \\ \dots & \dots & \dots & \dots & \dots & \dots \\ D_{N'1} & \dots & D_{N'N} & D_{N'1'} & \dots & D_{N'N'} \end{pmatrix} \begin{pmatrix} \mu_1^* \\ \mu_2^* \\ \vdots \\ \mu_N^* \\ \mu_{1'}^* \\ \mu_{2'}^* \\ \vdots \\ \mu_{N'}^* \end{pmatrix}$$

Figure 6.3: Symmetry patterns in vector ***RHS***.

be reduced introducing matrices

$$\tilde{A}_{ji}^{sym} = \tilde{A}_{ji} + \tilde{A}_{ji'} \quad (6.5)$$

$$\tilde{B}_{ji}^{sym} = \tilde{B}_{ji} + \tilde{B}_{ji'} \quad (6.6)$$

$$\tilde{D}_{ji}^{sym} = \tilde{D}_{ji} + \tilde{D}_{ji'} \quad (6.7)$$

$$\cdot \quad (6.8)$$

and can be rewritten as

$$[\tilde{A}]^{sym} \{\mu\} = -[B]^{sym} \{\sigma\} - [D]^{sym} \{\mu^*\}, \quad (6.9)$$

where the orders of matrices \tilde{A}^{sym} , B^{sym} and D^{sym} are half the orders of the correspondent complete matrices \tilde{A} , B and D .

6.1.2 Velocity induction

This section examines the consequences of symmetry to the perturbation velocity inductions. Referring to the case of Figure 6.4, indicating with \mathbf{v}_i the total velocity induced in point i ,

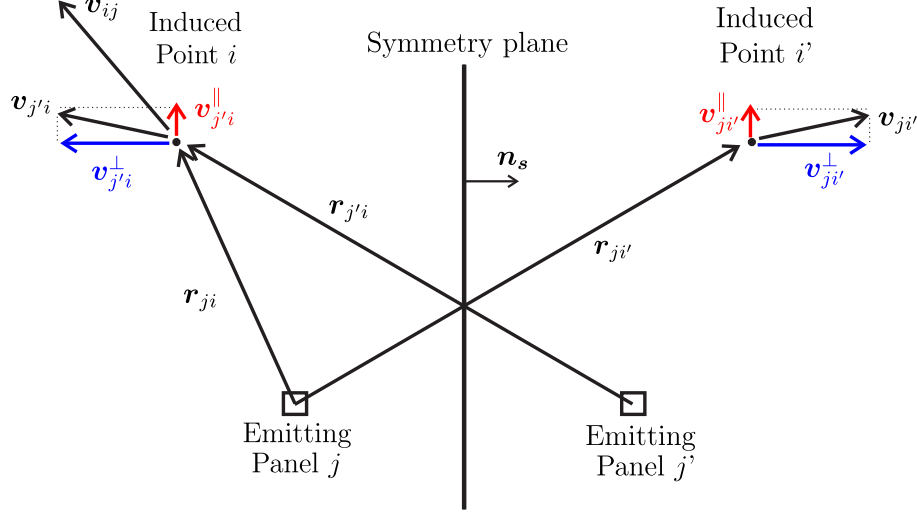


Figure 6.4: Velocity induction of an inducing panel on an induced point and their symmetric counterparts.

with \mathbf{v}_{ji} the velocity induction of panel j in point i and with $\mathbf{v}_{j'i}$ the induction of panel j' in i , it is possible to write

$$\mathbf{v}_i = \mathbf{v}_{ji} + \mathbf{v}_{j'i} \quad (6.10)$$

Given a generic vector \mathbf{a} and a unit vector \mathbf{e}_n , the following identity exists

$$\mathbf{a} = (\mathbf{a} \cdot \mathbf{e}_n) \mathbf{e}_n + (\mathbf{a} - (\mathbf{a} \cdot \mathbf{e}_n) \mathbf{e}_n) \quad (6.11)$$

where, by definition, $(\mathbf{a} \cdot \mathbf{e}_n)$ is the component of \mathbf{a} in the direction of \mathbf{e}_n and $(\mathbf{a} - (\mathbf{a} \cdot \mathbf{e}_n) \mathbf{e}_n)$ is a vector perpendicular to \mathbf{e}_n (it can be easily proven noticing that the scalar product with \mathbf{e}_n is zero). The following definitions are given

$$\mathbf{a}^{\parallel} = (\mathbf{a} \cdot \mathbf{e}_n) \mathbf{e}_n \quad (6.12)$$

$$\mathbf{a}^{\perp} = (\mathbf{a} - (\mathbf{a} \cdot \mathbf{e}_n) \mathbf{e}_n) \quad (6.13)$$

With a procedure similar to that adopted in Section 6.1.1 it is possible to show that the evaluation of the term $\mathbf{v}_{j'i}$ can be related to the velocity induction of panel j on the symmetrical point i' . Adopting the symbology of Equations 6.12 and 6.13, a similar decomposition

can be made for vector $\mathbf{v}_{j'i}$ respect to the unit vector \mathbf{n}_s , normal to the symmetry plane. As represented in Figure 6.4, it is

$$\mathbf{v}_{j'i} = -\mathbf{v}_{ji'}^{\parallel} + \mathbf{v}_{ji'}^{\perp} \quad (6.14)$$

where $\mathbf{v}_{ji'}^{\parallel}$ is the component of $\mathbf{v}_{ji'}$ parallel to \mathbf{n}_s and $\mathbf{v}_{ji'}^{\perp}$ is the component of $\mathbf{v}_{ji'}$ perpendicular to \mathbf{n}_s . Following the identity expressed by Equation 6.11, recalling Equation 6.10 and using Equation 6.14, velocity \mathbf{v}_i can be written as

$$\mathbf{v}_i = \mathbf{v}_{ji} - (\mathbf{v}_{ji'} \cdot \mathbf{n}_s) \mathbf{n}_s + (\mathbf{v}_{ji'} - (\mathbf{v}_{ji'} \cdot \mathbf{n}_s) \mathbf{n}_s). \quad (6.15)$$

6.1.3 Forces and moments evaluation

When forces and moments are evaluated, the contribution of the symmetrical part must be taken into account. Indicating with \mathbf{F}_{tot} and \mathbf{M}_{tot} the total force and moment respectively, with \mathbf{F} and \mathbf{M} force and moment of the considered geometry and with \mathbf{F}_S and \mathbf{M}_S the force and moment of the symmetrical part, it is

$$\mathbf{F}_{tot} = \mathbf{F} + \mathbf{F}_S \quad (6.16)$$

$$\mathbf{M}_{tot} = \mathbf{M} + \mathbf{M}_S. \quad (6.17)$$

The behaviour of a symmetric vector is shown in Figure 6.5; vectors \mathbf{F} and \mathbf{F}_S have been decomposed, as done in the previous section for the velocity vector, in a part perpendicular and one parallel to the symmetry plane. Indicating with \mathbf{F}^{\parallel} and \mathbf{F}_S^{\parallel} (\mathbf{F}^{\perp} and \mathbf{F}_S^{\perp}) the parallel (perpendicular) components, it can be seen that

$$\mathbf{F}^{\parallel} = -\mathbf{F}_S^{\parallel} \quad (6.18)$$

$$\mathbf{F}^{\perp} = \mathbf{F}_S^{\perp}. \quad (6.19)$$

Thus, substituting in Equation 6.16, it is

$$\mathbf{F}_{tot} = (\mathbf{F}^{\parallel} + \mathbf{F}^{\perp}) + (-\mathbf{F}^{\parallel} + \mathbf{F}^{\perp}) = 2\mathbf{F}^{\perp}. \quad (6.20)$$

Same considerations are valid for the total moment \mathbf{M}_{tot} . The difference is that moments are pseudovectors: in presence of a symmetry, magnitude and direction are mirrored, while the sign is inverted. Figure 6.6 shows the behaviour of a pseudovector in respect to symmetry. With the same symbology used for the force vector, it is

$$\mathbf{M}^{\parallel} = \mathbf{M}_S^{\parallel} \quad (6.21)$$

$$\mathbf{M}^{\perp} = -\mathbf{M}_S^{\perp} \quad (6.22)$$

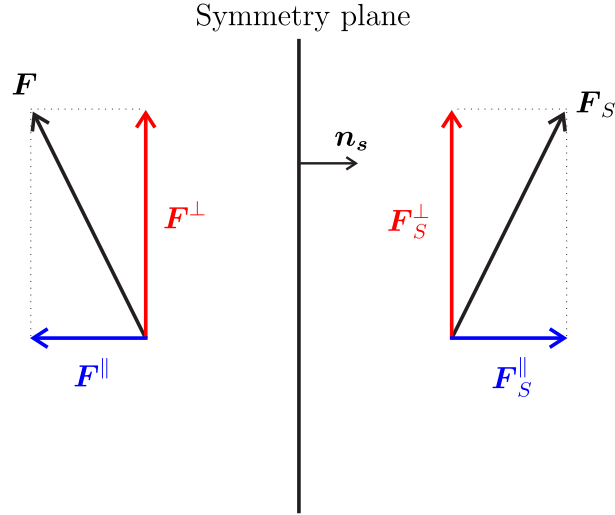


Figure 6.5: The sum of vector \mathbf{F} and its symmetrical \mathbf{F}_S is given by sum of the contributions of the components perpendicular to the symmetry plane normal, being the parallel components opposite.

and from Equation 6.17 the total moment can be expressed as

$$\mathbf{M}_{tot} = (\mathbf{M}^{\parallel} + \mathbf{M}^{\perp}) + (\mathbf{M}^{\parallel} - \mathbf{M}^{\perp}) = 2\mathbf{M}^{\parallel}. \quad (6.23)$$

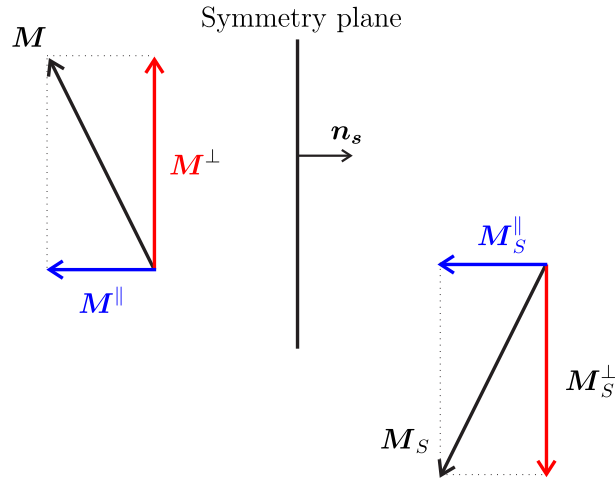


Figure 6.6: The sum of vector \mathbf{M} and its symmetrical \mathbf{M}_S is given by sum of the contributions of the components parallel to the symmetry plane normal, being the perpendicular components opposite due to the pseudo-vector nature of \mathbf{M} .

6.2 Zero-thickness bodies: vortex lattice method

In general, for aerodynamic bodies effects of thickness on the lift are of second-order in respect to those related to the wing planform shape and angle of attack. For this reason, in some cases it can be convenient to model a body only by its mean surface (zero-thickness surface), with the advantage of reducing the number of panels (by approximatively a factor of 2) required for the simulation. To represent zero-thickness bodies the formulation for the solution of potential flows has to be slightly modified.

6.2.1 Vortex lattice method

For zero-thickness bodies, the BEM problem will be reformulated in terms of perturbation velocity instead of perturbation potential. First, all the zero-thickness surfaces are divided into plane quadrilateral panels, whose geometry and properties are the same of the body and wake panels introduced in Section 3.1. As singularities, the vortex rings are used: every panel correspond to a vortex ring, whose filaments coincides with the panel edges.

Some authors (see, for example, [17]) recommend to place the vortex ring centers at $\frac{3}{4}$ of the panel's chord; in the present panel code the vortex rings centers coincides with the panel centers (collocation points) to preserve the analogy with the doublet panels presented in the previous sections.

Recalling Equation 2.16, zero normal flow across the body solid surface is required:

$$\nabla(\varphi + \Phi_\infty) \cdot \mathbf{n} = 0. \quad (6.24)$$

This condition has to be enforced at every collocation point on the body surface. In a discretized form, it is

$$(\mathbf{v}_k + \mathbf{V}_{\infty k}) \cdot \mathbf{n}_k = 0, \quad (6.25)$$

where \mathbf{v}_k is the perturbation velocity induced by all the body and wake vortex rings on the k -th collocation point. Indicating with Γ_i the strength of the i -th vortex ring on the body surface and with Γ_j^w the j -th vortex ring on the wake surface, and assuming that N_b and N_w are the number of body and wake panels respectively, Equation 6.25 can be rewritten as

$$\sum_{i=1}^{N_b} a_{ki} \Gamma_i + \sum_{j=1}^{N_w} b_{kj} \Gamma_j^w = -\mathbf{V}_{\infty k} \cdot \mathbf{n}_k, \quad (6.26)$$

where, from the Biot-Savart equation (Equation 3.39), it holds

$$a_{ki} = \frac{1}{4\pi} \oint_{C_i} \frac{(\mathbf{y} - \mathbf{x}_k) \times d\mathbf{l}(\mathbf{y})}{\|\mathbf{y} - \mathbf{x}_k\|^3} \cdot \mathbf{n}_k \quad (6.27)$$

$$b_{kj} = \frac{1}{4\pi} \oint_{C_j} \frac{(\mathbf{y} - \mathbf{x}_k) \times d\mathbf{l}(\mathbf{y})}{\|\mathbf{y} - \mathbf{x}_k\|^3} \cdot \mathbf{n}_k. \quad (6.28)$$

For the wake rings' intensities, results of Equation 2.37 are still valid; all the far wake vortex rings intensities are known from the previous timesteps. An unsteady equivalent of the Kutta condition is to set the intensity of a wake ring on trailing edge (near wake) equal to the intensity of the correspondent body panel on the same trailing edge:

$$\Gamma_l^w = \Gamma_l, \quad (6.29)$$

where l is an index that runs on the trailing edge. Indicating with N_{nw} the number of panels of the near wake and with N_{fw} the panels on the far wake, Equation 6.26 can be rewritten as

$$\sum_{i=1}^{N_b} a_{ki} \Gamma_i + \sum_{l=1}^{N_{nw}} c_{kl} \Gamma_l^w + \sum_{j=1}^{N_{fw}} b_{kj} \Gamma_j^w = -\mathbf{V}_{\infty k} \cdot \mathbf{n}_k, \quad (6.30)$$

having indicated with c_{kl} the expression

$$c_{kl} = \frac{1}{4\pi} \oint_{C_l} \frac{(\mathbf{y} - \mathbf{x}_k) \times d\mathbf{l}(\mathbf{y})}{\|\mathbf{y} - \mathbf{x}_k\|^3} \cdot \mathbf{n}_k. \quad (6.31)$$

Enforcing the condition expressed in Equation 6.29, the term \tilde{a}_{ki} can be introduced, where

$$\begin{cases} \tilde{a}_{ki} = a_{ki} & \text{if panel } i \text{ is not a trailing edge panel} \\ \tilde{a}_{kl} = a_{kl} + c_{kl} & \text{if panel } l \text{ is a trailing edge panel.} \end{cases} \quad (6.32)$$

The right hand side of Equation 6.30 is known and the system can be solved, obtaining the vortex intensities Γ .

6.3 Mixed problem

The present panel code does not preclude the possibility to model, in the same simulation, bodies with thickness (doublet/source formulation) and zero-thickness surfaces (vortex lattice). In this case, the on each body the proper boundary condition will be enforced; if collocation point k belongs to a three dimensional body with thickness, then the boundary condition will be expressed in terms of potential

$$\varphi_k = 0. \quad (6.33)$$

If point k lies on a zero-thickness surface, then the boundary condition involves the velocity

$$\nabla (\varphi_k + \Phi_{\infty k}) \cdot \mathbf{n}_k = 0. \quad (6.34)$$

In case of mixed formulation, the equivalence between doublets and vortex rings plays a key-role. In fact, the singularities on the zero-thickness surface will induce perturbation potential as doublets if the receiving point is on a body with thickness and will induce velocity as vortex rings if the receiving point belongs to a zero-thickness body. The same holds for the singularities on bodies with thickness: doublets and sources will induce velocity or perturbation potential according to the boundary condition to be enforced on the receiving collocation point. Figure 6.7 tries to clarify the concept with an example. Consider a thick

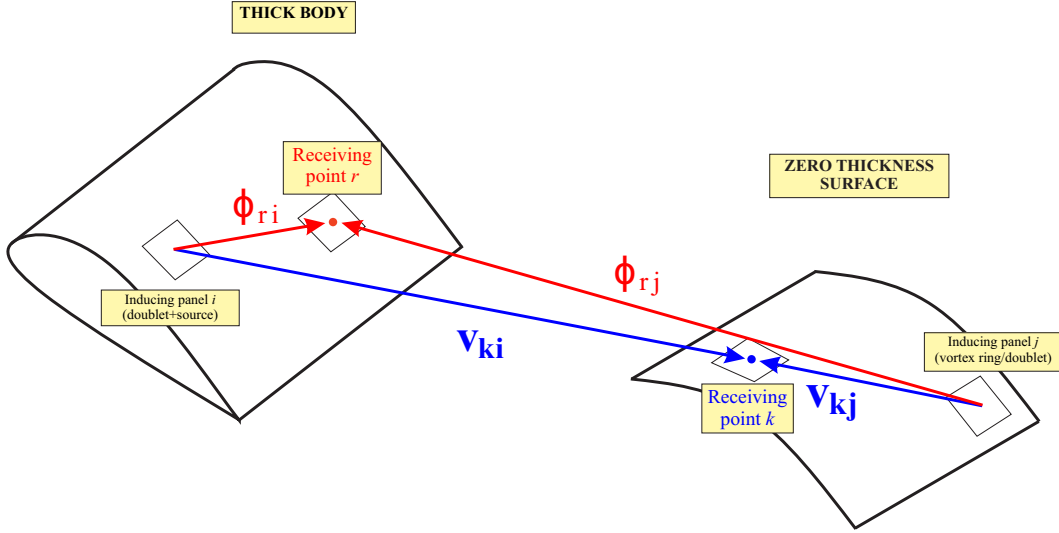


Figure 6.7: The panels on both kind of bodies (thick and zero-thickness) induce perturbation potential or velocity depending on the receiving collocation point.

body with N_t body panels (doublets and sources) and a zero-thickness body with N_z panels (doublets/vortices). The intensity of a body panel doublet/vortex ring is indicated with μ . The far wake panels N_{fw} include the wake panels shed by both bodies and their intensities are μ^* . Indicating with k a collocation point on the zero thickness surface and with r a panel on the thick body surface, the linear system obtained enforcing the proper boundary condition on every collocation point becomes

$$\begin{cases} \sum_{i=1}^{N_t} \tilde{A}_{ki}^* \mu_i + \sum_{j=1}^{N_z} a_{kj} \mu_j = -\mathbf{V}_{\infty k} \cdot \mathbf{n}_k - \sum_{i=1}^{N_t} B_{ki}^* \sigma_i - \sum_{l=1}^{N_{fw}} b_{kl} \mu_l^* \\ \sum_{i=1}^{N_t} \tilde{A}_{ri} \mu_i + \sum_{j=1}^{N_z} A_{rj} \mu_j = -\sum_{i=1}^{N_t} B_{ri} \sigma_i - \sum_{l=1}^{N_{fw}} D_{rl} \mu_l^* \end{cases} \quad (6.35)$$

where, recalling the symbology used in Section 3.3, it is

$$\tilde{A}_{ki}^* = \nabla \tilde{A}_{ki} \cdot \mathbf{n}_k \quad (6.36)$$

$$(6.37)$$

$$B_{ki}^* = \nabla B_{ki} \cdot \mathbf{n}_k.$$

The solution of the linear system is the vector of the body doublets/vortices strengths.

The body pressures are evaluated on the thick body surface using Bernoulli Equation 3.47. For the zero-thickness surfaces the pressure calculation requires a different formulation of the Bernoulli theorem (see [17]) that is not taken into account in this work. In this work the modeling of zero-thickness bodies is limited to evaluate the influence they have on other bodies. An example is shown in Figure 6.8.

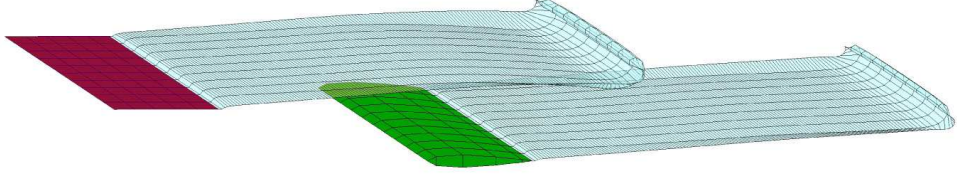


Figure 6.8: The simulation is focused on the evaluation of the influence the wake of the upstream wing has on the forces of the downstream wing. As the calculation of the forces on the upstream wing is not required, it is modeled as a zero-thickness surface, to reduce the computational costs. The forces will be evaluated only on the thick downstream wing.

Chapter 7

Validations

In this chapter the code will be validated. Four classical test cases, for which experimental or analytical solutions are available in literature, are simulated with the panel code and the results are compared and discussed.

The first test case is the comparison of the evolution of lift of an airfoil with the analytical solution of an impulsive starting flat plate obtained by Wagner.

The second test case, useful to validate the predictive capabilities of the code for unsteady flows, is based on the theory of oscillating airfoils developed by Theodorsen [30]; the results of lift and pitching moment for a pitching and plunging airfoil are compared with the analytical solution. The results are obtained for different reduced frequencies (an index of the unsteadiness of the flow) and different values of thickness.

The third test case concerns the simulation of a three-blade propeller, for which experimental results are available in literature.

Finally, for the validation of the alternative boundary formulation for body-wake impingement, pressure coefficients at different span sections of the blades of a two-blade rotor are compared with the experimental results obtained by Caradonna and Tung [9].

7.1 Wagner-based test case

The problem of a flat plate undergoing a step change in angle of attack in an incompressible and inviscid flow was studied by Wagner, who was able to derive an exact analytical solution for the evolution of the lift. At time $t < 0$ a flat plate is immersed in a free stream flow V_∞ with zero angle of attack α . In this case, the total circulation around the flat plate is zero and no lift is generated. At time $t=0$ the angle of attack α is impulsively set to

$\alpha = \alpha_0$: at this point a circulation develops around the flat plate and vorticity is shed into the wake at the plate trailing edge, generating the so called *starting vortex*. In the very first timesteps, the circulation on the body and the circulation shed into the wake are of the same order; the downwash induced by the wake significantly reduces the lift generated by the flat plate but this influence decreases as the starting vortex is convected downstream by the free-stream velocity. When the starting vortex is sufficiently distant from the body, its influence is negligible and the solution with the fully developed wake tends to a steady state. It is important to remark that the steady state is an asymptotic condition and cannot be reached in a numerical code; a good approximation of the steady state is obtained when the variation in time of the variables involved in the simulation is negligible respect to their absolute values.

To account for the lift changes due to the starting vortex during the transient between zero lift at zero angle of attack and lift with fully developed wake (a good approximation of the asymptotic steady state), Wagner introduced a *lift deficiency function* $\phi(s)$, where $s = \frac{2}{c} \int_0^t V_\infty dt$ is the dimensionless time. The expression of the two-dimensional lift coefficient evolution in time for a flat plate, according to small perturbation theory with the introduction of Wagner's function is

$$C_l(s) = \frac{\pi c}{2V_\infty} \delta(s) + 2\pi\alpha\phi(s), \quad (7.1)$$

where $\delta(s)$ is the Dirac delta function. Theoretically, the flat plate is affected by an infinite pulse at $t = 0^+$ due to the noncirculatory loading [22], then the evolution of lift follows the trend of Wagner's function, which can be seen as the ratio between the lift generated at the considered time and the steady state lift coefficient given by the small perturbation theory

$$\frac{C_l(t)}{2\pi\alpha} = \phi(s) \quad \text{for } t > 0. \quad (7.2)$$

Wagner function values, plotted in Figure 7.1, depend on a modified Bessel function [22] which is well approximated by the exponential expression

$$\phi(s) = 1 - 0.165e^{-0.0455s} - 0.335e^{-0.3s}. \quad (7.3)$$

Not considering the initial infinite pulse, at time $s = 0$ the value of Wagner's function is 0.5: this means that the initial lift reduction due to the presence of the starting vortex is half of the steady state value. The lift reduction progressively decreases as s increases and for $s \rightarrow \infty$ it is $\phi(s) \rightarrow 1$.

The results obtained by Wagner are compared to the time evolution of the lift coefficient of the wing C_L of a rectangular, untapered, finite wing with aspect ratio $AR = 500$, which is

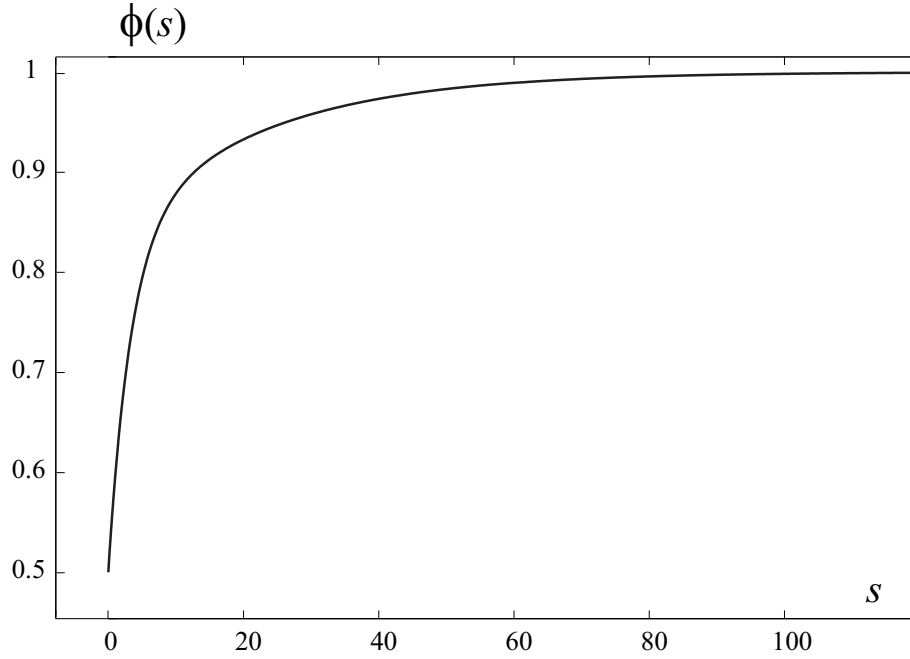


Figure 7.1: Wagner's function: exponential approximation.

impulsively set in motion with an angle of attack $\alpha = 5^\circ$. The wing sections are symmetrical 4-digit NACA airfoils 0012. The wing is represented by a mesh of 4040 panels: 40 chordwise, 100 spanwise and 20 on each plug at the wing lateral side. The chordwise panel distribution is not uniform, it is refined towards the leading edge and the trailing edge, where greater velocity gradients are expected. In Figure 7.2 the evolution of function $C_L(s)/C_{L_\infty}$ (where C_{L_∞} is the wing steady state lift coefficient) is compared to the analytical Wagner's function. In this simulation the iterative Kutta condition has not been applied and the wake roll-up has been disabled (rigid wake) to better reproduce the analytical model. In the next figures, all the results obtained with the present code will be indicated with *UPM*. The panel code reproduces well the trend of the lift evolution; some small differences can be related to the finiteness of the wing and to the fact that the wing section is not a flat plate but a NACA 0012 airfoil. By the way, a significant difference in the lift deficiency peak can be noticed in the very first timesteps of the simulation. This issue has already been noticed by other authors [17]: Katz recommends to reduce the dimension in the free-stream directions of the panels of the near wake, suggesting a value between 20% and 30% of the quantity $V_\infty \Delta T$, where ΔT is the timestep chosen for the numerical simulation. Following this suggestion, the simulation has been repeated and the convection distance of the near wake has been set to $0.2V_\infty \Delta T$. The results are shown in Figure 7.3. In this case the lift evolution is closer to the

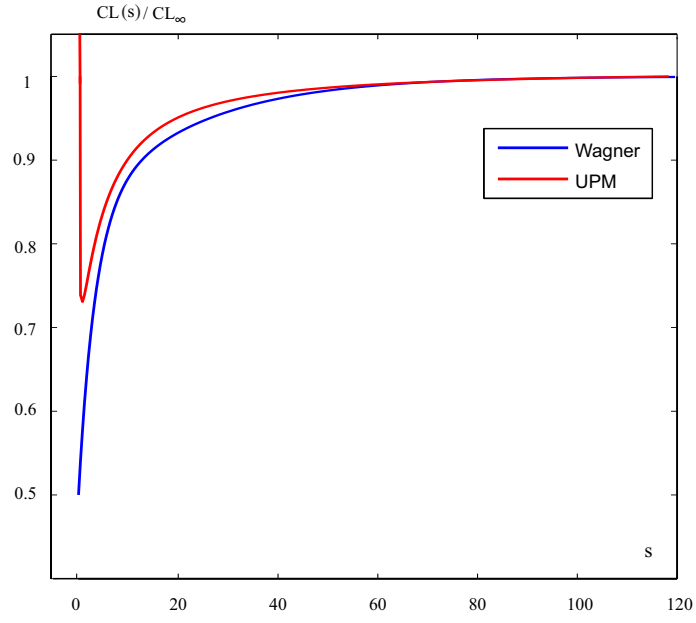


Figure 7.2: C_L/C_{L_∞} : comparison between Wagner's analytical equation (applied to a bidimensional flat plate) and panel code (on a very high aspect ratio wing) results.

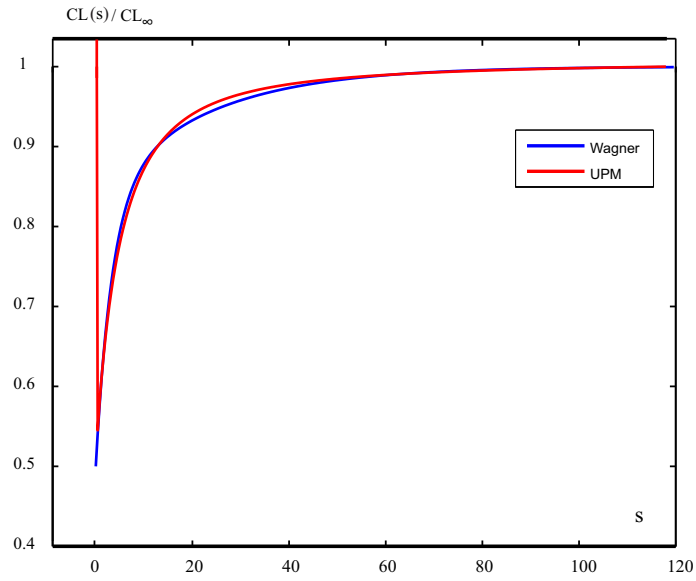


Figure 7.3: C_L/C_{L_∞} : in this simulation the near wake panels have been moved closer to the trailing edge, as suggested in [17].

analytical solution. Figure 7.4 shows the lift evolution for different aspect ratio rectangular, untapered wings. The wing sections are NACA 0012 airfoils and ΔT as been chosen such as the parameter $\frac{V_\infty \Delta T}{c} = 0.1$. The results are shown both for free wake and for rigid wake: the free wake simulations have a smaller lift coefficient compared to the rigid wake ones and the steady state lift coefficient increases with the aspect ratio.

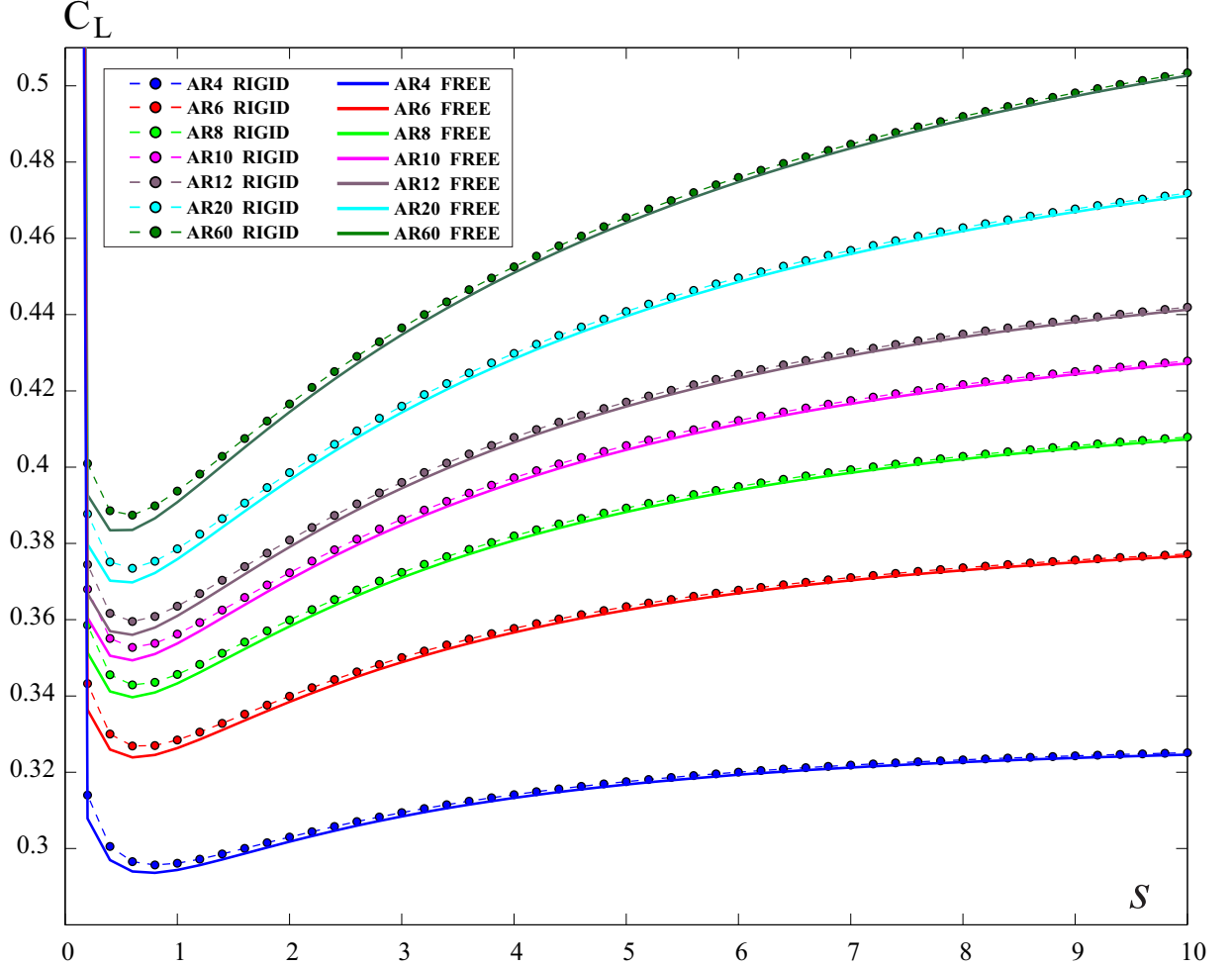


Figure 7.4: C_L evolution for rectangular wings of different aspect ratio at 5° angle of attack. Comparison between free wake and rigid wake.

7.2 Theodorsen-based test case

One of the feature of the unsteady panel code is the ability to predict unsteady loads due to the motion of a body in a uniform free-stream. The problem of an oscillating airfoil is a good

example to test the kinematic module and to validate the predictivity of the code, comparing the results of lift and pitching moment with those provided by the classical theory.

7.2.1 Theodorsen's theory: brief outline

The problem of an oscillating symmetrical airfoil in an incompressible, inviscid flow was studied by Theodorsen who, starting from the thin-airfoil theory, was able to provide an analytical expression for lift and pitching moment. The hypothesis behind the classical thin-airfoil theory and all the details about the procedure adopted by Theodorsen will be omitted in this thesis [22]; it is enough to say that the effects of thickness are neglected and the airfoil is represented by a continuous distribution of vortices along its mean line (a flat plate in case of symmetrical airfoil). The motion of the airfoil produces a distribution of perturbation velocities normal to the chord, which are taken into account to enforce the flow tangency condition on the flat plate, necessary to find the unknown strength of the vortex distribution. The wake too is represented by vortices and the Kutta condition is enforced at the flat plate trailing edge. It is important to underline that the wake is considered to be flat: the vortices are projected on a sort of 'wake mean line', as shown in Figure 7.5. In Figure 7.6 the reference

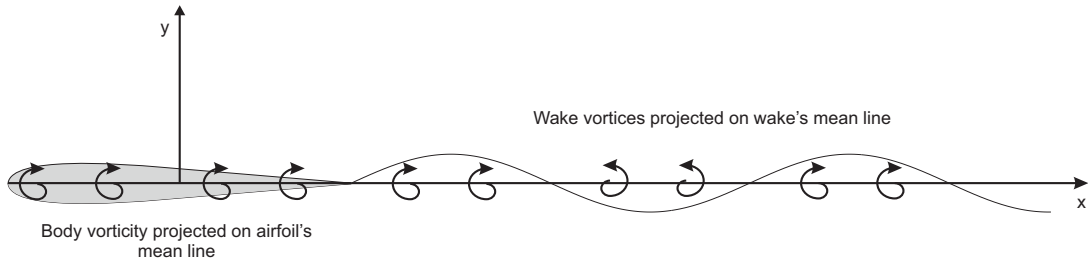


Figure 7.5: Summary of Theodorsen's classical vortex theory. Body and wake are represented by a distribution of vortices projected on body's and wake's mean lines.

system attached to the flat plate is shown; c is the flat plate chord and b the semi-chord, while a is the dimensionless coordinate of the flexural axis ($a = \frac{x_f}{b}$). It is possible to decompose the oscillating motion of the flat plate in the sum of the contributions of angular oscillations around its flexural axis (pitching) and translational oscillations along z axis (plunging). To characterize the unsteadiness of motion, *reduced frequency* k is introduced

$$k = \frac{\omega b}{V} = \frac{\omega c}{2V} \quad (7.4)$$

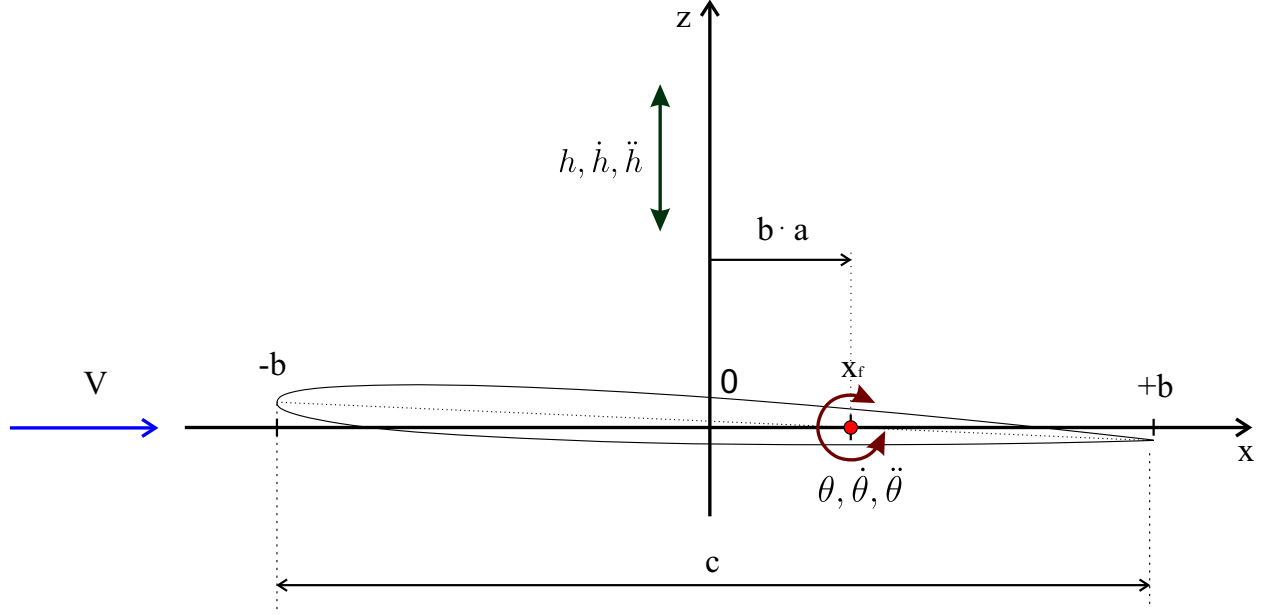


Figure 7.6: Reference system, with origin at airfoil's mid-chord, used to describe the problem of the oscillating airfoil.

where ω is the frequency of the oscillations. For $k = 0$ the flow is steady, while for $0 \leq k \leq 0.05$ it can be considered *quasi-steady* (that means that the unsteady terms of the governing equations can be neglected). For values of the reduced frequency larger than 0.05 the flow is considered unsteady and the unsteady terms (such as those related to accelerations effects like added mass) cannot be neglected; in particular, for values greater than 0.2 the flow is *highly unsteady* and the aerodynamic loads are dominated by the unsteady terms. The solution of the Theodorsen problem in terms of lift and pitching moment around the flexural axis can be decomposed in the contribution of a circulatory term, originating from the creation of circulation around the airfoil, and a non-circulatory term, due to the effects of the fluid acceleration. Indicating with $\theta, \dot{\theta}, \ddot{\theta}$ the pitching angle around the flexural axis, its first and second temporal derivatives respectively and with h, \dot{h}, \ddot{h} the displacement, velocity and acceleration along axis z , the expressions for the circulatory and non-circulatory contributions to lift and pitching moment, according to [22], are:

$$L_{NC} = \pi \rho b^2 [\ddot{z} + U \dot{\alpha} - ba \ddot{\alpha}] \quad (7.5)$$

$$L_C = 2\pi \rho U b \left[\dot{z} + U \alpha + b \left(\frac{1}{2} - a \right) \dot{\alpha} \right] \quad (7.6)$$

$$M_{NC_{x_f}} = \pi \rho b^2 \left[ba \ddot{z} - Ub \left(\frac{1}{2} - a \right) \dot{\alpha} - b^2 \left(\frac{1}{8} + a^2 \right) \ddot{\alpha} \right] \quad (7.7)$$

$$M_{C_{x_f}} = 2\pi\rho Ub^2 \left(a + \frac{1}{2}\right) \left[\dot{z} + U\alpha + b \left(\frac{1}{2} - a\right) \dot{\alpha} \right]. \quad (7.8)$$

To account for the effects of the wake on the plate airloads, the circulatory terms of the equations are multiplied by the so-called *Theodorsen's function* $C(k) = F(k) = iG(k)$, a complex function of k . $C(k)$ is known only when the plate motion is sinusoidal: in that case $C(k)$ can be expressed in terms of Hankel functions [22] $H_1^{(2)}$ and $H_0^{(2)}$:

$$C(k) = F(k) + iG(k) = \frac{H_1^{(2)}(k)}{H_1^{(2)}(k) + H_0^{(2)}(k)}. \quad (7.9)$$

The final expressions of lift and pitching moment around the airfoil flexural axis in terms of dimensionless coefficients are

$$C_l = \pi b \left(\frac{\ddot{z}}{U^2} + \frac{\alpha}{U} - \frac{ba}{U^2} \ddot{\alpha} \right) + 2\pi C(k) \left[\frac{\dot{z}}{U} + U\alpha + b \left(\frac{1}{2} - a\right) \frac{\dot{\alpha}}{U} \right]. \quad (7.10)$$

$$\begin{aligned} C_{m_{x_f}} = & \frac{\pi}{2} \left[\frac{ba\ddot{z}}{U^2} - \frac{b}{U} \left(\frac{1}{2} - a\right) \dot{\alpha} - \frac{b^2}{U^2} \left(\frac{1}{8} + a^2\right) \ddot{\alpha} \right] \\ & + \pi \left(a + \frac{1}{2}\right) \left[\frac{\dot{z}}{U} + \alpha + b \left(\frac{1}{2} - a\right) \frac{\dot{\alpha}}{U} \right] C(k) \end{aligned} \quad (7.11)$$

For the validations, a rectangular untapered NACA 0012 wing of aspect ratio $AR = 12$ is considered. The first set of simulations concerns the wing undergoing oscillations along the vertical axis z (pure heaving) at different reduced frequencies. The amplitude of the oscillations is $0.05c$. Results from the unsteady panel code are compared to the analytical solution obtained by Theodorsen, in terms of lift coefficient and pitching moment coefficient around mid-chord. The same comparisons are repeated in case of pure pitching around mid-chord point. In this case, three different amplitude oscillations are tested: 1° , 2° and 4° . For all the simulations the wake is considered rigid and the iterative Kutta condition is applied.

In Table 7.1 the details of the simulations are listed and in the next sections the results are presented and discussed.

7.2.2 Pure heaving

Figures 7.7 and 7.8 show the comparison between the panel code and Theodorsen results. The results are in good agreement, and as expected they tend to be closer as the reduced frequency decreases. The mayor differences are probably consequence of Theodorsen's assumptions (flat plate, plane wake).

Mesh details	Reduced frequency k	Dimensionless time interval $\frac{\Delta TV_\infty}{c}$
30 panels spanwise 40 panels chordwise	π	0.01667
	$\pi/2$	0.03333
	$\pi/4$	0.05000
	$\pi/16$	0.26667
	$\pi/40$	0.50000

Table 7.1: Simulation details.

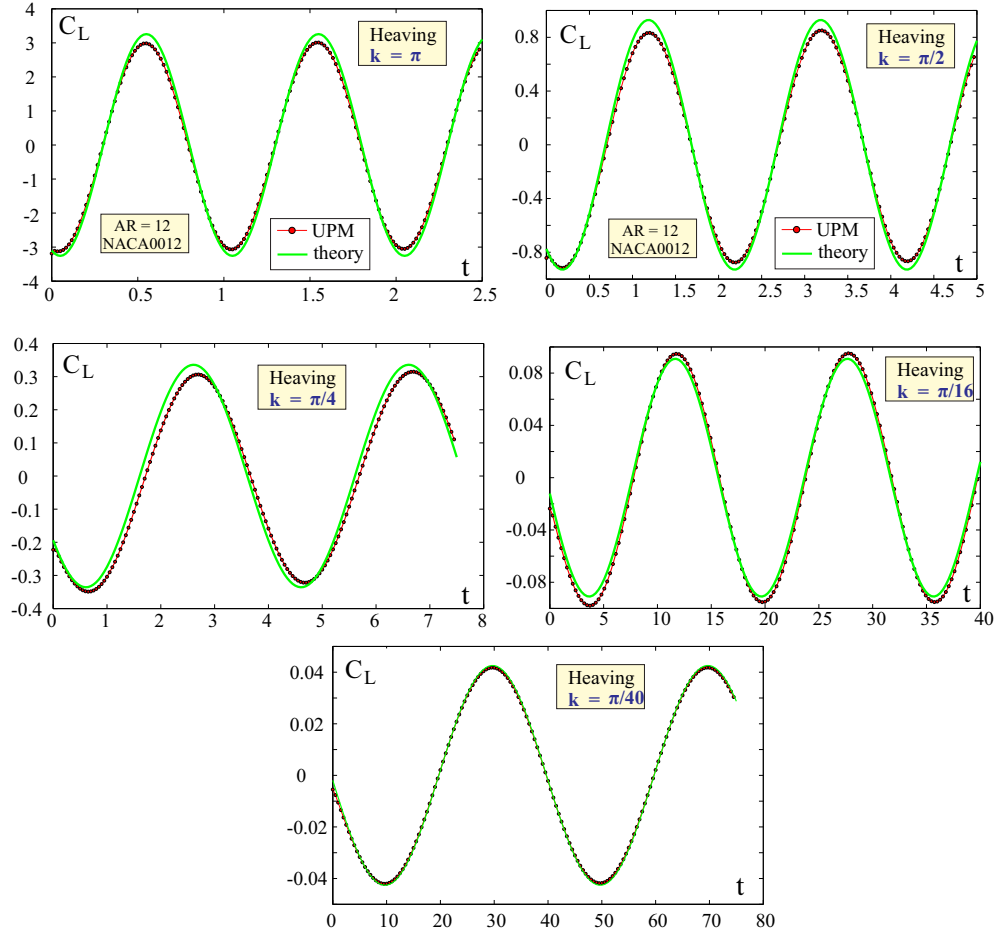


Figure 7.7: C_L comparison between Theodorsen solution and UPM results for a heaving wing at different reduced frequencies.

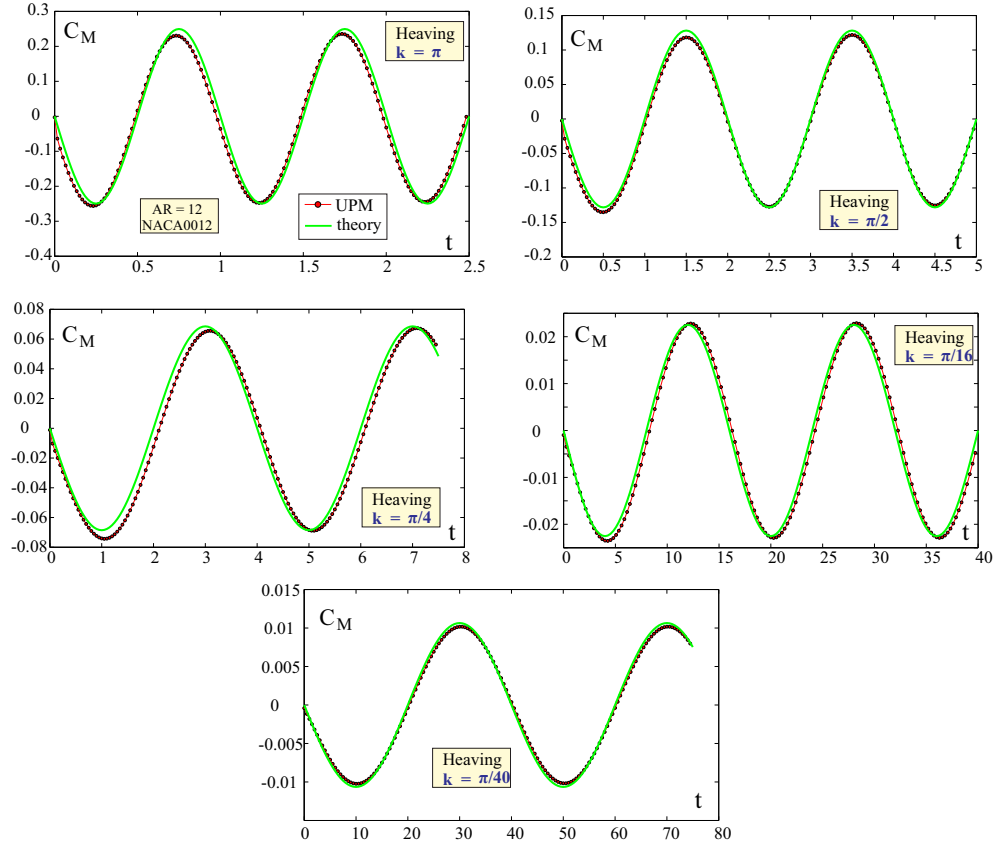


Figure 7.8: C_M around mid-cord comparison between Theodorsen solution and UPM results for a heaving wing at different reduced frequencies.

Thickness effect

Figure 7.9 shows the effect of thickness on the heaving simulation. As expected, when thickness decreases the results in terms of C_L are closer to the analytical solution (flat plate).

7.2.3 Pure pitching

The results for a pure pitching wing are shown in Figure 7.10 and Figure 7.11. For each reduce frequency, three different amplitude oscillations are tested: as Theodorsen theory has been developed from the hypothesis of small perturbations, thus, as expected, best correlation is achieved for the small amplitude case.

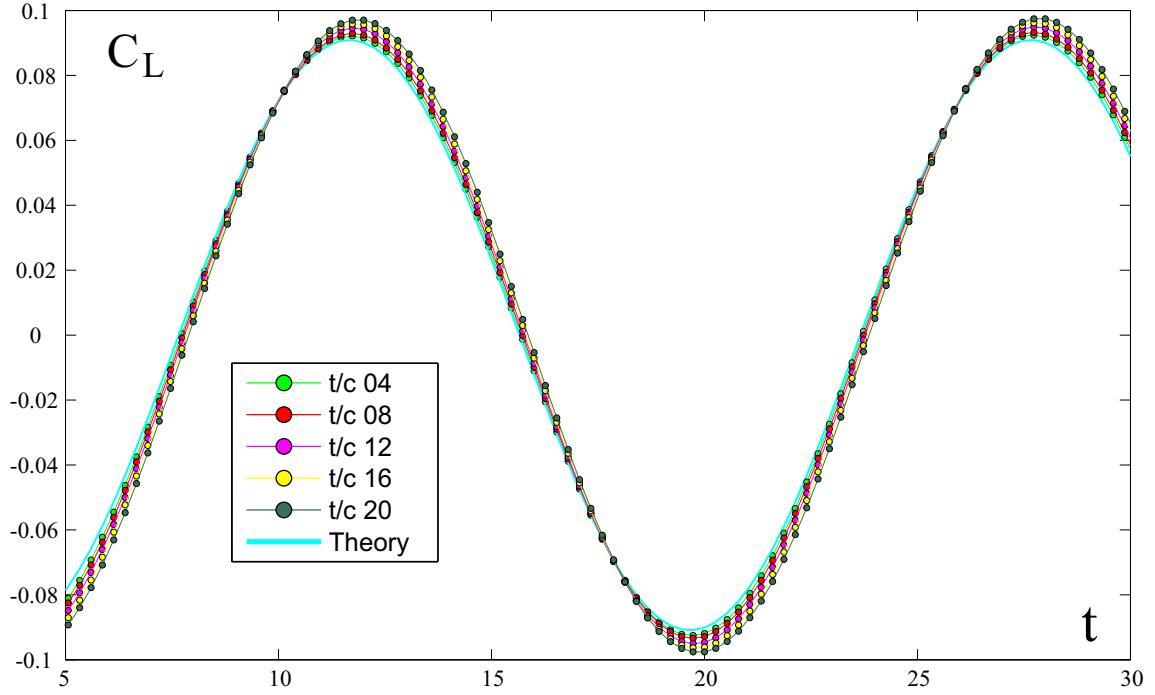


Figure 7.9: C_L comparison between Theodorsen solution and UPM results for a heaving wing at reduced frequency $k = \pi/16$ and for different values of the relative thickness of the wing.

7.3 Propeller - Biermann and Gray 1942 NACA report

In the previous sections, the capability of the panel code to predict unsteady aerodynamic loads has been validated with analytical solutions of two well know problems of classical theory. As one of the aims of this work is to study the performance of propellers, the code has been tested on the three-blade pusher propeller described in NACA Wartime report [7]. The thrust coefficient and power coefficient curves obtained with the panel code have been compared to the experimental result listed in the NACA report. All the details of the experiment are described in reference [7] and will be briefly summarized here. The case examined is a three-blade single-rotating pusher propeller with a 10-foot diameter, mounted at the rear end of a streamlined body which covers the hubs. The experimental results have been obtained in a 20-foot propeller research wind tunnel. Figure 7.12 depicts the geometry of the propeller, the disposition of the blades and the surface mesh. In the numerical simulation performed by the panel code, only the blades have been modeled and the presence of the spinner has been omitted, considering its effects negligible for the purposes of code validation.

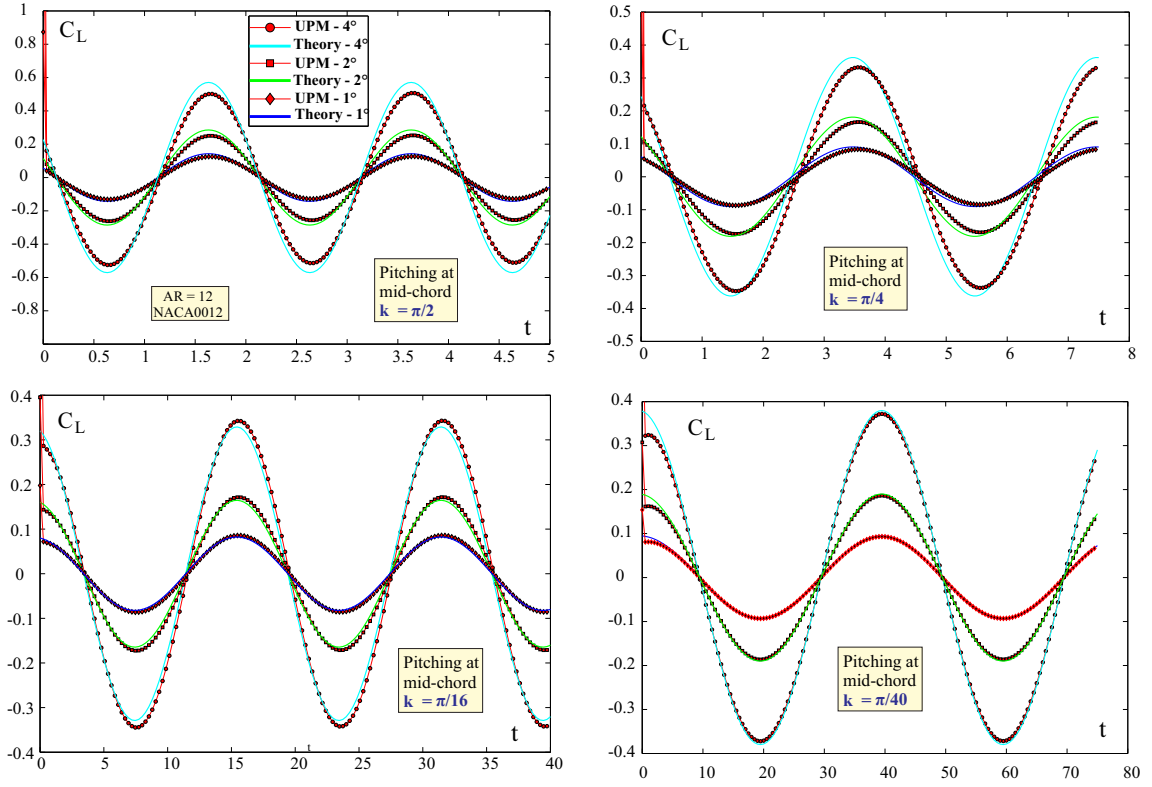


Figure 7.10: C_L comparison between Theodorsen solution and UPM results for a heaving wing at different reduced frequencies.

Thrust and power of the propeller are expressed in terms of dimensionless coefficients:

$$C_T = \frac{T}{\rho n^2 D^4} \quad \text{Thrust coefficient} \quad (7.12)$$

$$C_P = \frac{2\pi n Q}{\rho n^3 D^5} \quad \text{Power coefficient} \quad (7.13)$$

where

$$\begin{aligned} T &= \text{thrust} [N] \\ Q &= \text{torque} [Nm] \\ \rho &= \text{air density} \left[\frac{Kg}{m^3} \right] \\ n &= \text{revolutions per second} \left[\frac{1}{s} \right] \\ D &= \text{propeller diameter} [m] \end{aligned} \quad (7.14)$$

In Figure 7.13 the results of the panel code and the experiment data are compared. The dimensionless parameter in abscissa is the advance ratio $J = \frac{V_\infty}{nD}$. The results show good agreement for some advance ratios, while they diverge as the advanced ratio decreases. This is probably due to the flow separation, whose effects are not taken into account in the unsteady

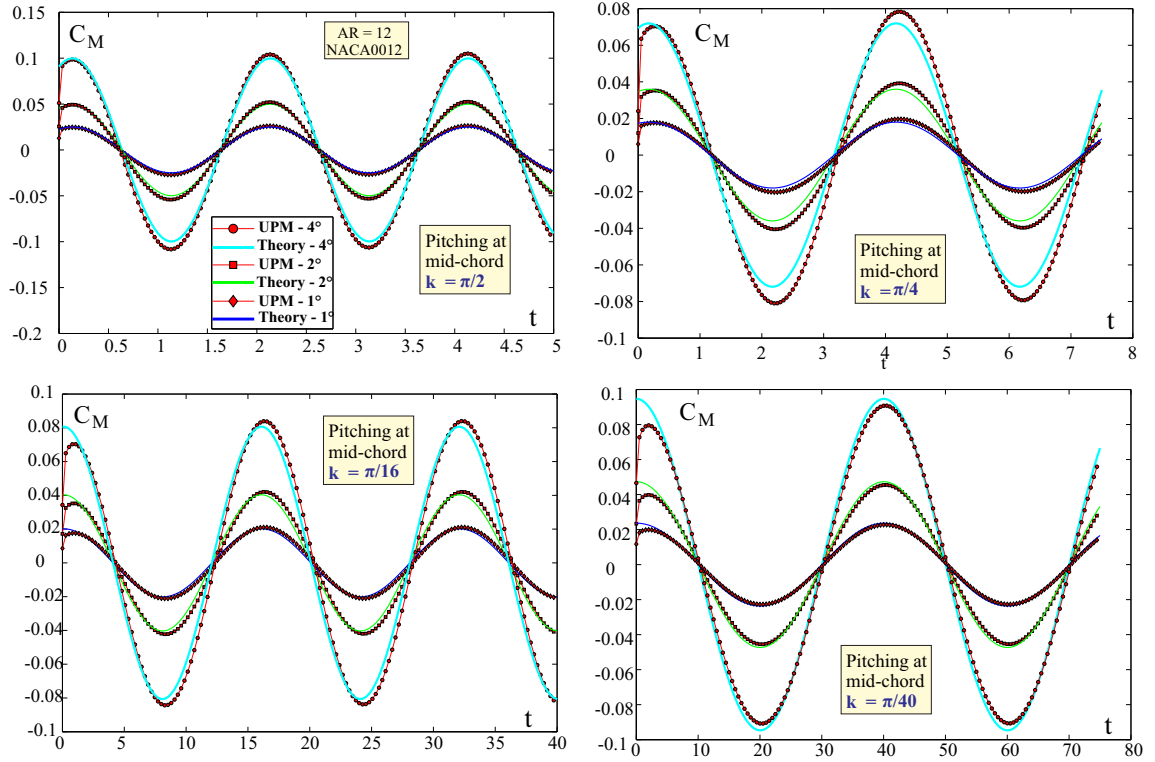


Figure 7.11: C_M around mid-cord comparison between Theodorsen solution and UPM results for a heaving wing at different reduced frequencies.

panel method, while they were obviously captured in the experiment. It is interesting to see that the power coefficient is less influenced by the separation; a possible cause could be that the separation occurs near the root of the blades, affecting those sections that give less contribution to the total torque.

7.4 Caradonna-Tung experiment

The validations performed so far do not include any case of wake-body impingement. As already introduced, in all those cases in which a wake comes too close or impinges a body, the BEM formulation has to be modified: the wake will be considered made up of vortex rings, thanks to the analogy between vortex rings and doublets. This allows to introduce a regularization in the vortex inductions and even in those cases in which a wake penetrates a body, the induced potential remains bounded.

A classical test found in literature, known as Caradonna-Tung experiment [9], involves a two-blade rotor made of two rectangular untapered NACA 0012 wings. Figure 7.14 and

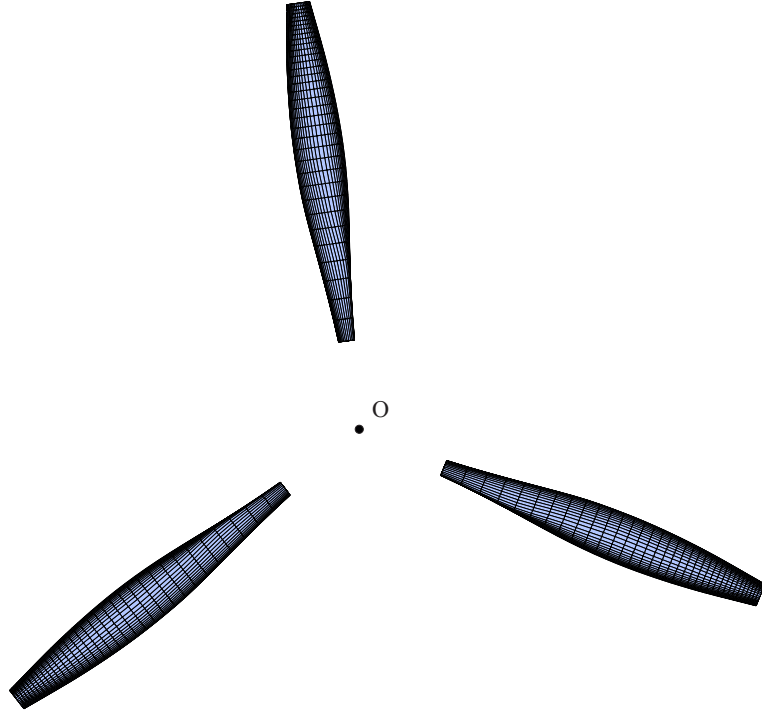


Figure 7.12: Geometry and surface mesh.

Figure 7.15 show the set-up of the experiment, with the dimensions of the objects involved. The rotor was tested in wind tunnel and, through pressure probes placed on the wing surface, the chordwise pressure coefficient distribution was obtained for specific sections. This test is particularly interesting because the rotors start from rest and there is no wind. This implies that during the first revolutions the wake is not convected downstream, but stays close to the blades. While this fact has no consequences in a real experiment, in the panel code it represents a problem because the wake impinges the blades several times in the first revolution; without the alternative vortex ring formulation, this would lead to instabilities, resulting in completely inaccurate results. For a rotational speed of 1200 rpm , a collective pitch $\theta = 8^\circ$ and a tip Mach number $M = 0.52$, the comparison between experimental results and numerical simulation in terms of pressure coefficients is presented in Figure 7.16. The three considered sections where the C_p is measured are, respectively, $r/R = 0.68$, $r/R = 0.80$ and $r/R = 0.96$, being R the blade radius and r is the span-wise coordinate. The code results and the experimental data are in good agreement and the main trend of the C_p distribution is well captured. It has to be said that no iterative Kutta condition has been applied (this can be seen in observing the pressure coefficients on trailing edge), resulting in possible inaccuracies of the C_p towards the trailing edge. Figure 7.17 shows a representation of the

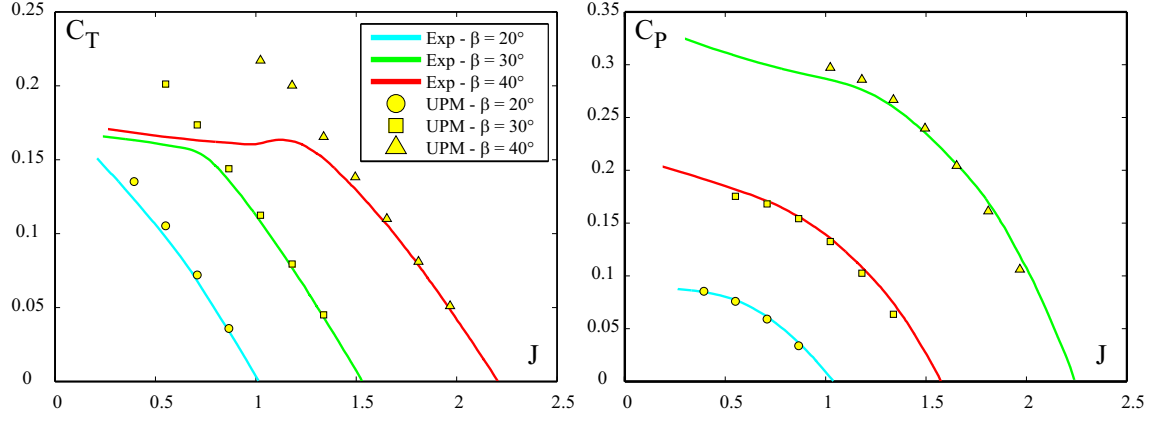


Figure 7.13: Comparison between experimental data from [7] and numerical results. Figure on the left shows the thrust coefficient C_T for different values of the advance ratio J , while figure on the right shows the Power coefficient C_P versus J . The simulations are repeated for three different values of the blade angle β , defined as the angle between the chord of a reference blade section and the propeller's plane of rotation.

developed wake in the numerical simulation. An important issue concerns the stability of the wake. Some authors have noticed that with an impulsive start of the rotor, some instabilities arise and no convergence is reached in the solution [10]. In the case of the simulations performed with the present capability, even with a slow start some instabilities have been observed: the wake in the center of the rotor is first convected upstream and eventually will be convected downstream after several revolutions. The effects of this on the final results are not yet known. Another form of instability, typical of helicopter rotors, concerns the pairing of the tip vortices as they are convected downstream. If a time marching Euler scheme is employed to simulate helicopter blades or rotors operating at hovering conditions, in order to avoid such instabilities a reduced timestep is needed. This has an impact on the cost of the simulation. For this reason implicit time-marching algorithms have to be preferred, as they are more stable and prevent wake instabilities even with smaller timesteps. For extensive details the reader is referred to works [2, 20–22]. As time-marching schemes are beyond the aims of this work, it can be said that even though much more work could be done to improve the capabilities of the code for the study of helicopter wakes, from the results of the Caradonna test, for what concerns the testing of the BEM formulation for vortex impingement, the code can be considered as validated. In fact, no instabilities due to vortex impingement have been noticed and the results show good agreements with the experiments.

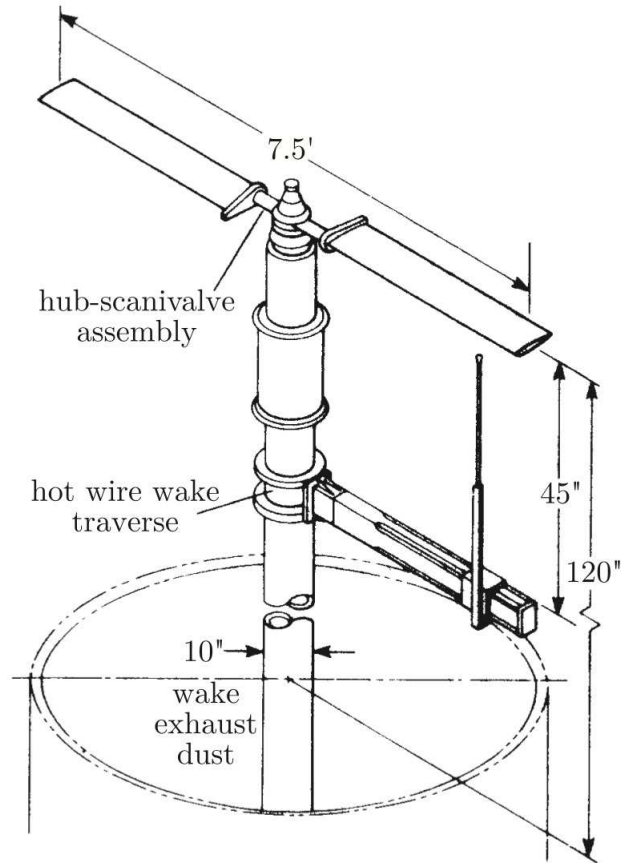


Figure 7.14: Details of the Caradonna-Tung experiment. Wind tunnel set-up. From [9].

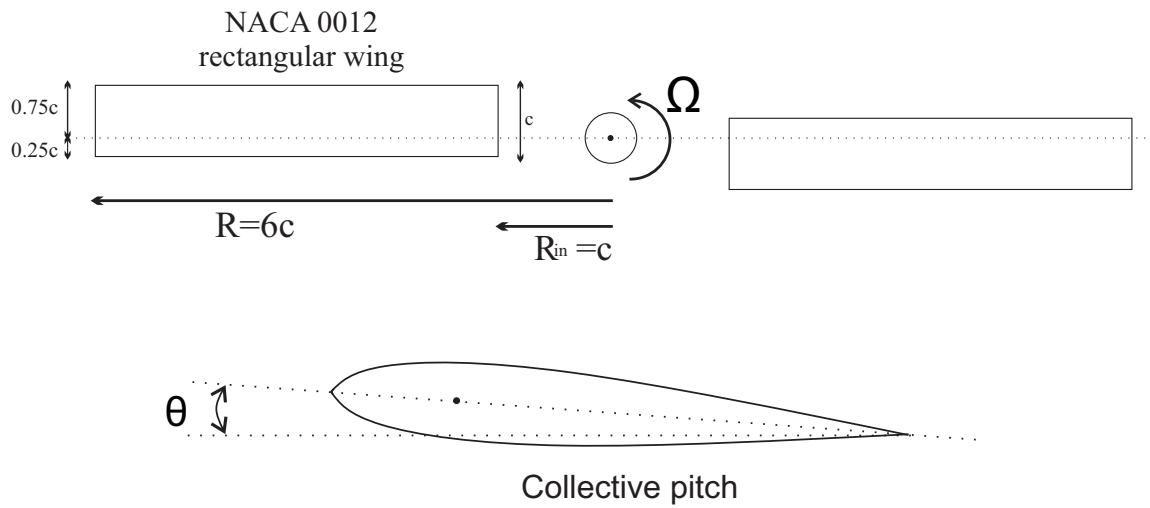


Figure 7.15: Rotor blade dimensions in multiples of the chord c and definition of collective pitch θ .

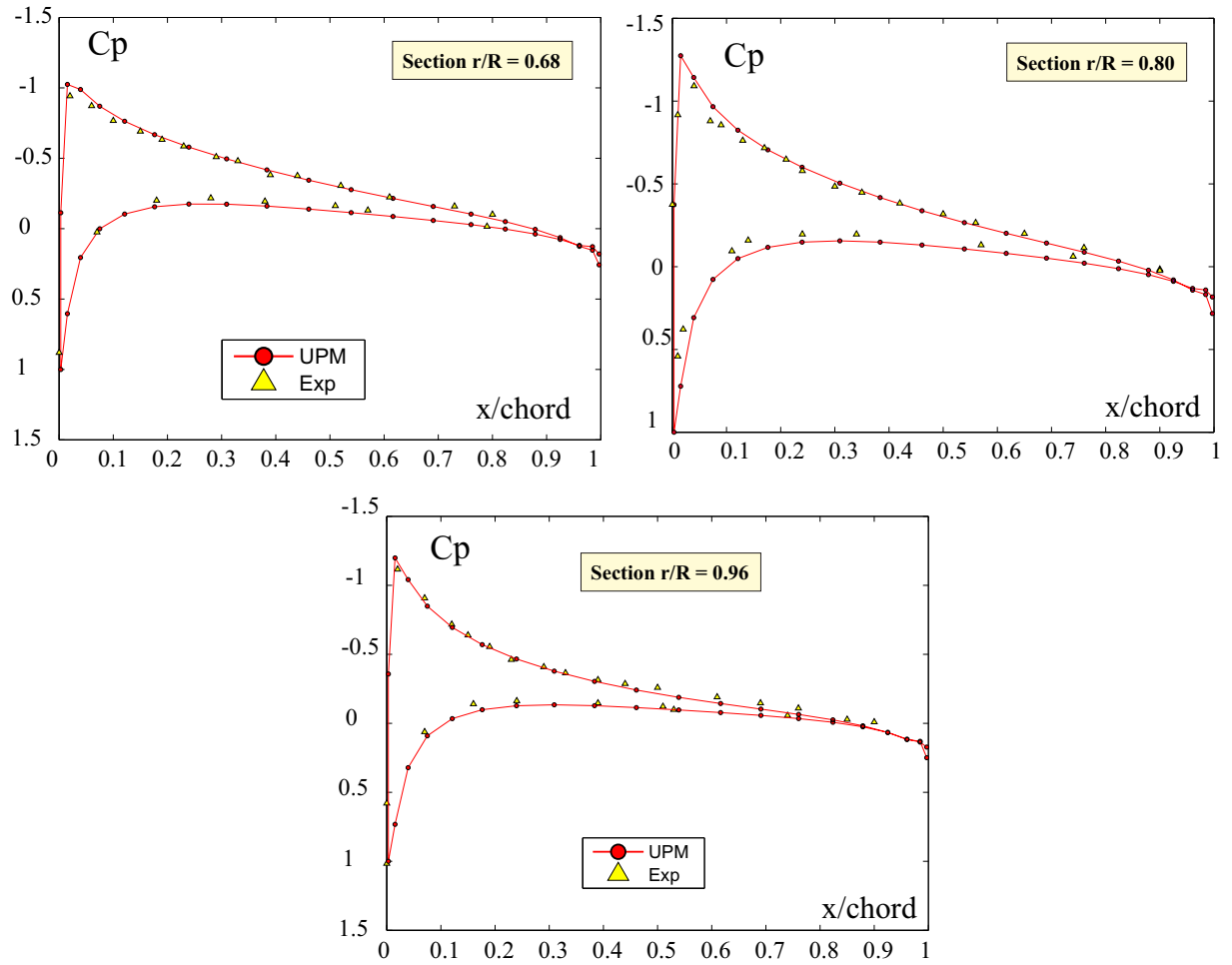


Figure 7.16: Comparison between experimental data and numerical results for three different spanwise sections.

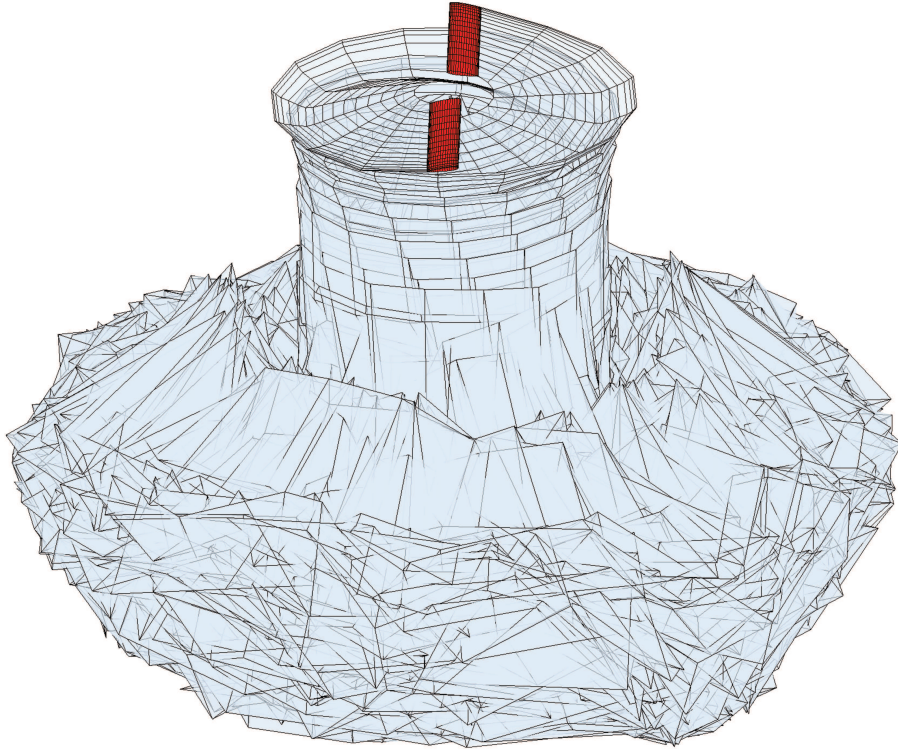


Figure 7.17: Developed wake of the Caradonna-Tung simulation.

Part II

APPLICATIONS: *IDINTOS*

PROJECT

Chapter 8

Introduction

IDINTOS is a project funded by the Tuscany regional government of a two-seater Ultralight PrandtlPlane joined wing amphibious aircraft. The project leader is prof. Frediani of the Aerospace Engineering department of University of Pisa. His group, with the support of external groups, was performing the design and coordinateing all the other technical activities. The project led to a realization of a prototype of the aircraft that was officially presented in November 2013 in Pontedera (Italy) and in April 2014 at the Aeroexpo in Friedrichshafen (Germany). Different studies on *IDINTOS* are currently in progress and work still has to be done to advance from a prototype to a fully flying configuration.

Because of the *innovative flavour* of the project (*IDINTOS* is one of the few examples of *full-scale* joined wings prototypes ever realized), the conceptual design of this configuration required a large effort. A key-role was played by the know-how gained by years of experience in the topic.

The first stages of the conceptual design were carried out using low fidelity tools and after a process of optimization, more refined capabilities like CFD and wind tunnel tests were employed for a fine tuning of the configuration. *IDINTOS*' propulsion system is composed of two three-bladed ducted propellers, whose design has been conducted simultaneously with the design of the aircraft. The propellers have been designed and optimized using lower order methods based on the actuator disk model and the blade element theory (BET).

A fundamental issue is to understand how the propellers influence the aero-mechanics of the whole aircraft, especially from the point of view of the aircraft trim and stability. First steps in this direction were made through CFD simulations; however because of the high computational efforts required to model the flow around a complete aircraft with the addition of a rotating propeller, their effects were simulated with a simplified model based on

a pressure jump boundary condition in proximity of the propellers' ducts. This model does not take into account the swirl perturbation velocities generated by the propeller blades, as well as the wake evolution and its effect on the aircraft. The need of more reliable results with limited computational costs made panel methods a good option for the study of the propellers influence on the aircraft.

Chapter 9

IDINTOS: Propeller

After the development and validation of the panel code, the second part of this work is based on its applications. Practical problems, like propeller performances and its integration in the aerodynamics design of an amphibious PrandtlPlane joined wing configuration are investigated. In this chapter the propeller is tested, simulating a series of operative conditions to obtain the performance curves.

9.1 Geometry and mesh

The three-blade ducted single propeller designed for the propulsion of an innovative two-propeller sea-plane (IDINTOS) is shown in Figure 9.1. The propeller was designed using a code based on the two-dimensional blade element theory (BET) and is the result of a process of optimization specifically focused on the cruise and take-off requirements [25]. Table 9.1 summarizes the parameters of the simulations. J is called *advance ratio* and is defined as:

$$J = \frac{V_{\infty}}{nD} \quad (9.1)$$

where V_{∞} is the wind speed, D is the propeller diameter and n the propeller's rotational velocity expressed in *revolutions per second*. The blade angle β is defined as the geometrical angle between the chord of a blade section taken as reference and a plane normal to the propeller's rotation axis.

Figure 9.2 shows the surface mesh for a single blade: it is composed of 23 and 32 panels in the spanwise and chordwise directions. The mesh is equally distributed between the upper and lower surface, with a refinement towards the leading and the trailing edge. The propeller shaft and the shroud have not been modeled.



Figure 9.1: 3D render of the amphibious Joined Wing IDINTOS with the two ducted propellers.

	RPM	V_{∞} [$\frac{m}{s}$]	Altitude [m]	Air density [$\frac{Kg}{m^3}$]	Blade angle [deg]	J
1	3485	22	0	1.225	0	0.0718
2	3305	22	0	1.225	0	0.0757
3	3004	22	0	1.225	0	0.0833
4	2884	22	0	1.225	0	0.867
5	2584	22	0	1.225	0	0.968
6	3485	55	1000	1.112	10	0.1794
7	3305	55	1000	1.112	10	0.1892
8	3004	55	1000	1.112	10	0.2081
9	2884	55	1000	1.112	10	0.2168
10	2584	55	1000	1.112	10	0.2420

Table 9.1: Simulations' matrix.

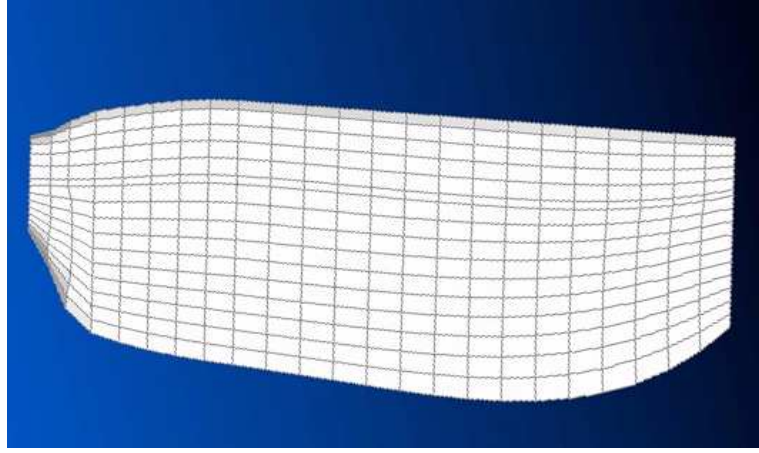


Figure 9.2: Mesh of the upper surface of a single blade of the propeller.

Figure 9.3 shows the performance curves in terms of thrust (c_T) power coefficient (c_P) (for the respective definitions see Section 7.3) of the propeller obtained with the BET and with the present panel code (UPM).

9.2 Comparison between panel code and BET

Figure 9.4 represents a direct comparison between the results obtained with the panel code and the BET in terms of percent error (for a definition of percent error see Appendix D). Because of the substantial differences, further investigations were carried out to find the causes of the discrepancy.

Results comparison of BET and panel method on Bierman and Gray 1942 NACA Report test case First of all, both methods have been validated with the same testcase presented in Section 7.3; Figure 9.5 shows a comparison between the results.

For high advance ratios, the two methods give good results compared to the experimental data. As the advance ratio decreases, the panel code results start to differ more from the experimental values by a larger extent than BET does. This is probably consequence of the fact that for low advance ratios the effects related to the boundary layer on the propeller aerodynamics become not negligible; in some sections closer to the root of the blades the flow can even be separated. Because the BET takes into account the effects of the boundary layer, the results obtained with this method are closer to the experimental values, while the panel code does not consider the boundary layer, consequently, in case of flow separation,

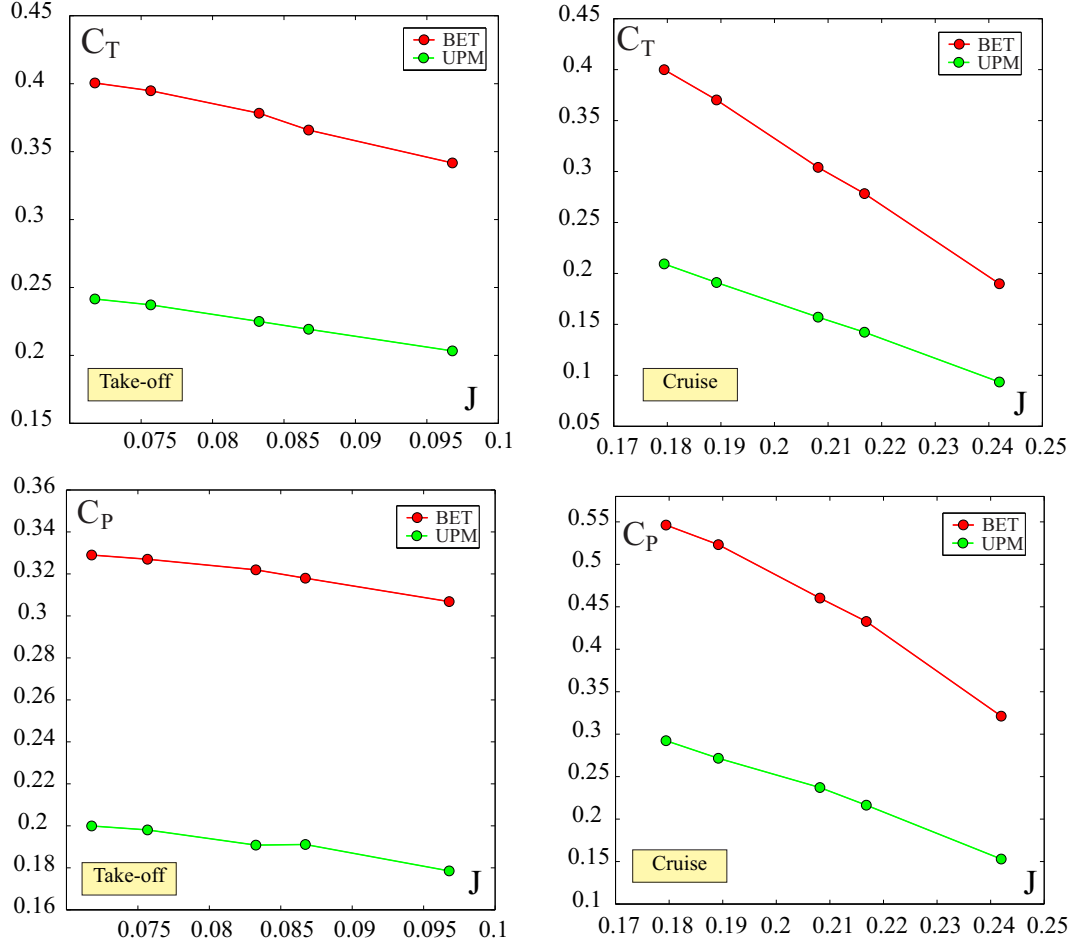


Figure 9.3: Comparison between the results obtained with the BET and the present panel code UPM in terms of thrust coefficient c_T and power coefficient c_P for the operative conditions listed in Table 9.1.

the numerical model is not a good representation of the physics of the experiment.

Panel code and BET performances on IDINTOS propeller: further investigations In the case of the IDINTOS propeller, an analysis of the spanwise distribution of the geometric angles of attack along the blades suggests that separation phenomena do not occur. Thus the large discrepancy between the results of the two methods can't be attributed to the boundary layers effects.

While the panel code considers the three-dimensional propeller geometry without any a priori assumption about the flow behaviour along the spanwise direction of the blades, the BET is based on a two-dimensional strip theory: this means that every section of the blade

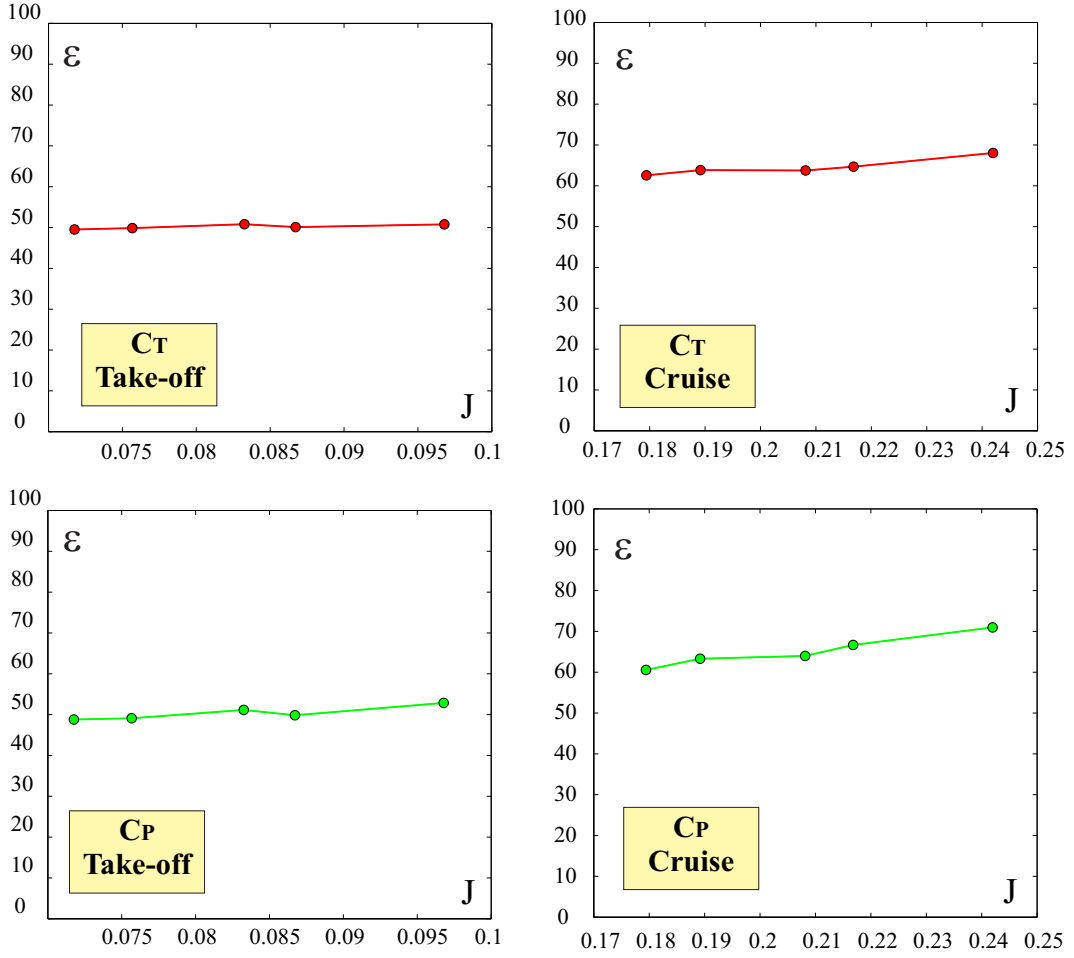


Figure 9.4: Differences between the results obtained with BET and the results from the present code in terms of percent error.

is considered as a stand-alone two-dimensional airfoil, not influenced by the aerodynamics of the neighbor blade sections. With this hypothesis, the three-dimensional effects related to the finiteness of the blades, such as tip-losses and tip-vortices are not captured. To take into account the tip-losses, the forces are integrated along the spanwise direction until the 97% of the tip-radius. While the two-dimensional strip theory can be a good approximation for high aspect ratio wings or blades (such as helicopter blades), its implications on low aspect ratio blades like the blades of the IDINTOS propeller have to be discussed. Considering the area S_{ref} of the upper surface highlighted in Figure 9.6 and the propeller radius $\frac{D}{2}$, the blade aspect ratio is

$$AR = \frac{\left(\frac{D}{2}\right)^2}{S_{ref}} = 4.3. \quad (9.2)$$

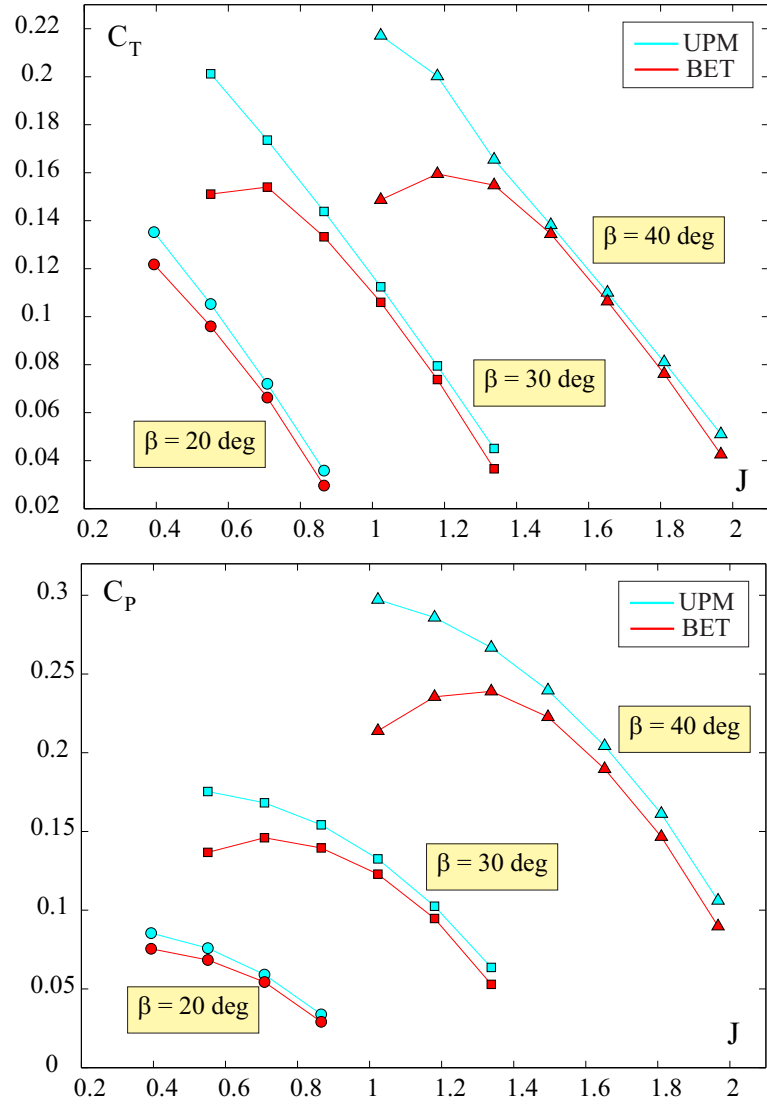


Figure 9.5: Comparison between BET and UPM for the testcase of Bierman and Gray 1942 NACA Report [7].

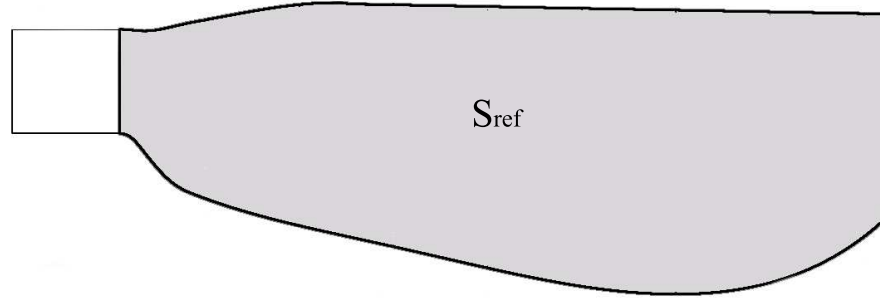


Figure 9.6: Blade planform. The surface colored in grey has been taken as reference for the evaluation of the blade aspect ratio.

AR	2.84	4.3	6.5	8.6	13	17.3	21.7
Scale factor	1.5	1	0.66	0.5	0.33	0.25	0.2

Table 9.2: Scale factors and aspect ratios of the different blades tested.

A campaign of simulations was made to evaluate the effects of the aspect ratio on the comparison between the results of panel code and BET. Keeping the blade radius constant, the blade geometry was scaled, resulting in a variation of the aspect ratio. As the aim of the simulation was to evaluate if the discrepancies between the two methods were somehow related to the finiteness of the blade and to the tip-losses, the propeller was modeled with just one blade. The aspect ratio of the original propeller was taken as reference (AR_{ref}); Table 9.2 shows the scale factors (defined as AR/AR_{ref}) and the aspect ratios. Table 9.3 reports the parameters of the operative condition (cruise) chosen for the simulation. Figure 9.7 shows the planform of the different aspect ratio blades. A comparison between the results of the two methods is represented in Figure 9.8 in terms of percent error. It is possible to see that increasing the aspect ratio, the differences between the two methods decrease. Although this cannot be considered as a definitive proof and further investigations beyond the purposes of this work have to be carried out, it is possible to say that without any doubt the three-dimensional effects due to the finiteness of the blade play an important role in the propeller aerodynamics and cannot be neglected a priori.

RPM	V_∞ [$\frac{m}{s}$]	Altitude [m]	Air density [$\frac{Kg}{m^3}$]	Blade angle [deg]	J
3004	55	1000	1.112	10	0.2081

Table 9.3: Operative condition for the simulations with different values of AR.

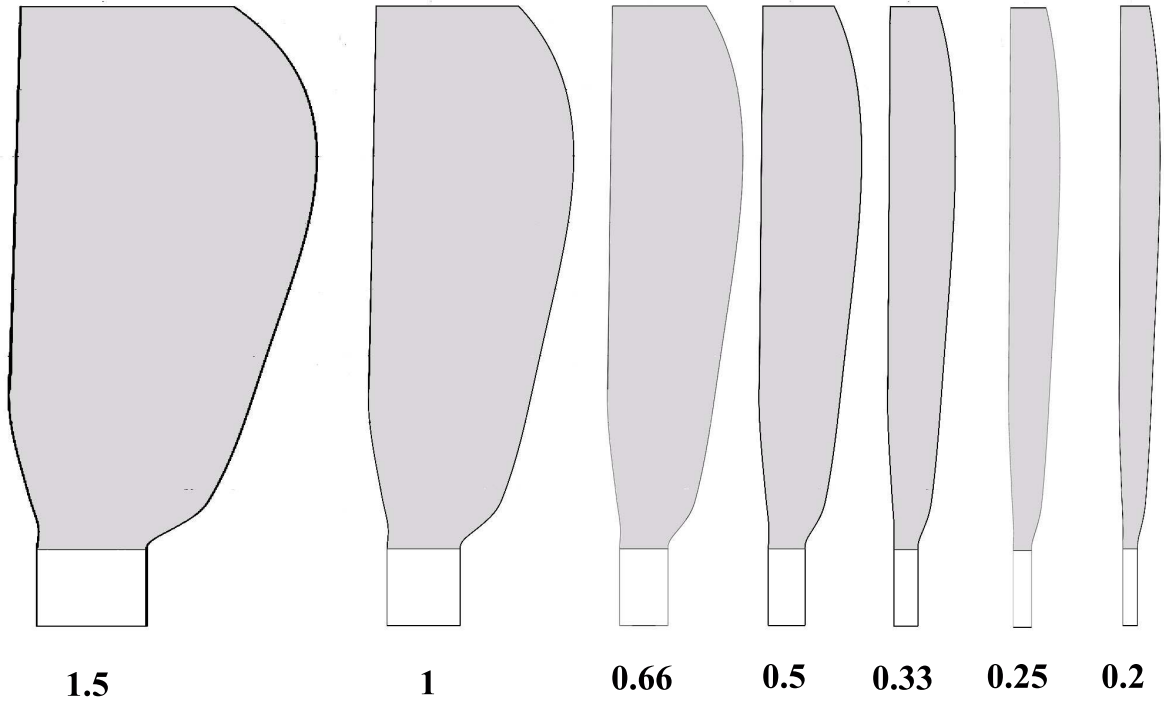


Figure 9.7: Blade planforms for different aspect ratios. Every blade has been scaled in a plane perpendicular to the blade radius, which is the same for every model. The number next to each blade represents the *scale factor*.

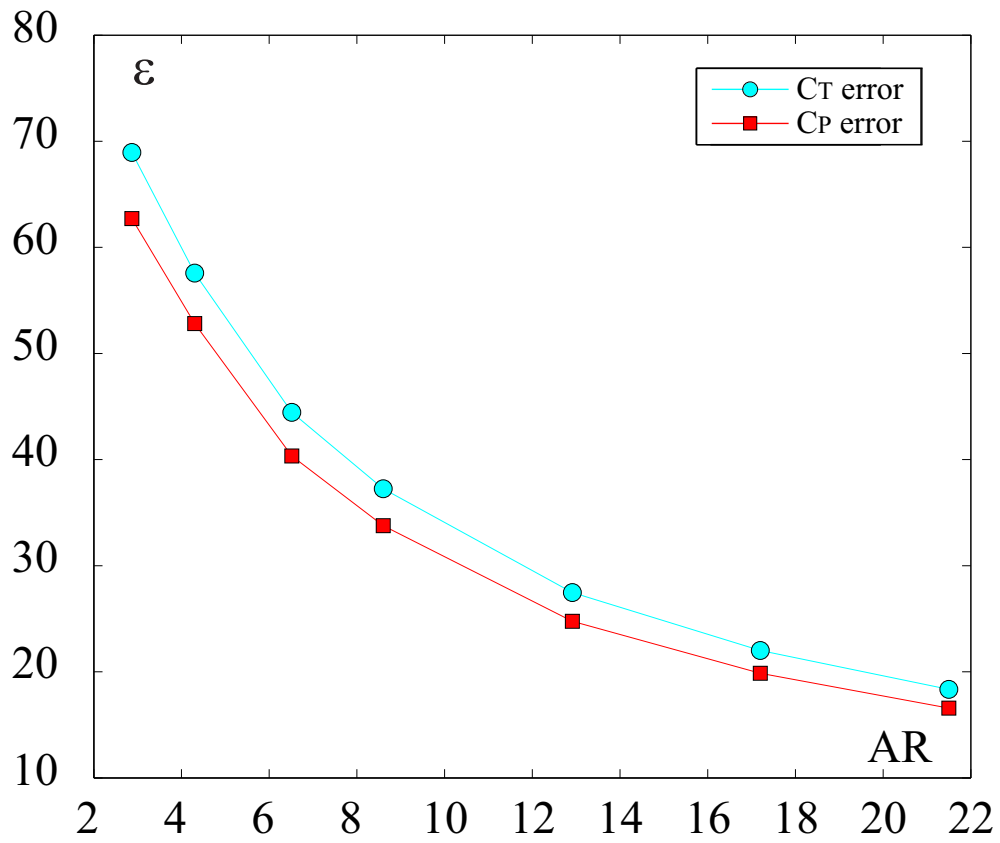


Figure 9.8: Percentage errors between the results of BET and UPM in terms of thrust and power coefficients for different aspect ratios. As expected, the error decreases as the aspect ratio increases.

Chapter 10

IDINTOS: Aircraft Models and Propellers Integration

10.1 Introduction

In this chapter the code will be applied to the study of a Joined Wing PrandtlPlane aircraft, focusing on the problem of the effects of the integration of the propellers in the configuration. A description of the different models tested will be presented, followed by a comparison of the results obtained and a discussion on the consequences of the model choice.

10.2 Description of the analyzed joined-wing configurations

From the prototype CAD model (Figure 10.1), four different configurations were considered.

The first one, called *wingsystem*, includes only the wing system; fuselage and fin are excluded from the model. The aerodynamic surface has been cleaned out, removing the tip hulls and the fences: their effects on the aircraft's aero-mechanics are considered to be second order and will not be taken into account in this work. Removing the fuselage from the model creates a gap in the front wing: this gap has been filled extending the front wing root sections in the directions perpendicular to the aircraft's longitudinal plane. The wing surface mesh is composed by 50 panels in the chordwise direction (25 on the upper surface and 25 on the lower one) and the spanwise panels distribution is refined towards the wing tips. Figure 10.2 shows a representation of the model.

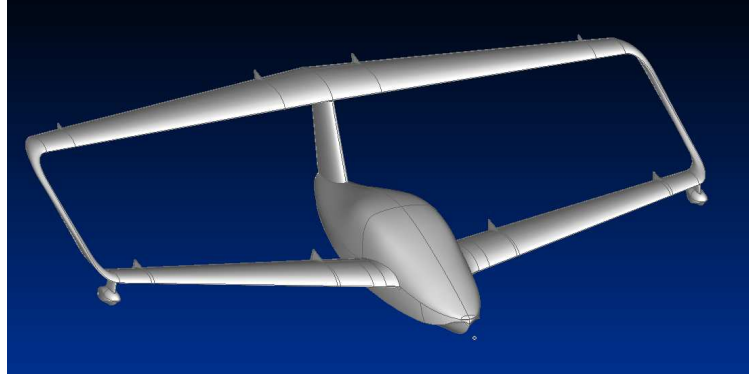


Figure 10.1: CAD model of the *IDINTOS* external surface.

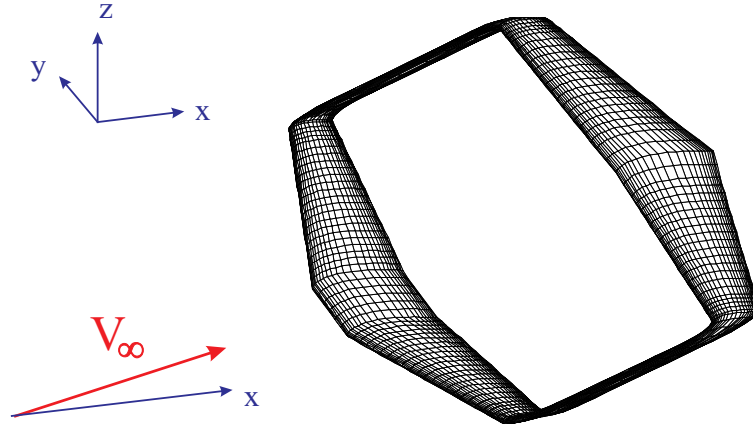


Figure 10.2: Aerodynamic model of the wing system (*wingsystem*).

The second configuration includes the propellers, whose geometry and model have been introduced in Section 9.1. The configuration wing system and propeller is called *wingprop* and is represented in Figure 10.3. In this case too, the shaft and the shroud are not taken into account.

The third configuration, called *wingbody* and represented in Figure 10.4, includes the wing system, the fuselage and the fin. Again the surfaces have been cleaned out of the fences and the tip hulls. The fuselage bottom hull has been smoothed in those areas presenting a sharp step, preventing inaccurate results due to the inability of panel methods to represent situations with boundary layer separations. The fourth configuration adds the propellers to the *wingbody* model and will be called *complete*. Figure 10.5 shows this configuration.

All the simulations were performed at cruise conditions, with a speed $V_{cr} = 49 \text{ m/s}$, an angle of attack $\alpha_{cr} = 1^\circ$ and an altitude of $h_{cr} = 1000 \text{ m}$ (it sets the air density). To

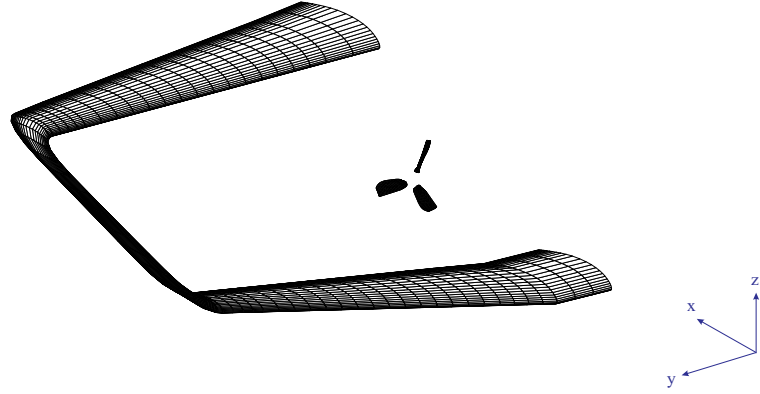


Figure 10.3: Aerodynamic model of the wing system and propeller (*wingprop*). Only one half of the model is shown (the configuration is symmetric with respect of xz -plane).

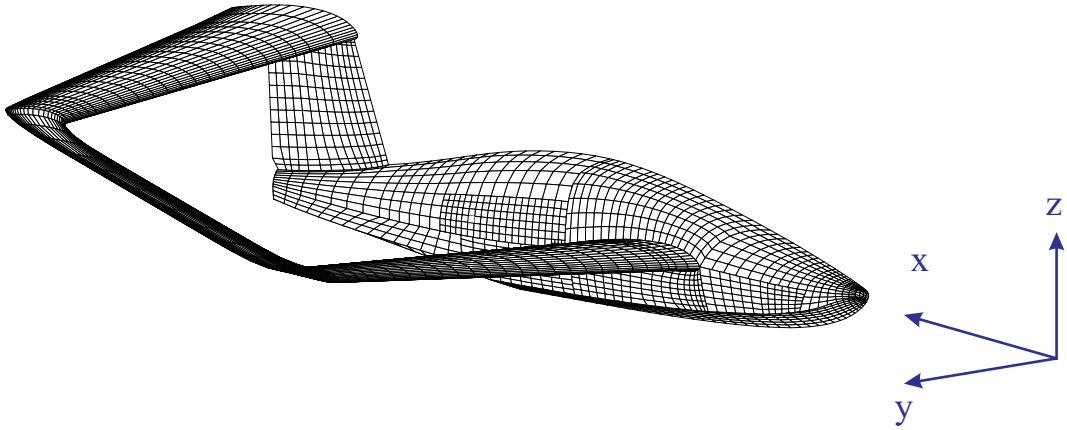


Figure 10.4: Aerodynamic model of the fuselage, wing system vertical fin (referred to as *wingbody*). Only one half of the model is shown (the configuration is symmetric with respect of xz -plane).

evaluate the aerodynamic derivatives in the longitudinal plane, a numerical differentiation was carried out, based on an angle of attack increment of 0.1° . Forces and moments have been non-dimensionalized with the reference surface S_{ref} and the mean aerodynamic chord c_{ref} .

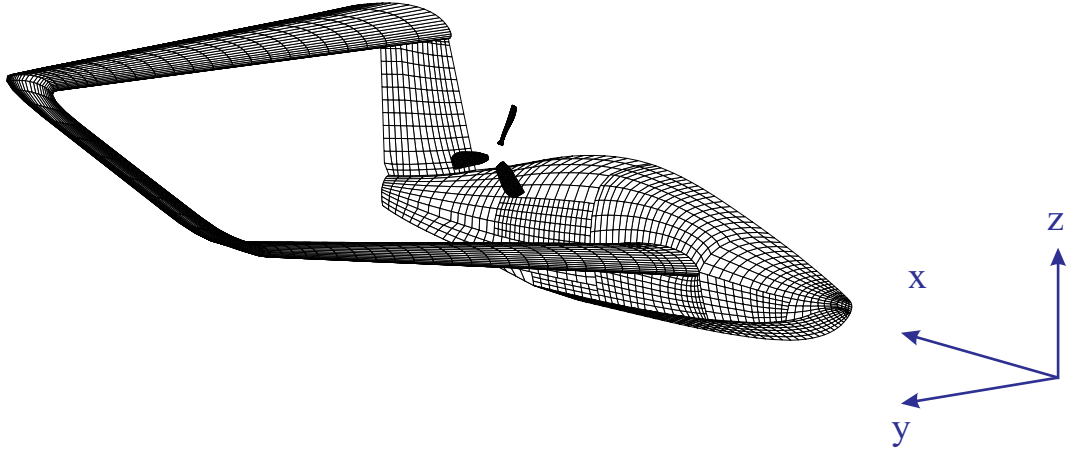


Figure 10.5: Aerodynamic model of the fuselage, wing system and propeller (referred to as *complete*). Only one half of the model is shown (the configuration is symmetric with respect of xz -plane).

10.3 Modeling options for the wing system and propeller's influence

A first set of simulations has been carried out on the *wingsystem* and *wingprop* configurations. Different modeling approaches have been used; they will be compared and discussed, trying to understand how they affect the numerical results.

The results are shown in Table 10.1.

10.3.1 Rigid/Free Wake modeling effects

With the rigid wake modeling, the wake shed from the trailing edge is forced to be parallel to the *free-stream* velocity. The free wake modeling better represents the physics of a *real* flow because it takes into account also the perturbation velocity induced by the body and the wake: thus, the wake is forced to be parallel to the *total* velocity. While the free wake is a more accurate modeling option, on the other side it requires more computational efforts, so it is reasonable to discuss how much the wake model influences the results of the simulation.

For a conventional wing, the differences in terms of lift coefficients between the two models are usually negligible (see Figure 7.4 in Section 7.1). For a PrandtlPlane configuration this is not true a priori; because of the presence of two large wings and because of the presence of the lateral joints, the wake shape can have a stronger impact on the global forces.

Simulation	C_L	C_D	C_{M_q}
<i>Wingsystem</i> -IKC-Free	3,05E-01	7,06E-03	-2,01E-02
<i>Wingsystem</i> -LKC-Free	3,18E-01	7,47E-03	-3,28E-02
<i>Wingsystem</i> -IKC-Rigid	3,07E-01	7,15E-03	-2,37E-02
<i>Wingsystem</i> -LKC-Rigid	3,20E-01	7,56E-03	-3,62E-02
<i>Wingprop</i> -IKC-Free	3,04E-01	7,17E-03	1,20E-03
<i>Wingprop</i> -LKC-Free	3,17E-01	7,58E-03	-8,10E-03
<i>Wingprop</i> -IKC-Rigid	3,10E-01	7,28E-03	-1,01E-02
<i>Wingprop</i> -LKC-Rigid	3,23E-01	7,70E-03	-2,05E-02

Table 10.1: Steady lift, drag and pitching moment coefficients for nominal cruise condition and different modeling approaches (LKC and IKC refer to the regular and iterative Kutta condition, Rigid/Free indicate the adopted wake modeling).

From the results of Table 10.1, the differences in terms of lift and drag coefficients for the *wingsystem* between rigid and free wake are not relevant (less than 0.5%). This means the influence of the wake shape on the global lift and drag is very small. Observing the pitching moment, the differences become relevant (between 10% and 20%). Figure 10.6 shows the distribution of normalized sectional lift $C_l \cdot c$ (where c is the sectional chord) and lift coefficient C_l for the *wingsystem* configuration. The sectional lift distribution of the front wing is basically not altered by the choice of the wake model. On the other hand, the rear wing experiences a change in sectional lift due to the wake shape: the differences between the two models are more relevant at the wing tip, while they become negligible approaching the wing root sections. Figure 10.7) compares the wake shape in case of free and rigid wake: the main differences are in proximity of the wing tips, due to the presence of the tip vortices, that are represented only in the free wake case because they are a consequence of the perturbation velocities related to the finiteness of the wings.

Although the differences in the sectional lift between the two cases have slight effect on the global lift, they have a not negligible effect on the pitching moment; this is consequence of the aircraft's center of gravity position, just behind the front wing, resulting in a longer moment arm for the forces that act on the rear wing.

Analyzing the configuration *wingprop*, the different wake models give similar results to what observed for the *wingsystem*. Again, the differences in terms of lift and drag are small compared to the differences in pitching moment.

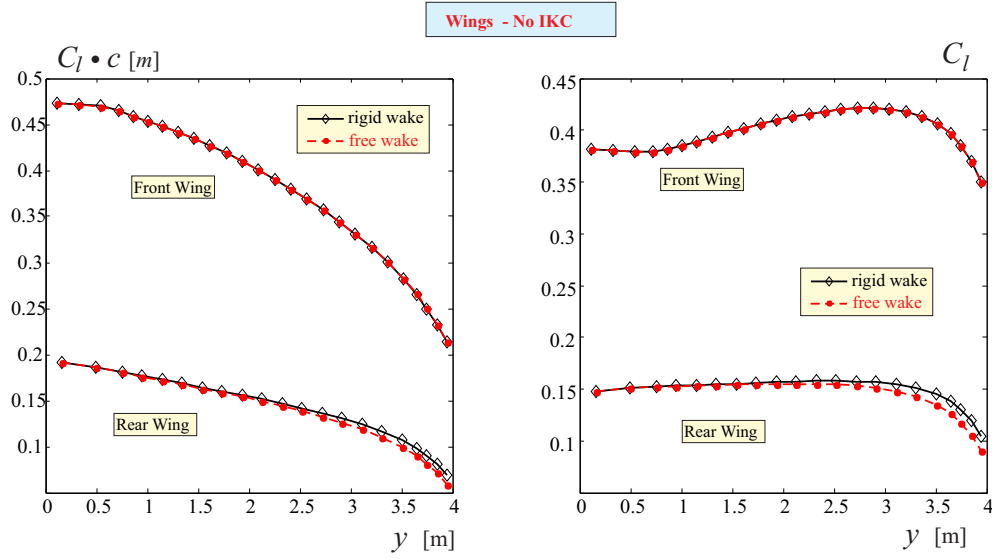


Figure 10.6: Sectional semi-normalized lift ($C_l \cdot c$) and lift coefficient (C_l) along the wing span for the *wingstem* case. The regular (linear) Kutta condition is enforced.

A correct representation of the wake is extremely important especially for the propeller, where the effect of the tip-vortices on the aerodynamic forces of each blade can be relevant. In this simulations the forces on the propellers are not taken into account, however the propellers wake, convected by the free-stream velocity, passes close to the rear wing, modifying the pressure field all around. Using a rigid wake or a free-wake model, thus, influences the aerodynamics of the whole configuration.

Comparing the sectional lift distributions (Figure 10.8) between rigid wake and free wake for the *wingprop*, it is possible to observe that in this case the differences are not limited to the rear wing tips. While the lift on the front wake is barely affected by the wake shape, the rear wing experiences the influence of the propeller's wake, whose shape has a great dependence on the wake model. In the free wake case the lift reduction is probably a consequence of the tendency of the wake to enlarge its helix radius while convected downstream; passing closer to the rear wake, its influence is higher than the rigid wake case. Figure 10.9 shows the wake shape for the *wingprop* depending on the wake model.

For the *wingprop* configuration too, the lift redistribution on the rear wing causes a change in the pitching moment that cannot be neglected. While small changes in the aircraft trim can be easily corrected with small deflections of the control, it is important to evaluate the effect of the lift redistribution due to the different models on the longitudinal flight

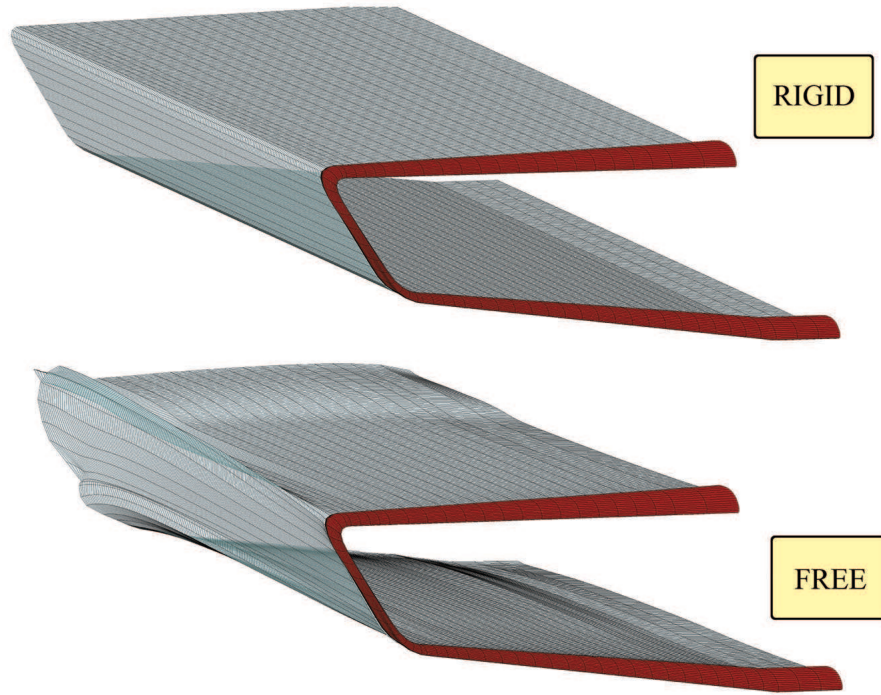


Figure 10.7: Comparison in terms of wake shape between rigid model and wake model for the *wingsystem*. The main differences are concentrated near the wing tips, where it is possible to observe the roll-up vortices in the free wake case.

mechanics. One important parameter in this regard is the static margin of stability (the ratio between pitching moment slope and lift slope coefficients normalized with the mean aerodynamic chord, i.e. $C_{M_q\alpha}/C_{L\alpha} \cdot c_{mean}$). Table 10.2 shows the margin of stability for *wingsystem* and *wingprop* depending on the different models. For both configurations it can be noticed a decrease on the margin of stability when the free wake model is used.

10.3.2 Iterative Kutta condition

In Section 2.7 the Joukowski condition was introduced to remove the velocity singularity on the trailing edge and consequently determine the near wake panels intensities. While in a two-dimensional domain this is enough to ensure zero pressure jump across the trailing edge (Kutta condition), in a low order three-dimensional domain this is not true a priori. For this reason, the Kutta condition has to be enforced through an iterative procedure, introduced in Section 3.7.

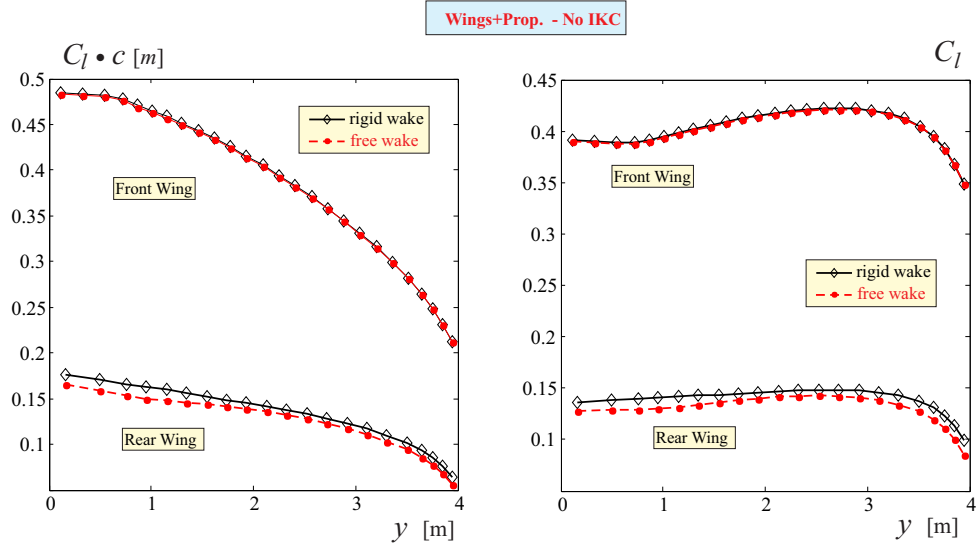


Figure 10.8: Sectional semi-normalized lift ($C_l \cdot c$) and lift coefficient (C_l) along the wing span for the *wingprop* case. The regular (linear) Kutta condition is enforced.

Simulation	$-\frac{C_{M\alpha}}{c_{\text{mean}} \cdot C_{L\alpha}}$ (%)
<i>Wingsystem</i> -IKC-Free	16,60 %
<i>Wingsystem</i> -LKC-Free	18,95 %
<i>Wingsystem</i> -IKC-Rigid	18,95 %
<i>Wingsystem</i> -LKC-Rigid	20,34 %
<i>Wingprop</i> -IKC-Free	17,11%
<i>Wingprop</i> -LKC-Free	18,44%
<i>Wingprop</i> -IKC-Rigid	17,23%
<i>Wingprop</i> -LKC-Rigid	18,90%

Table 10.2: Static margin of longitudinal stability at nominal cruise condition and different modeling approaches (LKC and IKC refer to the regular and iterative Kutta condition, Rigid/Free indicate the adopted wake modeling).

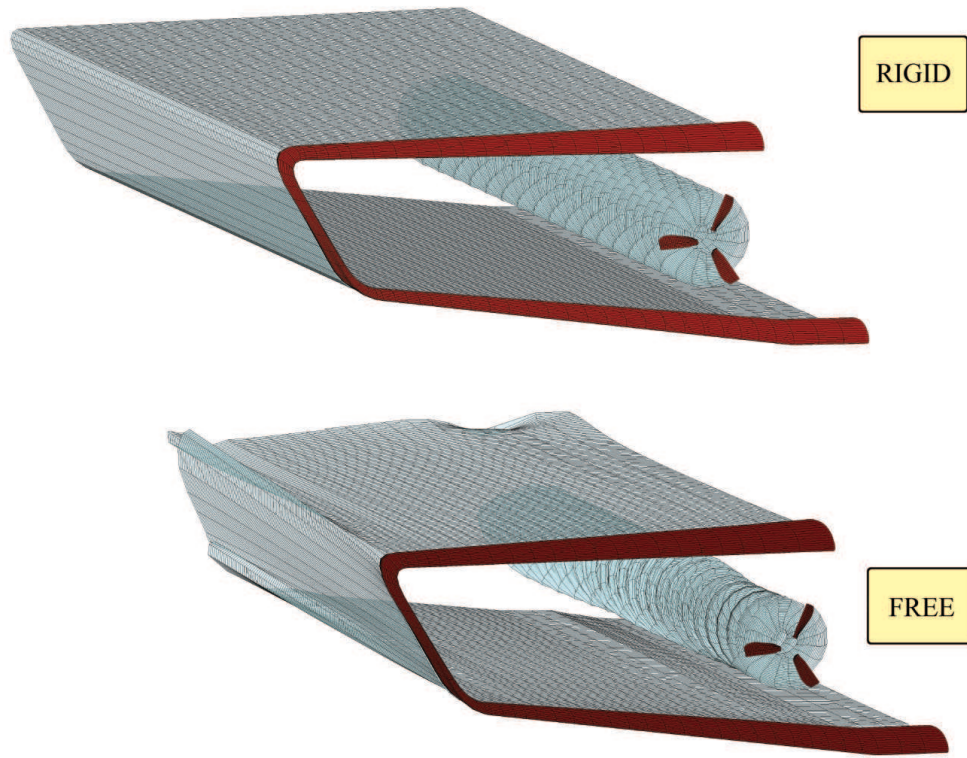


Figure 10.9: Comparison in terms of wake shape between rigid model and wake model for the *wingprop*. The main differences are in the propeller's wake; in the free wake model, it is possible to notice how the roll-up vortices grow as they are convected downstream.

From the results listed in Table 10.1, considering the *wingsystem* configuration the iterative Kutta condition case presents a reduction of lift coefficient of 5% compared with the respective case with the linear Kutta condition. In Figure 10.10 the spanwise distributions of C_l and $C_l \cdot c$ are compared. The differences in the two lift distribution can be observed on both wings: all over the wing span the iterative Kutta condition case presents a lower sectional lift. This is more evident on the rear wing, but it can be appreciated on the front wing too. To understand the causes of this lift reduction, it can be convenient to plot the chordwise pressure coefficient distribution of a wing section. The iterative Kutta condition enforcement drives the pressure jump on the trailing edge to zero, as shown in Figure 10.11; at the same time, it causes a redistribution of the pressure coefficients all along the wing chord, with larger differences towards the trailing edge. the result is a small sectional lift in the case of the iterative Kutta condition. Consequence of this redistribution is a varia-

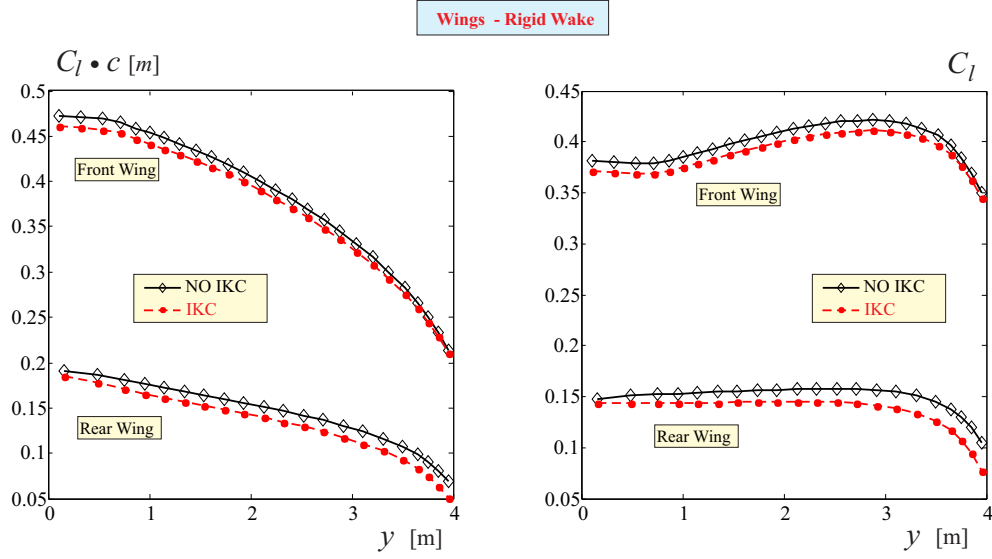


Figure 10.10: Sectional semi-normalized lift ($C_l \cdot c$) and lift coefficients (C_l) along the wing span for the *only wing* case. Rigid wake is considered. Enforcement of classic and iterative Kutta condition results are compared.

tion of the pitching moment (lower nose-down pitching moment) coefficient compared to the linear Kutta case and, most important, a reduction of the margin of stability, as shown in Table 10.2. Using lower order methods (linear Kutta, rigid wake) does not give conservative predictions: higher lift, higher nose-down pitching moment and higher margin of stability.

Adding the propeller does not change the trend of the results observed for the wing system only for what concerns the effects of the iterative Kutta condition.

10.3.3 Propeller's wake influence on the wing system aerodynamics

Comparing the *wingsystem* simulations in terms of lift coefficient with the respective cases with propeller, it can be noticed that the differences are very small, independently from the wake model or the Kutta condition. On the contrary the effects on the pitching moments are not negligible. Figure 10.12 shows the comparison between *wingsystem* and *wingprop* configurations in terms of sectional lift distribution and C_l distribution. Both simulations involves the iterative Kutta condition and the free wake model. The propeller's influence causes a lift increase in the front wing, accelerating the flow on the upper surface and

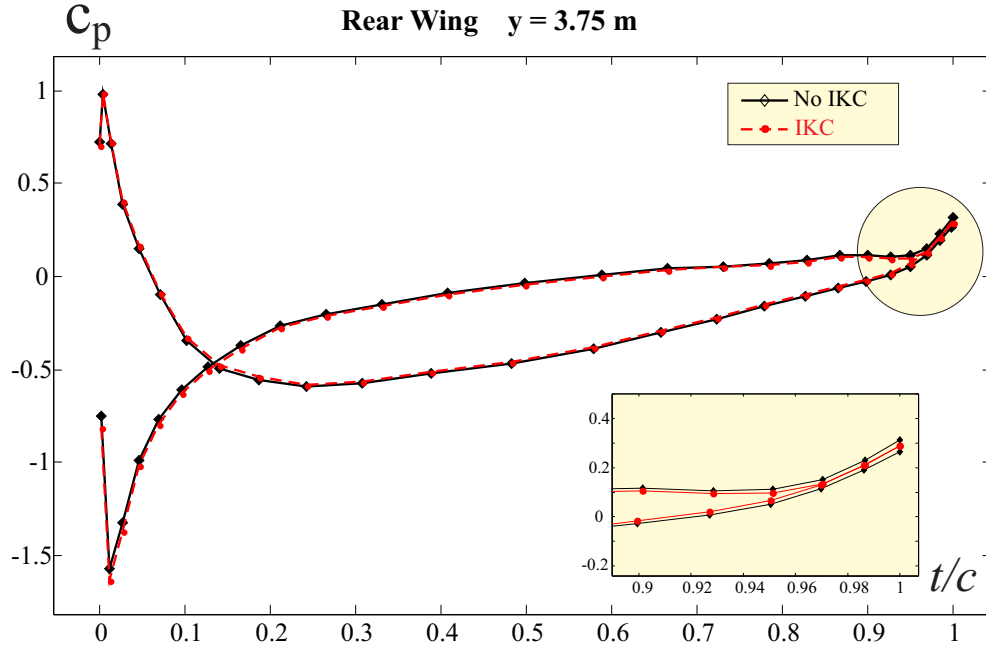


Figure 10.11: Pressure coefficient (c_p) distribution at rear wing section $y = 3.75 m(15/16 b)$. *Wingsystem* case. Linear and Iterative Kutta condition modeling results are compared.

consequently creating a suction region whose effects decrease moving towards the wing tip, which means far from the propeller. At the same time, the propeller's wake convected downstream passes under the rear wing; the velocities induced by the vortices affects the aerodynamics and modify the pressure field, causing a reduction in sectional lift in those sections closer to the propeller's wake. Moving towards the wing tips, the influence of the propellers tends to become negligible. While the effects of the increasing lift on the front wing and of the lift deficiency on the rear wing compensate for what concerns the total lift, this does not happens for the pitching moments. In fact the two effects generates a nose-up contribute that reduces the total nose-down pitching moment.

Observing the chordwise pressure coefficient distribution (Figure 10.13) for two sections on the front wing and two sections on the rear wake, it is interesting to see how the pressure redistribution is more evident on the upper surface for the front wing and on the lower surface for the rear wing, as expected. The sections closer to the wing tip are less affected by this redistribution.

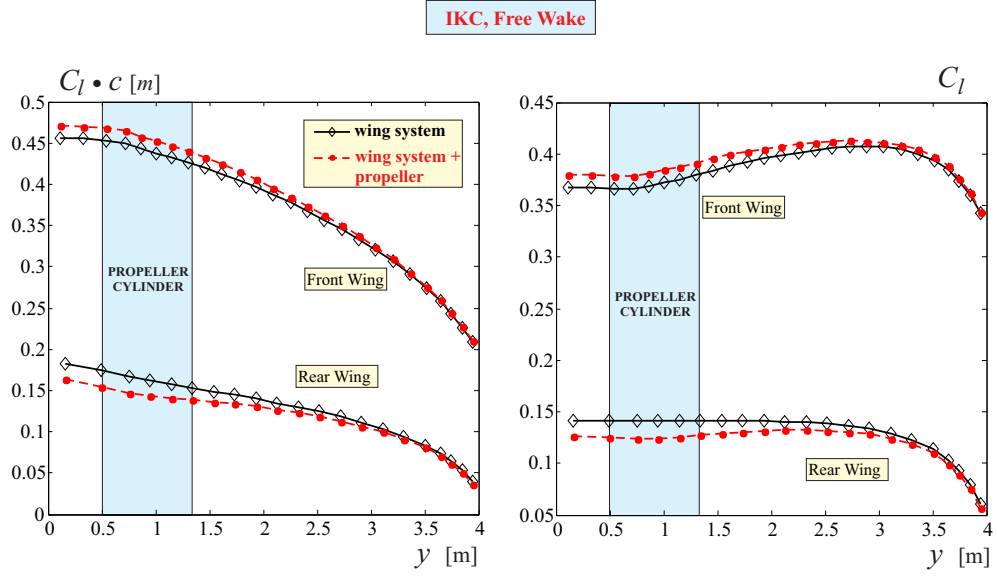


Figure 10.12: Sectional semi-normalized lift ($C_l \cdot c$) and lift coefficients (C_l) along the wing span for the wings only *wingsystem* and the wings with the propeller *wingprop* cases. Free wake and iterative Kutta condition enforcement are considered.

Concerning the longitudinal aero-mechanics, the loads redistribution due to the propeller affects the margin of stability, as results from Table 10.2. In all cases the margin of stability is reduced respect to the correspondent *wingsystem* configuration, except for the case of free wake and iterative Kutta condition, where the margin of stability is slightly higher for the propeller's case.

10.4 Fuselage

The effects of the modeling options (wake model, Kutta condition) discussed in the previous sections are basically the same for the *wingbody* and *complete* configurations. Both models cause a redistribution of sectional lift that has a slight influence on the global lift and affects the pitching moment. The results are shown in Table 10.3.

It is interesting to compare the effect that the fuselage has on the aerodynamics of the whole aircraft. First of all, it is important to point out that the panel methods are based on the hypothesis of potential flows and are suitable to the study of streamlined bodies where no boundary layer separation occurs. While for small angles of attack the aft part of a fuselage can be considered as streamlined, in the rear part the boundary layer effects are

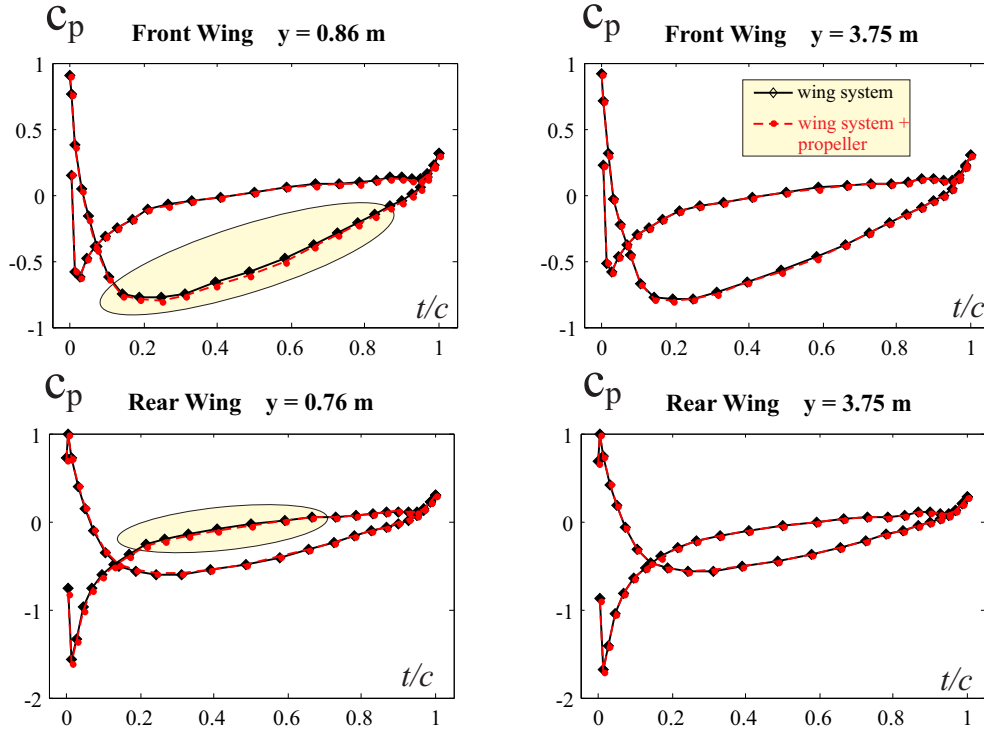


Figure 10.13: Pressure coefficient (c_p) distribution at front and rear wing root and tip sections, for *wingsystem* (wing-only) and *wingprop* (wing+propeller) cases. Free wake and iterative Kutta condition enforcement are considered.

not negligible and there is always flow separation in correspondence of the so-called *boat-tail*. These effects are not easy to include in a panel code. Even assuming that the separation occurs at the very end of the fuselage, it is difficult to simulate how the vorticity is shed into the wake because, in general, the boat tail is not sharp trailing edge and the Joukowski-Kutta condition is not applicable. Thus the main problem is that the present method is not able to accurately model the flow characteristics in the rear part of the fuselage. Because at low angles of attack the contributions of the fuselage to the lift of the whole configuration are small if compared the the lift generated by the wing system, the choice is to treat the fuselage as a non lifting body, without modeling any wake shedding. This way the main effects of the fuselage of deviating the streamlines, influencing the aerodynamics of the whole configuration, are preserved and are taken into account through the no-penetration condition. The flow separation on the boat-tail has a crucial role in the generation of drag

Simulation	C_L	C_D	C_{M_q}
<i>Wingbody</i> -IKC-Free	2,54E-01	3,80E-03	-1,59E-02
<i>Wingbody</i> -LKC-Free	2,64E-01	4,03E-03	-3,39E-02
<i>Wingbody</i> -IKC-Rigid	2,52E-01	4,85E-03	-3,30E-02
<i>Wingbody</i> -LKC-Rigid	2,63E-01	5,07E-03	-5,20E-02
<i>Complete</i> -IKC-Free	2,52E-01	3,22E-03	4,96E-03
<i>Complete</i> -LKC-Free	2,62E-01	3,33E-03	-9,79E-03
<i>Complete</i> -IKC-Rigid	2,54E-01	4,24E-03	-1,85E-02
<i>Complete</i> -LKC-Rigid	2,65E-01	4,35E-03	-3,57E-02

Table 10.3: Steady lift, drag and pitching moment coefficients for nominal cruise condition and different modeling approaches (LKC and IKC refer to the regular and iterative Kutta condition, Rigid/Free indicate the adopted wake modeling).

of a fuselage, while has little influence on the total lift of the whole aircraft. Thus, because of the limitations of the model, considering the fuselage as a non lifting body will lead to unacceptable results concerning the drag prediction of the whole configuration, but could still be useful to obtain some hints on how the presence of the fuselage affects the wings aerodynamics.

It can be useful to compare the results in terms of lift and pitching moment coefficients for the two cases *wingsystem* and *wingbody*. As the effects of the model options have already been discussed, a comparison will be made between the cases with the free wake and the iterative Kutta condition. Between the two configurations there is a significative difference in the lift coefficient (18%). The sectional lift $C_l \cdot c$ and the C_l spanwise distribution for both configurations are represented in Figure 10.14. As expected, the largest differences between the two cases concern the sections closer to the fuselage. Because the fuselage was modeled as a non-lifting body, for the case *wingbody* the sectional lift decreases as the spanwise coordinate y approaches the centerline: so it is possible to say that the presence of the fuselage perturbs the aerodynamic field of the wing system too, and its influence decreases as the distance of the wing sections from the centerline increases. This effects can be noticed on both wings. Concerning the front wing, it is important to recall that for *wingsystem* the gap of the fuselage was closed extending the root of the last wing section: thus, the extension is made of streamlined wing profiles and there is no lift drop. It is interesting to notice that closer to the wing tips, the sectional lift for the *wingbody* case actually is slightly higher than

the respective case without the fuselage.

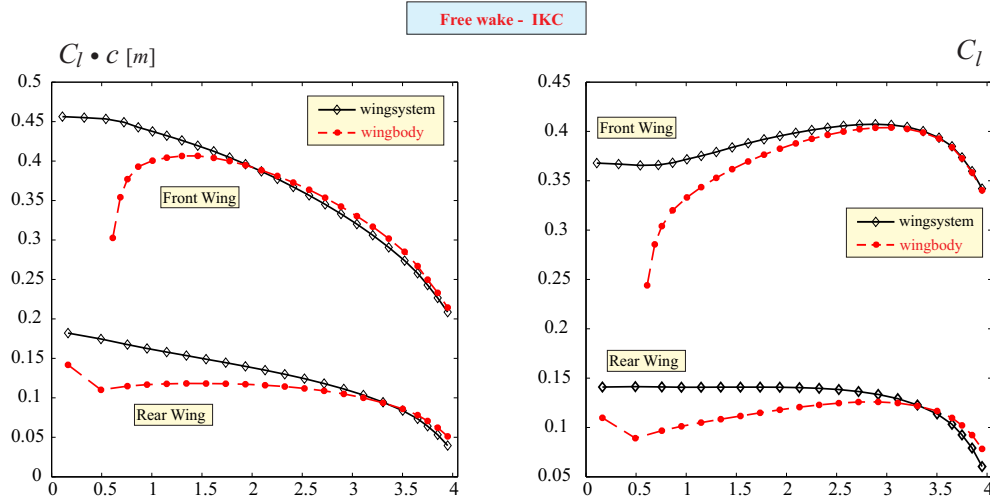


Figure 10.14: Sectional semi-normalized lift ($C_l \cdot c$) and lift coefficients (C_l) along the wing span for the *wing system* and *wingsbody* cases. Free wake and iterative Kutta condition enforcement are considered.

As the lift difference is higher on the front wing because in the *wingsystem* the fuselage has been replaced with a lifting extension of the front wing root sections, a tendency of the *wingbody* in nose pitch-up is confirmed by the numerical results.

The results of the static margin of stability are shown in Table 10.4. The presence of the fuselage reduces the static stability margin respect to the *wingsystem* configuration in case of free wake and iterative Kutta condition, while comparing the same configurations with rigid wake, the stability margin of *wingbody* is larger than *wingsystem*. The same results are obtained including the propeller in the simulation. Figure 10.15 shows the spanwise sectional lift and C_l distribution for the *wingbody* and *complete* configurations with iterative Kutta condition and free wake. As discussed for the *wingprop* configuration, the propeller increases the lift on the front wing, generating a suction peak on the upper face, and decreases the lift on the rear wing. In the *complete* configuration the lift reduction on the rear wing can be appreciated even at the wing tips: this is probably related to the combined influence of the fuselage and the propeller on the rear wing. In Figure 10.16 the wake evolution for the *complete* configuration is represented. The colors on the surface represents the values of the pressure coefficient on every panel.

Simulation	$-\frac{C_{M\alpha}}{c_{\text{mean}} \cdot C_{L\alpha}} (\%)$
<i>Wingbody</i> -IKC-Free	15,58 %
<i>Wingbody</i> -IKC-Rigid	23,22 %
<i>Complete</i> -IKC-Free	16,25%
<i>Complete</i> -IKC-Rigid	21,76%

Table 10.4: Static margin of longitudinal stability at nominal cruise condition and different modeling approaches (IKC refers to the regular and iterative Kutta condition, Rigid/Free indicate the adopted wake modeling).

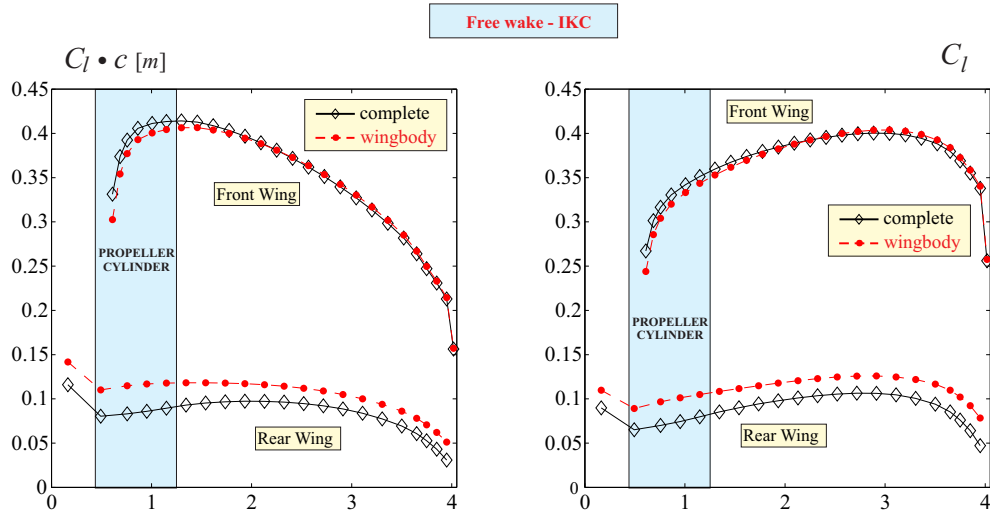


Figure 10.15: Sectional semi-normalized lift ($C_l \cdot c$) and lift coefficients (C_l) along the wing span for the *wingbody* and *complete* cases. Free wake and iterative Kutta condition enforcement are considered.

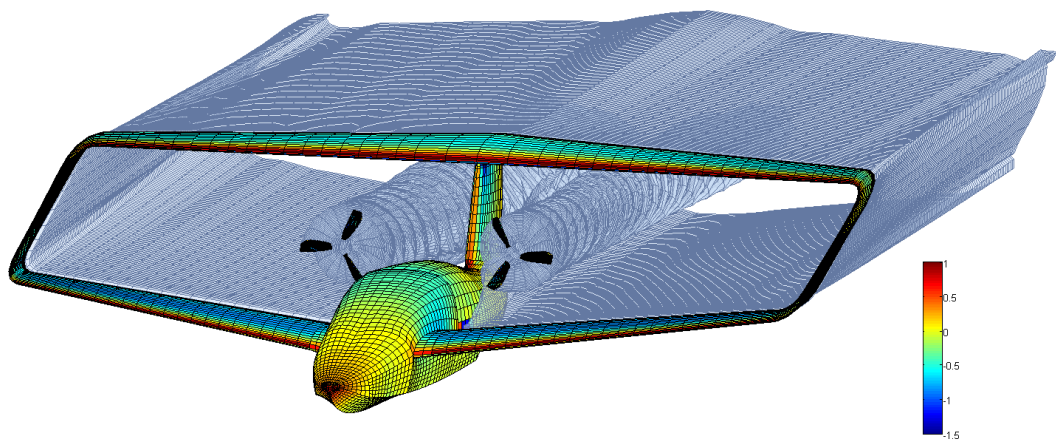


Figure 10.16: Wing shape of the *complete* configuration with iterative Kutta condition and free wake. The surface colors represents the values of the pressure coefficients on every panel.

Chapter 11

Conclusions

11.1 Discussion on the results

A three-dimensional multi-purpose low order unsteady panel method for the solution of potential flows around different geometries has been developed and validated. The panel method theory is based on a boundary element formulation involving a surface distribution of elemental solutions (sources and doublets) of the Laplace equation on the domain's boundaries. The problem of the existence and uniqueness of the solution has been discussed, including an insight on three-dimensional multiply-connected domains

The main characteristic of the code are here briefly summarized:

- low order panel method based on a constant strength distribution of singularities on first order quadrilateral panels representing the discretized geometry (bodies and wake);
- analogy between plane doublets and vortex rings for the velocities induced by the wake panels. A regularization function has been introduced to smooth the perturbation velocities induced by the vortex rings within a distance from the filament core called *core radius*, allowing to remove numerical instabilities;
- possibility to study cases of wake impingement on bodies through alternative formulation based on a decomposition of the perturbation potential into the contribution of the body and the far wake, and on the vortex regularization
- Kutta condition enforced with an iterative procedure for all those cases in which the Joukowski condition (bounded velocity without singularities on trailing edge) is not

enough to guarantee also a zero pressure jump across the trailing edge required by the Kutta condition;

- advanced kinematics module based on coordinate transformations between multiple reference systems. Linear and angular velocities are given as an input by the operator, while position and attitude of every reference system are obtained with a Fourth Order Runge-Kutta integration method. To determine the attitude, Hamilton's quaternions have been introduced to avoid the *gimbal lock* problem (loss of one degree of freedom) due to the singularity of the rotation matrix obtained with Euler's angles.

The code has been validated with multiple test cases. The results of the lift evolution on a high aspect ratio wing were compared to the analytical results provided by Wagner's theory. Moreover, Theodorsen oscillating wing results (in terms of lift and pitching moment) were reproduced. The thrust and power coefficients of a three-bladed propeller were compared to the experimental results provided by NASA and the alternative formulation for wake impingement was validated with the experimental results of a two-bladed rotor tested by Caradonna and Tung.

The second part of this work was focused on the application of the present code to an amphibious PrandtlPlane configuration, in order to evaluate the effects of the propellers on the aero-mechanics of the aircraft. The main results of the investigations are here summarized:

- the propellers performances in terms of thrust and power coefficient obtained with the present method were compared to the results obtained with a first order method based on the blade element theory. Because of the non-negligible differences observed, an investigation was carried out; the main reason of the discrepancy between the result was assumed to be the two-dimensional approach adopted by the blade element theory, which does not take into account the tip-losses due to the low aspect ratio of the propeller blades;
- a campaign of simulation was carried out on the PrandtlPlane Amphibious aircraft IDINTOS, in order to analyze the results in terms of lift and pitching moment and the longitudinal stability using different modeling approaches. Less accurate models like linear Kutta condition have proven to be non conservative, resulting in a higher lift and higher margin of stability respect to the model with free wake and iterative Kutta condition;

- the propellers modify the aircraft aerodynamics, increasing the sectional lift on the front wing and causing a lift drop on the rear wing, especially in those sections closer to the propeller's wake. This lift redistribution has slight influence on the global lift, but modifies the global pitching moment and the margin of stability;
- the problems related to the model of the fuselage, due to the flow separation in the rear part, have been discussed. The presence of the fuselage causes a reduction of lift on both wings respect to the wing system alone. It also changes the aircraft trim and the margin of stability.

11.2 Future developments

The issues and the problems met during the implementation of the code, have opened the way to possible developments. Some of them will be briefly introduced here:

- possibility to include the effects of the boundary layer. Panel methods can be coupled to a method to solve the integral boundary layers equations, in order to take into account also the viscous effects on the body surfaces. This can be important in all those cases in which there is flow separation (wings at high angle of attack, propellers at low advance ratios) as well as lower Reynolds number applications such as wind turbines;
- introduction of more accurate time-marching schemes for the wake evolution, such as predictor-corrector based schemes. This would be extremely useful in some rotor applications, where an explicit Euler method can lead to complex vortex instability phenomena;
- compressibility correction, to extend the applicability of the code to higher subsonic flows, where the flow compressibility effects are not negligible;
- coupling of the panel code with a structural one, to form an aeroelastic code and study the aeroelastic response of a body under the influence of unsteady aerodynamic loads such as gusts or wake interactions.

Appendices

Appendix A

Singularities

A.1 Constant strength quadrilateral doublet

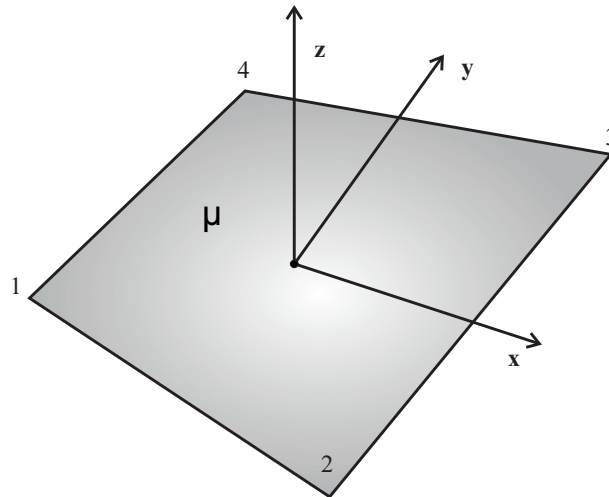


Figure A.1: Constant strength quadrilateral doublet

Figure A.1 shows a quadrilateral doublet panel of intensity μ with its local reference system. All the induction equations are referred to this system.

A.1.1 Velocity potential induction

According to [17], the panel with unitary doublet strength induces the following perturbation potential on the generic point P of coordinates (x, y, z) :

$$\begin{aligned} \varphi^d(x, y, z) = & -\frac{\mu}{4\pi} \left[\tan^{-1} \left(\frac{m_{12}e_1 - h_1}{zr_1} \right) - \tan^{-1} \left(\frac{m_{12}e_2 - h_2}{zr_2} \right) \right. \\ & + \tan^{-1} \left(\frac{m_{23}e_2 - h_2}{zr_2} \right) - \tan^{-1} \left(\frac{m_{23}e_3 - h_3}{zr_3} \right) \\ & + \tan^{-1} \left(\frac{m_{34}e_3 - h_3}{zr_3} \right) - \tan^{-1} \left(\frac{m_{34}e_4 - h_4}{zr_4} \right) \\ & \left. + \tan^{-1} \left(\frac{m_{41}e_4 - h_4}{zr_4} \right) - \tan^{-1} \left(\frac{m_{41}e_1 - h_1}{zr_1} \right) \right] \quad (\text{A.1}) \end{aligned}$$

where

$$\begin{aligned} m_{12} &= \frac{y_2 - y_1}{x_2 - x_1} & m_{23} &= \frac{y_3 - y_2}{x_3 - x_2} \\ m_{34} &= \frac{y_4 - y_3}{x_4 - x_3} & m_{41} &= \frac{y_1 - y_4}{x_1 - x_4} \\ r_k &= \sqrt{(x - x_k)^2 + (y - y_k)^2 + z^2} & k &= 1, 2, 3, 4 \\ e_k &= (x - x_k)^2 + z^2 & k &= 1, 2, 3, 4 \\ h_k &= (x - x_k)(y - y_k) & k &= 1, 2, 3, 4 \end{aligned}$$

A.1.2 Self-induction

The self induction of the panel on its center can be solved with a desingularization technique. Anyway, for a unit strength doublet panel:

$$\varphi(0, 0, z) = \begin{cases} \frac{\mu}{2} & z \rightarrow 0^+ \\ -\frac{\mu}{2} & z \rightarrow 0^- \end{cases} \quad (\text{A.2})$$

A.1.3 Farfield

To improve computational efficiency, when the distance between the generic point P and the center of the panel is greater than 3–5 times the typical dimension of the panel, the integral could be manipulated so that

$$\varphi^d(x, y, z) \approx \frac{\mu A_k}{4\pi} \frac{z}{(x^2 + y^2 + z^2)^{\frac{3}{2}}} \quad (\text{A.3})$$

which is the same influence of the point doublet with direction \mathbf{n} and intensity A_k , the area of the panel.

A.2 Constant strength quadrilateral source

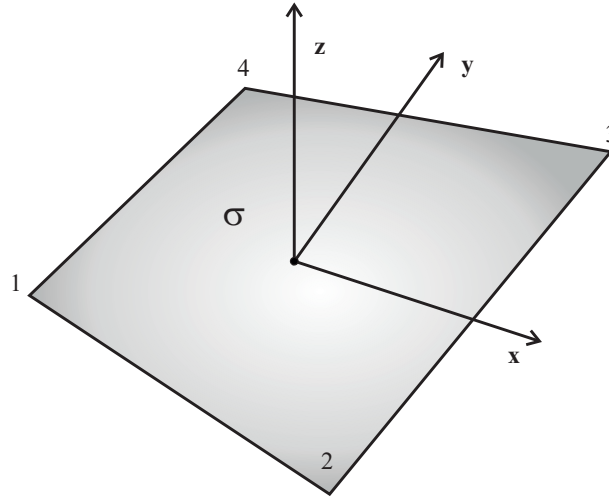


Figure A.2: Constant strength quadrilateral source

Figure A.2 shows a quadrilateral source panel with its local reference system. All the inductions equations are referred to this system.

A.2.1 Velocity potential induction

According to [17], the panel with unitary source strength induces the following potential on the generic point P of coordinates (x, y, z) :

$$\varphi^s = -(\varphi^{(l)} - z\varphi^d) \quad (\text{A.4})$$

where

$$\begin{aligned} \varphi^{(l)}(x, y, z) = & -\frac{\sigma}{4\pi} \left[\frac{(x-x_1)(y_2-y_1) - (y-y_1)(x_2-x_1)}{d_{12}} \ln \frac{r_1+r_2+d_{12}}{r_1+r_2-d_{12}} \right. \\ & + \frac{(x-x_2)(y_3-y_2) - (y-y_2)(x_3-x_2)}{d_{23}} \ln \frac{r_2+r_3+d_{23}}{r_2+r_3-d_{23}} \\ & + \frac{(x-x_3)(y_4-y_3) - (y-y_3)(x_4-x_3)}{d_{34}} \ln \frac{r_3+r_4+d_{34}}{r_3+r_4-d_{34}} \\ & \left. + \frac{(x-x_4)(y_1-y_4) - (y-y_4)(x_1-x_4)}{d_{41}} \ln \frac{r_4+r_1+d_{41}}{r_4+r_1-d_{41}} \right] \quad (\text{A.5}) \end{aligned}$$

A.2.2 Farfield

Again, to improve the computational efficiency, when the distance between the generic point P and the center of the panel is greater than 3 – 5 times the typical dimension of the panel, the integral could be manipulated so that

$$\varphi^{(l)} \approx \frac{\sigma A_k}{4\pi} \frac{1}{(x^2 + y^2 + z^2)^{\frac{1}{2}}} \quad (\text{A.6})$$

which is the same influence of the point source with intensity A_k , the area of the panel.

Appendix B

Sensitivity Matrix

For the iterative Kutta condition procedure, the following matrix is introduced:

$$\left[\frac{\partial \Delta Cp}{\partial \tilde{\mu}} \right]_{ij} = \frac{\partial \Delta Cp_i}{\partial \tilde{\mu}_j} = \sum_{k=1}^N \frac{\partial \Delta Cp_i}{\partial \mu_k} \frac{\partial \mu_k}{\partial \tilde{\mu}_j}. \quad (\text{B.1})$$

Matrix $\left[\frac{\partial \Delta Cp}{\partial \tilde{\mu}} \right]$ is a $N_{TE} \times N$ matrix and its called *sensitivity*; the generic element ij expresses the variation of pressure jump on trailing edge panel i cause by a variation of the j -th wake doublet strength $\tilde{\mu}_j$.

The sensitivity matrix can be obtained by the product of two different matrices

$$\left[\frac{\partial \Delta Cp}{\partial \tilde{\mu}} \right] = \left[\frac{\partial \Delta Cp}{\partial \mu} \right] \left[\frac{\partial \mu}{\partial \tilde{\mu}} \right] = \left[\frac{\partial \Delta Cp}{\partial \mu} \right] [A]^{-1} [C], \quad (\text{B.2})$$

where $\left[\frac{\partial \mu}{\partial \tilde{\mu}} \right]$ has already been found in Section 3.7, while $\left[\frac{\partial \Delta Cp}{\partial \mu} \right]$ will be obtained in this section.

Remembering Equation 3.67, it is

$$\left[\frac{\partial \Delta Cp}{\partial \tilde{\mu}} \right] = \left[\frac{\partial \Delta Cp}{\partial \mu} \right] \left[\frac{\partial \mu}{\partial \tilde{\mu}} \right] = \left[\frac{\partial \Delta Cp}{\partial \mu} \right] [A]^{-1} [C]. \quad (\text{B.3})$$

By definition, vector ΔCp represents the pressure jump across trailing edge $\Delta Cp = Cp^{up} - Cp^{down}$ and from the definition of pressure coefficient, it is:

$$\Delta Cp = -||\mathbf{V}_w^{up} - \mathbf{V}_b^{up} + \mathbf{v}_p^{up}||^2 + ||\mathbf{V}_w^{down} - \mathbf{V}_b^{down} + \mathbf{v}_p^{down}||^2 - 2\frac{\partial \varphi^{up}}{\partial t} + 2\frac{\partial \varphi^{down}}{\partial t}. \quad (\text{B.4})$$

Knowing that

- $V_w^{up} = V_w^{down}$
- $V_b^{up} \approx V_b^{down}$ ¹

and after some manipulations

$$\begin{aligned} \Delta C p = & - \|\mathbf{v}_p^{up}\|^2 + \|\mathbf{v}_p^{down}\|^2 - \\ & 2(\mathbf{V}_w - \mathbf{V}_b) \cdot (\mathbf{v}_p^{up} - \mathbf{v}_p^{down}) + \frac{\partial \varphi^{up}}{\partial t} - \frac{\partial \varphi^{down}}{\partial t}. \end{aligned} \quad (B.5)$$

Using vector identity $\|\mathbf{a}\| = \mathbf{a} \cdot \mathbf{a}$, where \mathbf{a} is a generic vector, and deriving respect to the doublet intensities, it is

$$\begin{aligned} \frac{\partial \Delta C p_i}{\partial \mu_j} = & - 2\mathbf{v}_{p_i}^{up} \cdot \frac{\partial \mathbf{v}_{p_i}^{up}}{\partial \mu_j} + 2\mathbf{v}_{p_i}^{down} \cdot \frac{\partial \mathbf{v}_{p_i}^{down}}{\partial \mu_j} \\ & - 2(\mathbf{V}_w - \mathbf{V}_b) \cdot \left(\frac{\partial \mathbf{v}_{p_i}^{down}}{\partial \mu_j} - \frac{\partial \mathbf{v}_{p_i}^{up}}{\partial \mu_j} \right) + \frac{\partial \varphi^{up}}{\partial t} - \frac{\partial \varphi^{down}}{\partial t}. \end{aligned} \quad (B.6)$$

Remembering that $\varphi_i = \mu_i$ and $\mathbf{v}_p = \nabla \varphi$, then

$$\begin{aligned} \frac{\partial \Delta C p_i}{\partial \mu_j} = & - 2\nabla \mu_i^{up} \frac{\partial \nabla \mu_i^{up}}{\partial \mu_j} + 2\nabla \mu_i^{down} \frac{\partial \nabla \mu_i^{down}}{\partial \mu_j} - \\ & 2(\mathbf{V}_w - \mathbf{V}_b) \cdot \left(\frac{\partial \nabla \mu_i^{down}}{\partial \mu_j} - \frac{\partial \nabla \mu_i^{up}}{\partial \mu_j} \right) + \frac{\partial \mu^{up}}{\partial t} - \frac{\partial \mu^{down}}{\partial t}. \end{aligned} \quad (B.7)$$

The expression for $\nabla \varphi_i$ has been obtained in Section 3.6: it can be derived again by μ_j to obtain the term $\frac{\partial \nabla \mu_i}{\partial \mu_j}$. Concerning the time derivative, this is achieved using a linear formula

$$\frac{\partial \mu_i}{\partial t} = \frac{\mu_i(T) - \mu_i(T - \Delta T)}{\Delta T} \quad (B.8)$$

where T indicates the current timestep of the simulation, $T - \Delta T$ the previous timestep and ΔT is the time advancing interval of the simulation.

¹Because the control points are not on trailing edge, the two velocities are not exactly equal, but this is in general not relevant for the numerical formulation.

Appendix C

Kinematics

C.1 Rotation matrix

Using Euler Angles defined in Section 5.1.1, the orientation of a reference system \mathcal{B} is given with respect to a reference system \mathcal{A} . To obtain the rotation matrix that transforms the coordinate of a generic vector from system \mathcal{B} to system \mathcal{A} , three consecutive rotations are necessary.

Rotation around axis x of system \mathcal{B}

$$\begin{Bmatrix} x \\ y' \\ z' \end{Bmatrix} = \begin{bmatrix} 1 & 0 & 0 \\ 0 & \cos \phi & -\sin \phi \\ 0 & \sin \phi & \cos \phi \end{bmatrix} \begin{Bmatrix} x \\ y \\ z \end{Bmatrix}_B \quad (\text{C.1})$$

Rotation around intermediate axis y'

$$\begin{Bmatrix} x' \\ y' \\ z_{\mathcal{A}} \end{Bmatrix} = \begin{bmatrix} \cos \theta & 0 & \sin \theta \\ 0 & 1 & 0 \\ -\sin \theta & 0 & \cos \theta \end{bmatrix} \begin{Bmatrix} x \\ y' \\ z' \end{Bmatrix}_B \quad (\text{C.2})$$

Rotation around axis z of system \mathcal{A}

$$\begin{Bmatrix} x \\ y \\ z \end{Bmatrix}_{\mathcal{A}} = \begin{bmatrix} \cos \psi & -\sin \psi & 0 \\ \sin \psi & \cos \psi & 0 \\ 0 & 0 & 1 \end{bmatrix} \begin{Bmatrix} x' \\ y' \\ z_{\mathcal{A}} \end{Bmatrix}_B \quad (\text{C.3})$$

The final rotation matrix is obtained applying the three consecutive rotations

$$[\Omega_{rot}^{\mathcal{B} \rightarrow \mathcal{A}}] = \begin{bmatrix} \cos \psi & -\sin \psi & 0 \\ \sin \psi & \cos \psi & 0 \\ 0 & 0 & 1 \end{bmatrix} \begin{bmatrix} \cos \theta & 0 & \sin \theta \\ 0 & 1 & 0 \\ -\sin \theta & 0 & \cos \theta \end{bmatrix} \begin{bmatrix} 1 & 0 & 0 \\ 0 & \cos \phi & -\sin \phi \\ 0 & \sin \phi & \cos \phi \end{bmatrix} \quad (\text{C.4})$$

and the final expression is

$$[\Omega_{rot}^{\mathcal{B} \rightarrow \mathcal{A}}] = \begin{bmatrix} \cos \theta \cos \psi & \sin \phi \sin \theta \cos \psi - \cos \phi \sin \psi & \cos \phi \sin \theta \cos \psi + \sin \phi \sin \psi \\ \cos \theta \sin \psi & \sin \theta + \cos \psi & \sin \theta - \sin \phi \cos \psi \\ -\sin \theta & \sin \phi \cos \theta & \cos \phi \theta \end{bmatrix}. \quad (\text{C.5})$$

C.2 Transformation between multiple coordinate systems

As the whole kinematic module implemented in the aerodynamic solver is based on coordinate transformations between multiple reference systems, it is important to show that knowing the transformation between system \mathcal{A} and system \mathcal{B} and between system \mathcal{B} to system \mathcal{C} , it is possible to obtain the transformation between \mathcal{A} and \mathcal{C} . Starting from the coordinate transformation of a point P from B to \mathcal{A}

$$\mathbf{O}_A \mathbf{P}^{\mathcal{A}} = \mathbf{O}_A \mathbf{O}_{\mathcal{B}}^{\mathcal{A}} + \Omega_{rot}^{\mathcal{B} \rightarrow \mathcal{A}} \mathbf{O}_{\mathcal{B}} \mathbf{P}^{\mathcal{B}}. \quad (\text{C.6})$$

and considering the transformation of the coordinates of a point P from \mathcal{C} to \mathcal{B}

$$\mathbf{O}_B \mathbf{P}^{\mathcal{B}} = \mathbf{O}_B \mathbf{O}_{\mathcal{C}}^{\mathcal{B}} + \Omega_{rot}^{\mathcal{C} \rightarrow \mathcal{B}} \mathbf{O}_{\mathcal{C}} \mathbf{P}^{\mathcal{C}}. \quad (\text{C.7})$$

it is possible to combine the two transformations, obtaining the coordinates of point P from \mathcal{C} to \mathcal{A} :

$$\mathbf{O}_A \mathbf{P}^{\mathcal{A}} = \mathbf{O}_A \mathbf{O}_{\mathcal{C}}^{\mathcal{A}} + \Omega_{rot}^{\mathcal{C} \rightarrow \mathcal{A}} \mathbf{O}_{\mathcal{C}} \mathbf{P}^{\mathcal{C}}. \quad (\text{C.8})$$

$$\mathbf{O}_A \mathbf{P}^{\mathcal{A}} = \mathbf{O}_A \mathbf{O}_{\mathcal{B}}^{\mathcal{A}} + \Omega_{rot}^{\mathcal{B} \rightarrow \mathcal{A}} [\mathbf{O}_{\mathcal{B}} \mathbf{O}_{\mathcal{C}}^{\mathcal{B}} + \Omega_{rot}^{\mathcal{C} \rightarrow \mathcal{B}} \mathbf{O}_{\mathcal{C}} \mathbf{P}^{\mathcal{C}}]. \quad (\text{C.9})$$

Equation C.9 can be rewritten in terms of a translational part and a rotational part that multiplies vector $\mathbf{x}_{\mathcal{P}}^{\mathcal{C}}$:

$$\mathbf{O}_A \mathbf{P}^{\mathcal{A}} = \mathbf{tr} + [\mathbf{ROT}] \mathbf{O}_{\mathcal{C}} \mathbf{P}^{\mathcal{C}} \quad (\text{C.10})$$

where

$$tr = O_{\mathcal{A}} O_{\mathcal{B}}^{\mathcal{A}} + \Omega_{rot}^{\mathcal{B} \rightarrow \mathcal{A}} O_{\mathcal{B}} O_{\mathcal{C}}^{\mathcal{B}} \quad (C.11)$$

$$[ROT] = \Omega_{rot}^{\mathcal{B} \rightarrow \mathcal{A}} \Omega_{rot}^{\mathcal{C} \rightarrow \mathcal{B}} \quad (C.12)$$

The procedure can be generalized with n intermediate coordinate systems. Imagining to transform from system \mathcal{A}_n to \mathcal{A} through n intermediate coordinate systems, the expression of the coordinates of a generic point P can always be written decomposing the contributions of the translational part and the rotational part

$$O_{\mathcal{A}} P^{\mathcal{A}} = tr + [ROT] O_{\mathcal{A}_n} P^{\mathcal{A}_n} \quad (C.13)$$

where

$$tr = O_{\mathcal{A}} O_{\mathcal{A}_1}^{\mathcal{A}} + \Omega^{\mathcal{A}_1 \rightarrow \mathcal{A}} O_{\mathcal{A}_1} O_{\mathcal{A}_2}^{\mathcal{A}_1} + \dots + \Omega^{\mathcal{A}_1 \rightarrow \mathcal{A}} \Omega^{\mathcal{A}_2 \rightarrow \mathcal{A}_1} \dots \Omega^{\mathcal{A}_n \rightarrow \mathcal{A}_{n-1}} O_{\mathcal{A}_{n-1}} O_{\mathcal{A}_n}^{\mathcal{A}_{n-1}}$$

$$[ROT] = \Omega^{\mathcal{A}_1 \rightarrow \mathcal{A}} \Omega^{\mathcal{A}_2 \rightarrow \mathcal{A}_1} \dots \Omega^{\mathcal{A}_n \rightarrow \mathcal{A}_{n-1}}.$$

This procedure is adopted in the aerodynamic solver to find the transformation matrices between all the coordinate systems present in the simulation.

C.3 Angular velocity and Euler Angles derivatives

Consider a frame of reference \mathcal{B} rotating with respect to another frame \mathcal{A} with an angular velocity $\omega_{\mathcal{B} \rightarrow \mathcal{A}}^{\mathcal{A}} = p\mathbf{i}_{\mathcal{A}} + q\mathbf{j}_{\mathcal{A}} + r\mathbf{k}_{\mathcal{A}}$, where $\mathbf{i}_{\mathcal{A}}$, $\mathbf{j}_{\mathcal{A}}$, $\mathbf{k}_{\mathcal{A}}$ are the unit vectors of the axis of frame \mathcal{A} . According to the definition of Euler Angles, the following relation is also correct

$$\omega_{\mathcal{B} \rightarrow \mathcal{A}}^{\mathcal{A}} = \dot{\phi}\mathbf{i}_e + \dot{\theta}\mathbf{j}_e + \dot{\psi}\mathbf{k}_e \quad (C.14)$$

where \mathbf{i}_e , \mathbf{j}_e , \mathbf{k}_e are the unit vectors around which the rotations are performed: they depend on the particular choice of the Euler Angles. Defining angles as introduced in Section 5.1.1 (*Tait-Bryan angles*) and observing Figure 5.2, it is possible to notice that

- $\mathbf{i}_{\mathcal{A}} = \mathbf{i}_e$
- $\mathbf{j}_{\mathcal{A}}$ is obtained from \mathbf{j}_e after a rotation of an angle ϕ around \mathbf{i} axis
- $\mathbf{k}_e = \mathbf{k}_{\mathcal{B}}$. $\mathbf{k}_{\mathcal{A}}$ is obtained from $\mathbf{k}_{\mathcal{B}}$ after three consecutive rotations ϕ , θ , ψ .

Combining this information, it is possible to obtain a rotation matrix that allows to convert the angular velocity defined through Euler Angle derivatives, into the angular velocity expressed in the considered frame of reference \mathcal{A} :

$$\left\{ \begin{array}{c} p \\ q \\ r \end{array} \right\}_{\mathcal{B} \rightarrow \mathcal{A}}^{\mathcal{A}} = \begin{bmatrix} 1 & 0 & -\sin \theta \\ 0 & \cos \phi & \cos \theta \sin \phi \\ 0 & -\sin \phi & \cos \theta \cos \phi \end{bmatrix} \left\{ \begin{array}{c} \dot{\phi} \\ \dot{\theta} \\ \dot{\psi} \end{array} \right\}. \quad (\text{C.15})$$

The transformation matrix that transforms the angular velocity of system \mathcal{B} respect to system \mathcal{A} from the coordinates of \mathcal{A} to Euler angles derivatives is indicated as

$$\Omega_{EA \rightarrow \mathcal{A}} = \begin{bmatrix} 1 & 0 & -\sin \theta \\ 0 & \cos \phi & \cos \theta \sin \phi \\ 0 & -\sin \phi & \cos \theta \cos \phi \end{bmatrix} \quad (\text{C.16})$$

The inverse rotation is obtained trivially inverting the rotation matrix:

$$\left\{ \begin{array}{c} \dot{\phi} \\ \dot{\theta} \\ \dot{\psi} \end{array} \right\} = \begin{bmatrix} 1 & \tan \theta \sin \phi & \tan \theta \cos \phi \\ 0 & \cos \phi & -\sin \phi \\ 0 & \frac{\sin \phi}{\cos \theta} & \frac{\cos \phi}{\cos \theta} \end{bmatrix} \left\{ \begin{array}{c} p \\ q \\ r \end{array} \right\}_{\mathcal{B} \rightarrow \mathcal{A}}^{\mathcal{A}}. \quad (\text{C.17})$$

Indicating with $\Omega_{EA \rightarrow \mathcal{A}}$ the inverse matrix of $\Omega_{\mathcal{A} \rightarrow EA}$, it is

$$\Omega_{\mathcal{A} \rightarrow EA} = \begin{bmatrix} 1 & \tan \theta \sin \phi & \tan \theta \cos \phi \\ 0 & \cos \phi & -\sin \phi \\ 0 & \frac{\sin \phi}{\cos \theta} & \frac{\cos \phi}{\cos \theta} \end{bmatrix}. \quad (\text{C.18})$$

It is possible to observe that the inverse does not coincide with the transpose matrix and that for $\theta \rightarrow (\frac{\pi}{2} \pm n\pi)$ the matrix becomes singular.

C.4 Fourth Order Runge-Kutta integration

Runge-Kutta methods are numerical multi-stage, single step integration methods and are often used in the solution of Ordinary Differential Equations. In this section, only the principles of the method will be introduced; for further details see [28].

Consider the following Ordinary Differential Equation

$$\begin{cases} \frac{dy}{dt} = f(y(t), t) \\ y(t_n) = y_n \end{cases} \quad (\text{C.19})$$

Starting from the initial value y_n at the time t_n , a Runge-Kutta method allows to evaluate the solution y_{n+1} at the time $t + \Delta t$ using the information from a certain number of intermediate steps. The formula for the Fourth Order Runge-Kutta scheme is the following:

$$y_{n+1} = y_n + \frac{1}{6}\Delta t (k_1 + 2k_2 + 2k_3 + k_4) + O(\Delta t^5) \quad (\text{C.20})$$

where

$$\begin{aligned} k_1 &= f(y_n, t_n) \\ k_2 &= f\left(y_n + \frac{k_1}{2}, t_n + \frac{\Delta t}{2}\right) \\ k_3 &= f\left(y_n + \frac{k_2}{2}, t_n + \frac{\Delta t}{2}\right) \\ k_4 &= f(y_n + k_3, t_n + \Delta t). \end{aligned}$$

To obtain the solution at the new time $t + \Delta t$, four coefficients are required: they are results of the evaluation of the differential equation in four intermediate stages between t and $t + \Delta t$. The Fourth Order Runge-Kutta is an explicit scheme.

C.5 Derivative of a vector expressed in a different frame of reference

Consider two frame of references \mathcal{A} and \mathcal{B} and a vector \mathbf{x}_P . Notation $\mathbf{x}_P^{\mathcal{A}}$ indicates the vector expressed in coordinates of frame \mathcal{A} , while $\mathbf{x}_P^{\mathcal{B}}$ is the same vector expressed in coordinates of frame \mathcal{B} .

$\Omega_{rot}^{\mathcal{A} \rightarrow \mathcal{B}}$ and $\Omega_{rot}^{\mathcal{B} \rightarrow \mathcal{A}}$ are, respectively, the rotation matrixes from \mathcal{A} to \mathcal{B} and from \mathcal{B} to \mathcal{A} .

Applying a coordinate transformation, it is possible to write

$$\mathbf{x}_P^{\mathcal{B}} = \Omega_{rot}^{\mathcal{A} \rightarrow \mathcal{B}} \mathbf{x}_P^{\mathcal{A}}. \quad (\text{C.21})$$

Deriving both members with respect to time

$$\frac{\partial \mathbf{x}_P^{\mathcal{B}}}{\partial t} = \frac{\partial}{\partial t} (\Omega_{rot}^{\mathcal{A} \rightarrow \mathcal{B}}) \mathbf{x}_P^{\mathcal{A}} + \Omega_{rot}^{\mathcal{A} \rightarrow \mathcal{B}} \frac{\partial \mathbf{x}_P^{\mathcal{A}}}{\partial t} \quad (\text{C.22})$$

and applying a coordinate transformation, it results

$$\frac{\partial \mathbf{x}_P^{\mathcal{B}}}{\partial t} = \frac{\partial}{\partial t} (\Omega_{rot}^{\mathcal{A} \rightarrow \mathcal{B}}) \Omega_{rot}^{\mathcal{B} \rightarrow \mathcal{A}} \mathbf{x}_P^{\mathcal{B}} + \Omega_{rot}^{\mathcal{A} \rightarrow \mathcal{B}} \frac{\partial \mathbf{x}_P^{\mathcal{A}}}{\partial t}. \quad (\text{C.23})$$

It is important to understand the meaning of $\frac{\partial \mathbf{x}_P^{\mathcal{A}}}{\partial t}$: it indicates the variation in time of vector \mathbf{x}_P expressed in the coordinates of frame \mathcal{A} . Matrix $\Omega_{rot}^{\mathcal{A} \rightarrow \mathcal{B}}$ performs a rotation on such vector, expressing the variation in time of $\mathbf{x}_P^{\mathcal{A}}$ in coordinates of system \mathcal{B} : to indicate $\Omega_{rot}^{\mathcal{A} \rightarrow \mathcal{B}} \frac{\partial \mathbf{x}_P^{\mathcal{A}}}{\partial t}$ the notation $\left(\frac{\partial \mathbf{x}_P^{\mathcal{A}}}{\partial t}\right)^{\mathcal{B}}$ is used.

Referring to equation C.23, the term $\frac{\partial}{\partial t} (\Omega_{rot}^{\mathcal{A} \rightarrow \mathcal{B}})$ is a matrix associated to the vector angular velocity of \mathcal{A} with respect to \mathcal{B} , expressed in \mathcal{A} coordinates. If vector angular velocity is indicated with $\boldsymbol{\omega}_{\mathcal{A} \rightarrow \mathcal{B}}^{\mathcal{A}}$, it is possible to write

$$\frac{\partial}{\partial t} (\Omega_{rot}^{\mathcal{A} \rightarrow \mathcal{B}}) = \begin{pmatrix} 0 & -\omega_{\mathcal{A} \rightarrow \mathcal{B}}^{\mathcal{A}}|_z & \omega_{\mathcal{A} \rightarrow \mathcal{B}}^{\mathcal{A}}|_y \\ \omega_{\mathcal{A} \rightarrow \mathcal{B}}^{\mathcal{A}}|_z & 0 & -\omega_{\mathcal{A} \rightarrow \mathcal{B}}^{\mathcal{A}}|_x \\ -\omega_{\mathcal{A} \rightarrow \mathcal{B}}^{\mathcal{A}}|_y & \omega_{\mathcal{A} \rightarrow \mathcal{B}}^{\mathcal{A}}|_x & 0 \end{pmatrix} \quad (\text{C.24})$$

The product between matrix shown in Equation C.24 and a generic vector \mathbf{a} is equal to the cross product $\boldsymbol{\omega}_{\mathcal{A} \rightarrow \mathcal{B}}^{\mathcal{A}} \times \mathbf{a}$, so Equation C.23 can be rewritten in the following form:

$$\frac{\partial \mathbf{x}_P^{\mathcal{B}}}{\partial t} = \boldsymbol{\omega}_{\mathcal{A} \rightarrow \mathcal{B}}^{\mathcal{B}} \times \mathbf{x}_P^{\mathcal{B}} + \Omega_{rot}^{\mathcal{A} \rightarrow \mathcal{B}} \frac{\partial \mathbf{x}_P^{\mathcal{A}}}{\partial t} \quad (\text{C.25})$$

where matrix C.24 has been rotated due to the right product with $\Omega_{rot}^{\mathcal{B} \rightarrow \mathcal{A}}$. This is equal to a transformation of vector $\boldsymbol{\omega}_{\mathcal{A} \rightarrow \mathcal{B}}^{\mathcal{A}}$ into the coordinates of frame \mathcal{B} and has been indicated with $\boldsymbol{\omega}_{\mathcal{A} \rightarrow \mathcal{B}}^{\mathcal{B}}$. In case point P is not moving with respect to frame of reference \mathcal{A} , for example if P belongs to a rigid body attached to \mathcal{A} , it is $\frac{\partial \mathbf{x}_P^{\mathcal{A}}}{\partial t} = 0$, thus, for a rigid body, Equation C.23 can be written as

$$\frac{\partial \mathbf{x}_P^{\mathcal{B}}}{\partial t} = \boldsymbol{\omega}_{\mathcal{A} \rightarrow \mathcal{B}}^{\mathcal{B}} \times \mathbf{x}_P^{\mathcal{B}}. \quad (\text{C.26})$$

C.6 Derivative of a quaternion in another frame of reference

As was done in the previous section, two Cartesian coordinate systems \mathcal{A} and \mathcal{B} and a vector \mathbf{x}_P are introduced. $\mathbf{x}_P^{\mathcal{A}}$ and $\mathbf{x}_P^{\mathcal{B}}$ indicates the coordinates of the vector with respect to the two frames of reference. According to 5.17, indicating with $\mathcal{R}^{\hat{q}}(\hat{p}) = \hat{q}^* \circ \hat{p} \circ \hat{q}$ the coordinate transformation between \mathcal{A} and \mathcal{B} , converting vectors $\mathbf{x}_P^{\mathcal{A}}$ and $\mathbf{x}_P^{\mathcal{B}}$ into pure quaternions and remembering that for a unit quaternion $\hat{q}^{-1} = \hat{q}^*$, it is possible to write:

$$\begin{Bmatrix} 0 \\ \mathbf{x}_P^{\mathcal{B}} \end{Bmatrix} = \hat{q}^* \circ \begin{Bmatrix} 0 \\ \mathbf{x}_P^{\mathcal{A}} \end{Bmatrix} \circ \hat{q} \quad (\text{C.27})$$

$$\begin{Bmatrix} 0 \\ \mathbf{x}_P^{\mathcal{A}} \end{Bmatrix} = \hat{q} \circ \begin{Bmatrix} 0 \\ \mathbf{x}_P^{\mathcal{B}} \end{Bmatrix} \circ \hat{q}^*. \quad (\text{C.28})$$

Performing the time derivatives, equation C.27 becomes

$$\frac{\partial}{\partial t} \begin{Bmatrix} 0 \\ \mathbf{x}_P^{\mathcal{B}} \end{Bmatrix} = \frac{\partial \hat{q}^*}{\partial t} \circ \begin{Bmatrix} 0 \\ \mathbf{x}_P^{\mathcal{A}} \end{Bmatrix} \circ \hat{q} + \hat{q}^* \circ \begin{Bmatrix} 0 \\ \mathbf{x}_P^{\mathcal{A}} \end{Bmatrix} \circ \frac{\partial \hat{q}}{\partial t} + \hat{q}^* \circ \begin{Bmatrix} 0 \\ \frac{\partial \mathbf{x}_P^{\mathcal{A}}}{\partial t} \end{Bmatrix} \circ \hat{q} \quad (\text{C.29})$$

and considering P attached to system \mathcal{A} such as $\frac{\partial \mathbf{x}_P^{\mathcal{A}}}{\partial t} = 0$, it is

$$\frac{\partial}{\partial t} \begin{Bmatrix} 0 \\ \mathbf{x}_P^{\mathcal{B}} \end{Bmatrix} = \frac{\partial \hat{q}^*}{\partial t} \circ \begin{Bmatrix} 0 \\ \mathbf{x}_P^{\mathcal{A}} \end{Bmatrix} \circ \hat{q} + \hat{q}^* \circ \begin{Bmatrix} 0 \\ \mathbf{x}_P^{\mathcal{A}} \end{Bmatrix} \circ \frac{\partial \hat{q}}{\partial t}. \quad (\text{C.30})$$

Substituting Equation C.28 in Equation C.30, it is possible to write

$$\frac{\partial}{\partial t} \begin{Bmatrix} 0 \\ \mathbf{x}_P^{\mathcal{B}} \end{Bmatrix} = \frac{\partial \hat{q}^*}{\partial t} \circ \hat{q} \circ \begin{Bmatrix} 0 \\ \mathbf{x}_P^{\mathcal{B}} \end{Bmatrix} \circ \hat{q}^* \circ \hat{q} + \hat{q}^* \circ \hat{q} \circ \begin{Bmatrix} 0 \\ \mathbf{x}_P^{\mathcal{B}} \end{Bmatrix} \circ \hat{q}^* \circ \frac{\partial \hat{q}}{\partial t} \quad (\text{C.31})$$

and recalling that for a unit quaternion $\hat{q}^* \circ \hat{q} = \hat{q} \circ \hat{q}^* = 1$, it holds

$$\frac{\partial}{\partial t} \begin{Bmatrix} 0 \\ \mathbf{x}_P^{\mathcal{B}} \end{Bmatrix} = \frac{\partial \hat{q}^*}{\partial t} \circ \hat{q} \circ \begin{Bmatrix} 0 \\ \mathbf{x}_P^{\mathcal{B}} \end{Bmatrix} + \begin{Bmatrix} 0 \\ \mathbf{x}_P^{\mathcal{B}} \end{Bmatrix} \circ \hat{q}^* \circ \frac{\partial \hat{q}}{\partial t} \quad (\text{C.32})$$

To simplify the last equation, consider the following expression

$$\hat{q}^* \circ \hat{q} = 1 \quad (\text{C.33})$$

and its time derivative

$$\frac{\partial}{\partial t} (\hat{q}^* \circ \hat{q}) = \frac{\partial \hat{q}^*}{\partial t} \circ \hat{q} + \hat{q}^* \circ \frac{\partial \hat{q}}{\partial t} = 0. \quad (\text{C.34})$$

From C.34, using the following identity

$$\frac{\partial \hat{q}^*}{\partial t} \circ \hat{q} = -\hat{q}^* \circ \frac{\partial \hat{q}}{\partial t} = -\left(\frac{\partial \hat{q}^*}{\partial t} \circ \hat{q} \right)^* \quad (\text{C.35})$$

and according to the definition, it is possible to state that $\frac{\partial \hat{q}^*}{\partial t} \circ \hat{q}$ is a pure quaternion.

Substituting Equation C.35 in Equation C.32, it leads to

$$\frac{\partial}{\partial t} \begin{Bmatrix} 0 \\ \mathbf{x}_P^{\mathcal{B}} \end{Bmatrix} = 2 \frac{\partial \hat{q}}{\partial t} \circ \hat{q}^* \circ \begin{Bmatrix} 0 \\ \mathbf{x}_P^{\mathcal{B}} \end{Bmatrix}. \quad (\text{C.36})$$

C.7 From quaternions to rotation matrix

In Section 5.1.1 the rotation matrix $\Omega_{rot}^{A \rightarrow B}$ between two frames of reference \mathcal{A} and \mathcal{B} was obtained from the definition of Euler Angles. As already seen, considering a generic vector \mathbf{x}_P , it holds that:

$$\{\mathbf{x}_P^{\mathcal{B}}\} = [\Omega_{rot}^{A \rightarrow B}] \{\mathbf{x}_P^{\mathcal{A}}\} \quad (C.37)$$

where

$$\Omega_{rot}^{A \rightarrow B} = \begin{bmatrix} \cos \theta \cos \psi & \sin \phi \sin \theta \cos \psi - \cos \phi \sin \psi & \cos \phi \sin \theta \cos \psi + \sin \phi \sin \psi \\ \cos \theta \sin \psi & \sin \theta + \cos \psi & \sin \theta - \sin \phi \cos \psi \\ -\sin \theta & \sin \phi \cos \theta & \cos \phi \cos \theta \end{bmatrix} \quad (C.38)$$

Performing the same rotation using quaternions

$$\begin{Bmatrix} 0 \\ \mathbf{x}_P^{\mathcal{B}} \end{Bmatrix} = \hat{q} \circ \begin{Bmatrix} 0 \\ \mathbf{x}_P^{\mathcal{A}} \end{Bmatrix} \circ \hat{q}^* \quad (C.39)$$

and recalling the definition of quaternion product, with some manipulations it is possible to show that equation C.39 can be expressed in the same form of C.37, where

$$\Omega_{rot}^{A \rightarrow B} = \begin{bmatrix} q_0^2 + q_1^2 + q_2^2 + q_3^2 & 2(q_1 q_2 - q_3 q_0) & 2(q_1 q_3 - q_2 q_0) \\ 2(q_1 q_2 - q_3 q_0) & q_0^2 - q_1^2 + q_2^2 - q_3^2 & 2(q_2 q_3 - q_1 q_0) \\ 2(q_1 q_3 - q_2 q_0) & 2(q_2 q_3 - q_1 q_0) & q_0^2 - q_1^2 - q_2^2 + q_3^2 \end{bmatrix}. \quad (C.40)$$

To convert a rotation matrix into a quaternion, recalling that a unit quaternion, by definition, has a unit norm, from C.40 the following relations can be obtained:

$$q_0^2 = \frac{1}{4} (1 + \Omega_{11}^{A \rightarrow B} + \Omega_{22}^{A \rightarrow B} + \Omega_{33}^{A \rightarrow B}) \quad (C.41)$$

$$q_1^2 = \frac{1}{4} (1 + \Omega_{11}^{A \rightarrow B} - \Omega_{22}^{A \rightarrow B} - \Omega_{33}^{A \rightarrow B}) \quad (C.42)$$

$$q_2^2 = \frac{1}{4} (1 - \Omega_{11}^{A \rightarrow B} + \Omega_{22}^{A \rightarrow B} - \Omega_{33}^{A \rightarrow B}) \quad (C.43)$$

$$q_3^2 = \frac{1}{4} (1 - \Omega_{11}^{A \rightarrow B} - \Omega_{22}^{A \rightarrow B} + \Omega_{33}^{A \rightarrow B}). \quad (C.44)$$

The main problem is to determine the signs of the components q_0, q_1, q_2, q_3 . To do this, the maximum value of the following terms has to be determined:

$$q_0 = \frac{1}{4} \sqrt{1 + \Omega_{11}^{A \rightarrow B} + \Omega_{22}^{A \rightarrow B} + \Omega_{33}^{A \rightarrow B}} \quad (\text{C.45})$$

$$q_1 = \frac{1}{4} \sqrt{1 + \Omega_{11}^{A \rightarrow B} - \Omega_{22}^{A \rightarrow B} - \Omega_{33}^{A \rightarrow B}} \quad (\text{C.46})$$

$$q_2 = \frac{1}{4} \sqrt{1 - \Omega_{11}^{A \rightarrow B} + \Omega_{22}^{A \rightarrow B} - \Omega_{33}^{A \rightarrow B}} \quad (\text{C.47})$$

$$q_3 = \frac{1}{4} \sqrt{1 - \Omega_{11}^{A \rightarrow B} - \Omega_{22}^{A \rightarrow B} + \Omega_{33}^{A \rightarrow B}}. \quad (\text{C.48})$$

Once the maximum has been found, all the other values can be obtained from a linear combination of the off-diagonal terms of matrix $\Omega_{rot}^{A \rightarrow B}$. The procedure is summarized in Table C.1: the left column indicates the maximum value between the four components and following each row, the expressions to evaluate the the other components are given.

Max value	q_0	q_1	q_2	q_3
q_0	q_0	$\frac{\Omega_{32}^{A \rightarrow B} - \Omega_{23}^{A \rightarrow B}}{4q_0}$	$\frac{\Omega_{13}^{A \rightarrow B} - \Omega_{31}^{A \rightarrow B}}{4q_0}$	$\frac{\Omega_{21}^{A \rightarrow B} - \Omega_{12}^{A \rightarrow B}}{4q_0}$
q_1	$\frac{\Omega_{32}^{A \rightarrow B} - \Omega_{23}^{A \rightarrow B}}{4q_1}$	q_1	$\frac{\Omega_{21}^{A \rightarrow B} - \Omega_{12}^{A \rightarrow B}}{4q_1}$	$\frac{\Omega_{13}^{A \rightarrow B} - \Omega_{31}^{A \rightarrow B}}{4q_1}$
q_2	$\frac{\Omega_{13}^{A \rightarrow B} - \Omega_{31}^{A \rightarrow B}}{4q_2}$	$\frac{\Omega_{21}^{A \rightarrow B} - \Omega_{12}^{A \rightarrow B}}{4q_2}$	q_2	$\frac{\Omega_{32}^{A \rightarrow B} - \Omega_{23}^{A \rightarrow B}}{4q_2}$
q_3	$\frac{\Omega_{21}^{A \rightarrow B} - \Omega_{12}^{A \rightarrow B}}{4q_3}$	$\frac{\Omega_{13}^{A \rightarrow B} - \Omega_{31}^{A \rightarrow B}}{4q_3}$	$\frac{\Omega_{32}^{A \rightarrow B} - \Omega_{23}^{A \rightarrow B}}{4q_3}$	q_3

Table C.1: Quaternion components: algorithm table

Appendix D

Percentage Error

When comparing different results, it is usually convenient to introduce a percentage error, instead of a simple difference between the absolute values. If x_1 and x_2 are the values to be compared, the percentage error ϵ is defined as

$$\epsilon = 100 \frac{|x_1 - x_2|}{x_m} \quad (\text{D.1})$$

where

$$x_m = \frac{|x_1 + x_2|}{2}. \quad (\text{D.2})$$

Bibliography

- [1] H. Ashley and M. Landahl. *Aerodynamics of Wings and Bodies*. Dover Books on Aeronautical Engineering Series. Dover Publications, Incorporated, 2012.
- [2] Ashish Bagai, J. Gordon Leishman, and Jacob Park. Aerodynamic Analysis of a Helicopter in Steady Maneuvering Flight Using a Free-Vortex Rotor Wake Model. *Journal of The American Helicopter Society*, 44, 1999.
- [3] P. Bassanini, C. M. Casciola, M. R. Lancia, and R. Piva. Uniqueness of the bounded flow solution in aerodynamics. *Computational Mechanics*, 22(1):12–18, 1998.
- [4] P. Bassanini, C.M. Casciola, M.R. Lancia, and R. Piva. Edge singularities and kutta condition in 3d aerodynamics. *Meccanica*, 34(3):199–229, 1999.
- [5] G. Bernardini. *Problematiche Aerodinamiche Relative alla Progettazione di Configurazioni Innovative*. PhD thesis, Politecnico di Milano, Nov 1999.
- [6] G. Bernardini, J. Serafini, M. Molica Colella, and M. Gennaretti. Analysis of a structural-aerodynamic fully-coupled formulation for aeroelastic response of rotorcraft. *Aerospace Science and Technology*, 29(1):175 – 184, 2013.
- [7] David Biermann and W. H. Gray. Wind-tunnel tests of single- and dual-rotating pusher propellers having from three to eight blades. Wartime report, National Advisory Committee for Aeronautics. Langley Aeronautical Lab.; Langley Field, VA, United States, 1942.
- [8] G. Buresti. *Elements of Fluid Dynamics*. ICP Fluid Mechanics. Imperial College Press, 2012.
- [9] F. X. Caradonna and C. Tung. Experimental and analytical studies of a model helicopter rotor in hover. 1981.

- [10] Ki Hoon Chung, Jae Wook Kim, Ki Wahn Ryu, Kyung Tae Lee, and Duck Joo Lee. Sound generation and radiation from rotor tip-vortex pairing phenomenon. *AIAA Journal*, 44(6):1181–1187, June 2006.
- [11] L. Demasi. *Aerodynamic Analysis of Non-conventional Wing Configurations for Aeroelastic Applications*. PhD thesis, Politecnico di Torino, 2004.
- [12] L. Erickson. Panel methods: An introduction. Technical Report TP 2995, NASA, 1990.
- [13] Massimo Gennaretti and Giovanni Bernardini. Novel boundary integral formulation for blade-vortex interaction aerodynamics of helicopter rotors. *AIAA Journal*, 45(6):1169–1176, June 2007.
- [14] Z. Grobekatthofer, K. Yoon. Introduction into quaternions for spacespace attitude representation, May 2012.
- [15] Moqin He, Brain Veitch, Neil Bose, Bruce Colbourne, and Pengfei Liu. A three-dimensional wake impingement model and applications on tandem oscillating foils. *Ocean Engineering*, 34(89):1197 – 1210, 2007.
- [16] J. Hess and M. Smith. Calculation of Potential Flows about Arbitrary Bodies. 1967.
- [17] J. Katz and A. Plotkin. *Low-Speed Aerodynamics*. Cambridge Aerospace Series. Cambridge University Press, 2001.
- [18] V A Kondrat’ev and O A Oleinik. Boundary-value problems for partial differential equations in non-smooth domains. *Russian Mathematical Surveys*, 38(2):1, 1983.
- [19] K. Krishnamurty. *Principles of Ideal-fluid Aerodynamics*. R. E. Krieger Publishing Company, 1980.
- [20] J. Gordon Leishman. *Principles of helicopter aerodynamics*. Cambridge aerospace series. Cambridge University Press, Cambridge, New York, 2000.
- [21] J. Gordon Leishman and Ashish Bagai. Challenges in Understanding the Vortex Dynamics of Helicopter Rotor Wakes. *Aiaa Journal*, 36:1130–1140, 1998.
- [22] J. Gordon Leishman and Mahendra J. Bhagwat. Generalized viscous vortex model for application to free-vortex wake and aeroacoustic calculations. 58th Annual Forum and Technology Display of the american Helicopter Society International, Montreal, Canada, 11-13 June 2002.

- [23] Smith J.H.B. Mangler, K. W. Behaviour of the vortex sheet at the trailing edge of a lifting wing. *The Aeronautical Journal*,, 74:906–908, 1970.
- [24] B. Maskew. Program vsaero theory document. Technical Report CR 4023, NASA, 1987.
- [25] L. Menna. Progetto preliminare di eliche libere e intubate per velivoli ultraleggeri. Master’s thesis, Università’ di Pisa, 2014.
- [26] Giovanni Monegato. Numerical evaluation of hypersingular integrals. *Journal of Computational and Applied Mathematics*, 50(13):9 – 31, 1994.
- [27] L. Morino. Boundary integral equation in aerodynamics. *Appl. Mech. Rev.*, (46), 1993.
- [28] A. Quarteroni, R. Sacco, and F. Saleri. *Numerical Mathematics*. Texts in Applied Mathematics. Springer, 2010.
- [29] A.A. Rangwalla. *Application of a Potential Code to General Unsteady Flows in Three Dimensions*. UMI, 1986.
- [30] T. Theodorsen. *General Theory of Aerodynamic Instability and the Mechanism of Flutter*. National Advisory Committee for Aeronautics: Report. NACA, 1934.
- [31] A.H. Watt and M. Watt. *Advanced animation and rendering techniques: theory and practice*. ACM press frontier series. ACM Press, 1992.
- [32] G. S. Winckelmans. *Topics in vortex methods for the computation of three- and two-dimensional incompressible unsteady flows*. PhD thesis, California Institute of Technology, 1989.
- [33] E. Zupan, M. Saje, and D. Zupan. The quaternion-based three-dimensional beam theory. *Computer Methods in Applied Mechanics and Engineering*, 198(4952):3944 – 3956, 2009.